



Title	Bond behavior and degradation mechanisms of Multi-functional Fabric Reinforced Cementitious Matrix (MFRCM) composites used for ICCP-SS
Author(s)	Zhu, Miaochang
Citation	北海道大学. 博士(工学) 甲第14239号
Issue Date	2020-09-25
DOI	10.14943/doctoral.k14239
Doc URL	<a href="http://hdl.handle.net/2115/79415">http://hdl.handle.net/2115/79415</a>
Type	theses (doctoral)
File Information	Zhu_Miaochang.pdf



[Instructions for use](#)

**Bond behavior and degradation mechanisms of Multi-functional Fabric  
Reinforced Cementitious Matrix (MFRCM) composites used for ICCP-SS**

ICCP-SS 工法に用いる多機能型繊維補強セメント系複合材料 (MFRCM) の付  
着挙動と劣化メカニズム

By  
Miaochang ZHU

A thesis submitted in partial fulfillment of the requirements for the degree of  
Doctor of Philosophy in Engineering

Supervisor  
Associate Professor Koji MATSUMOTO

Co-supervisor  
Professor Tamon UEDA  
Professor Ji-Hua ZHU

English Engineering Program (e3)  
Division of Engineering and Policy for Sustainable Environment  
Graduate School of Engineering  
Hokkaido University  
September 2020

## Acknowledgment

To begin with, I would like to express my sincerest gratitude to my supervisors, Prof. Tamon Ueda and Prof. Jihua Zhu, for their joint-supervision during my PhD study. I am very grateful to Prof. Tamon Ueda not only for his kindness, patience, and responsibility but also for his valuable, inspirational and constructive instructions and suggestions, which helps me enormously in conducting my study. I do appreciate him for his continued supervision after he retired from Hokkaido University. I also feel very much indebted to Prof. Jihua Zhu for his constant guidance since I was an undergraduate student, and for his all-round encouragement and support to create the conditions for my PhD study. To work under their supervision is a wonderful experience, which benefits me a lot from not only their knowledge and skills but also their passion and attitude towards research.

Many thanks go to Dr. Koji Matsumoto, who becomes my official supervisor after Prof. Tamon Ueda retired, for his kind, thoughtful and constructive comments. I also thank him very much for his help in handling the procedures for applying for the doctoral degree. I would also like to thank the examination committee members: Prof. Takashi Matsumoto, Prof. Takafumi Sugiyama and Prof. Hiroshi Yokota for their valuable questions and comments that contribute to improving my study.

My thanks also go to Dr. Meini Su for her suggestions since the beginning of my PhD study, which helps improve my study. I would also like to extend my sincere thanks to Dr. Werawan Manakul for encouraging me and sharing stories about the university, life, and culture, in which I found something fresh and interesting.

I also appreciate the e3 program and the staff for their kind cooperation and help that make my life and study convenient in Hokkaido university. My appreciation also extends to all my lab mates for creating a kind, friendly, pleasant, positive, and motivating atmosphere, especially Zhao Wang, LiangLiang Wei, Yang Xie and Piyu Chen for the enjoyable time. Besides, I would like to thank the lab mates who do me favor in the extensive experimental work: Wanqian Li, Zhi Wang, Zhaojun Qin and Jianming Dong.

I would also like to acknowledge the financial support from the Key-Area Research and Development Program of Guangdong Province (2019B111107002), the National Key Research and Development Program of China (2018YFE0124900), the National Natural Science Foundation of China (51538007/51778370/51861165204), the Natural Science Foundation of Guangdong (2017B030311004), and the Shenzhen Science and Technology Project (GJHZ20180928155819738).

Finally, I am extremely thankful to my family, especially my wife, for their constant unconditional support and love, which gives me the courage and confidence throughout the PhD candidature.

## Abstract

A sustainable repair method, which is called ICCP-SS (impressed current cathodic protection and structural strengthening), has been proposed for deficient reinforced concrete structures caused by corrosion of steel in concrete. In the implementation of the proposed method, a material that plays a dual functional role as structural reinforcement and impressed current anode should be used and applied on concrete substrate. A multifunctional fabric reinforced cementitious matrix (MFRCM) composite in which carbon fabric is incorporated is employed as such a functional material. While the MFRCM composite works in an ICCP-SS system the embedded carbon fabric is subjected to not only anodic polarization that is related to electrochemistry but also the stress transferred from the surrounding matrix. Thus, there is a need to investigate the bond behavior and degradation of carbon fabric embedded in the matrix under anodic polarization, which helps gain an in-depth understanding of the global behavior of MFRCM composites and the effectiveness and efficiency of the ICCP-SS method.

Systematic research work was carried out, with a major aim at clarifying the bond behavior at the interface between carbon fabric and cementitious matrix within MFRCM composites under anodic polarization. In the beginning, the bond behavior of carbon yarn embedded in a range of cementitious matrices was investigated. The bond slip relationship was determined for the carbon yarn embedded in various matrices. The results show that the carbon yarns embedded in various matrices feature a similar bond behavior that can be represented by a trilinear bond slip relationship. Once the tensile strength is attained, fracture of the embedded carbon yarn can take place. An approach was derived to calculate the critical embedment length based on the bond slip relationship. Afterwards, the effect of matrix impregnation on the bond behavior between carbon fabric and matrix was studied. The outer (impregnated) part and inner (unimpregnated) part can be distinguished within a single carbon yarn due to limited matrix impregnation. The percentage of the impregnated part was estimated as 30% of the whole carbon yarn based on the image process and analysis results. Besides, the respective bond slip relationship for the outer (matrix-outer part) and inner (outer part-inner part) interface was determined based on the pullout test results. By carrying out finite element modeling that incorporates the evaluated bond slip relationships, a good agreement can be achieved between numerical and experimental results. Besides, the stress transfer at the outer and inner interfaces and the contribution of the outer and inner parts to carrying the applied force as well as the effects of key parameters on the pullout behavior were also discussed based on numerical simulation.

With introducing anodic polarization, MFRCM composites were investigated concerning the electrochemical performance, the mechanisms of degradation and the bond behavior between carbon fabric and matrix. Stabilized electrochemical performance can be maintained for MFRCM composites polarized up to  $125 \text{ mA/m}^2$ , while an exponential growth of cell voltage can be seen for larger current densities. Using SEM, EDS, FTIR and XPS, the polarization induced changes in the chemical composition and morphology of carbon fabric and the surrounding matrix were analyzed. The results reveal that the carbon fabric in the matrix showed a clear sign of deterioration featured by multiple transverse cracks on the carbon filaments and significant changes in the surface functional groups. The changes in the



morphology of carbon fabric within MFRCM composites were also discussed. Finally, the effect of anodic polarization on the bond behavior between carbon fabric and matrix was examined. The respective bond slip relationship for the outer and inner interface was determined based on test results obtained from anodically polarized MFRCM composites. The results show that anodic polarization compromises the bond behavior for both interfaces, depending on the extent of anodic polarization. With increasing the extent of anodic polarization, both the local bond strength and the residual bond stress decrease for the outer interface, while the local bond strength is reduced for the inner interface.

**Keywords:** Anodic polarization, Bond behavior, Bond slip relationship, Carbon fabric, Cementitious matrix, Degradation mechanisms, ICCP-SS, Matrix impregnation, MFRCM composites

# TABLE OF CONTENTS

ACKNOWLEDGMENT.....	I
ABSTRACT .....	II
TABLE OF CONTENTS .....	IV
<b>1 INTRODUCTION .....</b>	<b>1</b>
1.1 BACKGROUND .....	1
1.2 LITERATURE REVIEW .....	2
1.2.1 <i>FRCM composites for concrete strengthening</i> .....	2
1.2.2 <i>Carbon fibers in ICCP for reinforced concrete</i> .....	3
1.3 OBJECTIVES OF THE STUDY .....	4
1.4 OUTLINE OF THE DISSERTATION.....	4
<b>2 BOND BEHAVIOR OF CARBON YARN EMBEDDED IN VARIOUS CEMENTITIOUS MATRICES.....</b>	<b>6</b>
2.1 INTRODUCTION .....	6
2.2 EXPERIMENTAL INVESTIGATION .....	7
2.2.1 <i>Raw materials and specimens</i> .....	7
2.2.2 <i>Test method for pullout tests</i> .....	8
2.2.3 <i>Test results</i> .....	8
2.3 ANALYTICAL EXTRACTION OF THE BOND SLIP RELATIONSHIP.....	11
2.3.1 <i>Description of the carbon yarn-matrix interfacial problem</i> .....	11
2.3.2 <i>Analytical solution of the interfacial issue</i> .....	12
2.3.3 <i>Analytical extraction of the bond slip relationship</i> .....	15
2.3.4 <i>Verification of the evaluated bond slip relationship</i> .....	16
2.4 DETERMINATION OF $L_d$ FOR THE EMBEDDED CARBON YARN .....	18
2.4.1 <i>Numerical simulation of the pullout curve</i> .....	18
2.4.2 <i>Numerical determination of <math>L_d</math></i> .....	21
2.4.3 <i>A proposed approach for calculating <math>L_d</math></i> .....	23
2.4.4 <i>Parametric study on effects of bond parameters on <math>L_d</math></i> .....	24
2.5 CONCLUSIONS OF THIS CHAPTER.....	27
<b>3 BOND BEHAVIOR OF CARBON FABRIC IN CEMENTITIOUS MATRIX WITH CONSIDERING MATRIX IMPREGNATION .....</b>	<b>30</b>
3.1 INTRODUCTION .....	30
3.2 EXPERIMENTAL INVESTIGATION .....	31
3.2.1 <i>Raw materials and carbon FRCM composite</i> .....	31
3.2.2 <i>Specimen preparation and test implementation</i> .....	32
3.2.3 <i>Test results</i> .....	33
3.3 DISCUSSION .....	35
3.3.1 <i>Estimation of the cross-sectional area of the outer part</i> .....	35
3.3.2 <i>Evaluation of bond slip relationships for the outer and inner interfaces</i> .....	37

3.3.3	<i>Numerical modeling of pullout tests</i> .....	42
3.3.4	<i>Parametric study on effects of key parameters</i> .....	46
3.4	CONCLUSIONS OF THIS CHAPTER.....	49
<b>4</b>	<b>MECHANISMS OF DEGRADATION OF CARBON FABRIC POLARIZED IN CEMENTITIOUS MATRIX</b> .....	<b>51</b>
4.1	INTRODUCTION .....	51
4.2	EXPERIMENTAL PROGRAM .....	52
4.2.1	<i>Materials and specimen preparation</i> .....	52
4.2.2	<i>Application of galvanostatic anodic polarization</i> .....	53
4.2.3	<i>Material characterization for MFRCM composites</i> .....	54
4.3	TEST RESULTS AND DISCUSSION .....	55
4.3.1	<i>Electrochemical behavior of carbon fabric in cementitious matrix</i> .....	55
4.3.2	<i>Elemental distribution in the matrix around the carbon fabric</i> .....	58
4.3.3	<i>Morphology and surface elements of the embedded carbon fabric</i> .....	60
4.3.4	<i>Surface chemical composition of the embedded carbon fabric</i> .....	62
4.4	DISCUSSION .....	66
4.5	CONCLUSIONS OF THIS CHAPTER.....	69
<b>5</b>	<b>BOND BEHAVIOR OF CARBON FABRIC IN CEMENTITIOUS MATRIX SUBJECTED TO ANODIC POLARIZATION</b> .....	<b>71</b>
5.1	INTRODUCTION .....	71
5.2	EXPERIMENTAL PROGRAM .....	72
5.3	RESULTS AND DISCUSSIONS.....	73
5.3.1	<i>Pullout test results</i> .....	73
5.3.2	<i>Effects of anodic polarization on sectional area of the embedded carbon yarn</i> .....	76
5.3.3	<i>Effects of anodic polarization on bond slip relationship for the outer interface</i> .....	78
5.3.4	<i>Effects of anodic polarization on bond slip relationship for the inner interface</i> .....	80
5.4	CONCLUSIONS OF THIS CHAPTER.....	82
<b>6</b>	<b>SUMMARY AND SUGGESTIONS</b> .....	<b>83</b>
6.1	SUMMARY.....	83
6.2	SUGGESTIONS FOR FUTURE WORKS.....	84
<b>7</b>	<b>APPENDIX A</b> .....	<b>86</b>
7.1	INTRODUCTION .....	86
7.2	GENERALIZED EVALUATION OF BOND BEHAVIOR BETWEEN FRP AND CONCRETE.....	86
7.2.1	<i>Determination of <math>\tau</math>-<math>s</math> relationship using the <math>P</math>-<math>u</math> curve</i> .....	86
7.2.2	<i>Prediction of the bond strength model</i> .....	88
7.2.3	<i>Prediction of strain and bond stress distribution</i> .....	88
7.2.4	<i>Determination of <math>L_{eff}</math></i> .....	90
7.3	AN INTRODUCTORY EXAMPLE OF UTILIZING THE PROPOSED METHOD .....	91
7.4	VERIFICATION OF THE PROPOSED METHOD TO CALCULATE $L_{EFF}$ .....	98
	<b>REFERENCES</b> .....	<b>101</b>

# Chapter 1

## 1 Introduction

### 1.1 Background

Corrosion of steel reinforcement is one of the major causes to deteriorate the structural performance of reinforced concrete structures. Once steel corrosion in concrete initiates, the cross-sectional area of steel reinforcement is reduced, the bond between steel and concrete is damaged and concrete is cracked along the steel bar. When concrete cracking happens, harmful species can more easily reach the steel bar through cracked concrete and accelerate the process of steel corrosion.

In the course of steel corrosion, reinforced concrete structures suffer from corrosion induced deterioration and become the deficient ones of which structure performance cannot satisfy the original or upgraded requirements. Therefore, the deficiencies in structural performance call for structural strengthening. In the last decades, a wide range of structural strengthening technologies have been developed, such as increasing sectional area, introduction of prestressing, and external bonding (ACI 318-02/318R-02 2002; ACI 562M-13 2015). Among these technologies, external bonding has gained great popularity in the scientific and engineering communities due to its efficiency, ease installation, and little interference (ACI 440.2R 2008). The choice of different structural strengthening methods depends on the practical demand. Anyway, structural performance can be ensured if the chosen method was properly designed and implemented. However, although the structural performance of corroded concrete structures can be improved by conducting structural strengthening, there is little impact on the process of steel corrosion in concrete. This indicates the temporarily strengthened structures are likely to become deficient again with the elapse of time, which is due to the lasting corrosion induced deterioration. Therefore, one-off strengthening work may not suffice for the expected lifespan of the structures, and repetitive work is possibly called for. When assessing the service life of the strengthened structures, it is also necessary to carefully consider the subsequent impact of steel corrosion in concrete.

In addition to structural strengthening, much attention has also been paid to protecting steel in concrete from corrosion. If the steel in concrete can be effectively protected, there is no risk of structural degradation caused by steel corrosion and the upgraded structural performance can be maintained throughout the expected lifespan. There exist several developed techniques for preventing steel corrosion, including utilizing stainless steel, application of coated steel, the use of corrosion inhibitors, cathodic protection and so forth (ACI 222R-01 2001). Among these options, impressed current cathodic protection (ICCP) has been recognized as an effective method to control corrosion of steel in concrete (Pedferri 1996; ACI 222R-01 2001; Byrne et al. 2016; Polder and Peelen 2018), especially in the chloride contaminated concrete. ICCP involves applying cathodic current to the steel in concrete and thus negatively shifting the steel potential to the immunity zone where the corrosion rate of steel is negligible. Although steel corrosion can be effectively controlled by ICCP, the existing loss in structural performance should be addressed by simultaneously adopting SS so that the safety of the structures will suffice during service life.

It can be found that for deficient concrete structures caused by steel corrosion both SS and corrosion control should be better handled at the same time to gain the endurable long-term structural performance. SS and corrosion control are currently considered in a separate manner, which means the impact on corrosion control is usually neglected when applying structural strengthening and vice versa. Recently, an innovative sustainable method that can provide structural strengthening and corrosion control simultaneously has been proposed. The method is the so-called ICCP-SS method, which combines the advantages of impressed current cathodic protection (ICCP) and structural strengthening (SS). A typical ICCP-SS system is shown in Fig. 1.1, which consists of existing reinforced concrete, an impressed current anode, a power supply, monitors and cables and so on. Such a system shares something in common with the SS and ICCP system in which a layer of reinforcement or anode is applied onto the concrete for SS or ICCP. The core component of an ICCP-SS system is the multifunctional fabric reinforced cementitious matrix (MFRCM) composite that functions as not only the reinforcing material but also the impressed current anode.

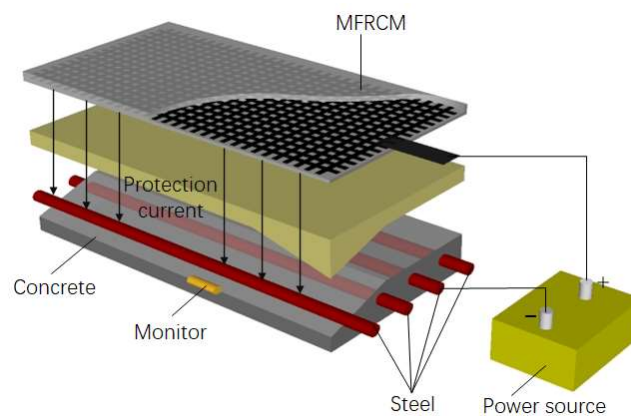


Fig. 1.1 A typical ICCP-SS system

## 1.2 Literature review

### 1.2.1 FRCM composites for concrete strengthening

MFRCM composite is the same as the FRCM composites without being considered to play a role as the impressed current anode. The FRCM composite normally comprises a fabric or textile as reinforcement embedded in the cementitious matrix and shows improved tensile behavior and ductility in comparison to the plain cementitious materials (ACI 549.4R-13 2013). The composite is externally applied onto substrate concrete and subjected to tension force. Compared with FRP strengthening, the matrix and adherend are normally made of cementitious material rather than organic resin for the FRCM composite, while allows overcoming some drawbacks associated with the use of the organic matrix, such as strict requirements on the concrete surface, weathering or aging of organics, poor performance at high temperature and emission of harmful substance(s). So far, many research efforts have been devoted to the development of FRCM strengthening. It can be found from the literature that most studies are focused on the following topics: i) tensile behavior of the FRCM composites (ACI 549.4R-13 2013); ii) bond mechanisms at the fabric-matrix interface and the FRCM composite-concrete interface (Carozzi et al. 2020); iii) member behavior of FRCM strengthening systems, such as

flexural or shear strengthening of reinforced concrete beams and confinement of reinforced concrete columns (Awani et al. 2017; Koutas et al. 2019). Differing from FRP strengthening systems in which the typical failure is debonding of the surface concrete, the failure is often related to debonding at the fabric-matrix interface for the strengthening systems, which has gained much concern. It can be found that the mechanical behavior of the FRCM composite and the efficiency of the strengthening systems depend on the bond behavior between fabric and matrix. The bond behavior between various fabrics and matrix has been widely investigated (Carozzi et al. 2020). Compared with glass and PBO fabric, the bond behavior between carbon fabric and matrix is less concerned.

Carbon fabric normally comprises carbon yarns deposited in different directions, and each carbon yarn consists of thousands of filaments bundled together. As the free spacing between filaments within one single yarn is smaller than the size of cement particles, the cementitious matrix cannot fully impregnate the whole yarn, leading to various bond characteristics of different filaments. The filaments in the outer layer of the carbon yarn can receive good matrix impregnation and thus show strong adhesion with the matrix, and these filaments are termed as sleeve filaments. While for the core filaments of the carbon yarn, they are not in contact with the matrix due to the limited matrix impregnation, and the stress transfer is caused by friction between them. During slippage of the carbon yarn, the filaments show varying normal tensile stress due to different bond characteristics with the stress reduced from the outermost towards the core of the yarn. Therefore, the breakage of all the filaments cannot happen at the same time but in a progressive manner, and the outermost filaments fail first. It is obvious that matrix impregnation complicates the bond behavior between carbon fabric and matrix. However, although the progressive failure has been investigated on the multifilament glass yarn embedded in the cementitious matrix (Banholzer 2006), there is little available information regarding the carbon yarn that shows similar behavior.

### 1.2.2 Carbon fibers in ICCP for reinforced concrete

ICCP has turned out to be an effective technique to prevent steel corrosion (ACI 222R-01 2001). During application ICCP, the cathodic current is applied to the steel from the external anode through the concrete. The steel is therefore forced to be a cathode in which the reduction reaction occurs and the original oxidation of iron during the corrosion process is prevented. Meanwhile, the oxidation reaction in which the hydroxyl ions are oxidized takes place on the external anode, and such a condition encountered by the anode is so-called anodic polarization. The effectiveness of ICCP is highly dependent on the electrochemical performance of the impressed current anode. Several impressed current anodes have been studied, such as cast-iron alloy, conductive coating, sprayed zinc and titanium-based anodes (ACI 222R-01 2001; Byrne et al. 2016). Among them, the mixed metal oxides coated titanium-based anode is the most common one in ICCP of concrete structures, as it is able to tolerate high current densities and exhibit a low rate of consumption. However, the anode is expensive and thus the large-scale promotion is to some extent limited. Therefore, there always exists a motivation for developing other cost-effective, reliable and durable anodes.

Recently, carbon fibers have received increasing attention for use as an anode in ICCP for reinforced concrete (Chini and Antonsen 2008; Nguyen et al. 2012; Zhang and Tang 2014; Zhu

et al. 2014, 2015). The mechanical and electrochemical performance of carbon FRP (CFRP) anodically polarized in different electrolyte were investigated. The results show that the tensile strength of polarized CFRP decreases with increasing the applied charge density and the epoxy in CFRP seems to be more vulnerable than carbon fibers (Sun et al. 2016a, 2016b). Besides, the degradation in the cementitious matrix close to carbon fibers used as an anode was also reported (Zhang 2018). It was found that during anodic polarization the matrix in the vicinity of carbon fibers shows a ring-pattern degraded zone which is characterized by calcium leaching (Zhang 2018). However, studies concerning the degradation of carbon fabric in the matrix after anodic polarization are scarce. Furthermore, when utilizing the MFRCM composites as both reinforcement and anode, stress transferred between carbon fabric and matrix after anodic polarization should be investigated to understand the tensile behavior of MFRCM composites and the corresponding strengthening systems. So far, there is no information regarding the bond behavior between carbon fabric and matrix within MFRCM composites subjected to anodic polarization.

### **1.3 Objectives of the study**

The objectives of this study are as follows.

1. To establish the bond slip relationship of single carbon yarn embedded in the cementitious matrix.
2. To clarify the bond behavior of carbon fabric embedded in the cementitious matrix with considering matrix impregnation and propose a method for evaluating different bond slip relationships for different interfaces involved in the embedded carbon fabric.
3. To evaluate the electrochemical performance of carbon fabric utilized as an anode in the ICCP-SS system and clarify the mechanisms of degradation of the carbon fabric in the cementitious matrix subjected to anodic polarization.
4. To evaluate the bond behavior of carbon fabric in the cementitious matrix after anodic polarization and establish the effects of anodic polarization on bond slip relationships for different interfaces involved in the embedded carbon fabric.

### **1.4 Outline of the dissertation**

This dissertation contains six chapters and one appendix as follows.

Chapter 1 presents the background of the present study, the literature review, the objectives of the study and the outline of the dissertation.

Chapter 2 presents the bond behavior of carbon yarn embedded in a range of cementitious matrices. The chapter describes the experimental program and the method used to determine the bond slip relationship based on pullout test results. The bond slip relationship is determined for the carbon yarn in various cementitious matrices. Besides, an approach is presented to determine the critical embedment length of the carbon yarn based on the evaluated bond slip relationship.

Chapter 3 describes the bond behavior of carbon fabric embedded in the cementitious matrix, which is influenced and complicated by matrix impregnation. The chapter presents the experimental program and the method of determining the percentage of the impregnated part

and the respective bond slip relationship for different interfaces involved between carbon fabric and matrix based on pullout test results. Then, numerical modeling is carried out to validate the accuracy of the evaluated bond slip relationships. In addition, the contribution of the outer and inner part to resisting the applied force, the bond stress distribution at the outer and inner interface and the effects of key parameters on the pullout behavior are discussed.

Chapter 4 aims at investigating the electrochemical performance and material degradation of carbon fabric within the MFRCM composites. The chapter shows the electrochemical performance of the composites and characterization of the changes in the chemical compositions and morphology of the carbon fabric and cementitious matrix using a series of characterization techniques. The discussion on the mechanisms of morphological changes in the carbon fabric due to anodic polarization is also presented.

Chapter 5 presents the bond behavior of carbon fabric within the MFRCM composites subjected to anodic polarization. The chapter describes the changes in the sectional area and the pullout behavior of the carbon yarn within the composites with anodic polarization. The bond slip relationships for different interfaces between carbon fabric and matrix are established for the polarized composites.

Chapter 6 summarizes the major conclusions based on the present study and gives suggestions for future works that may help advance the ICCP-SS technique.

Appendix A presents the development of a generalized method of evaluating bond behavior of the externally bonded FRP reinforcement. The chapter shows the mathematical derivation of the proposed method in terms of bond slip relationship, bond strength, strain distribution of FRP and the effective bond length. An introductory example is illustrated to show the implementation of the proposed method on a referenced FRP-concrete interface. Besides, discussions on the reliability of the method to calculate the effective bond length are presented.



## Chapter 2

### 2 Bond behavior of carbon yarn embedded in various cementitious matrices

#### 2.1 Introduction

Many efforts have been made to investigate the mechanical behavior of FRCM composites and the corresponding strengthening systems. Tensile behavior of FRCMs (Hegger et al. 2006; Häußler-Combe and Hartig 2007; Barhum and Mechtcherine 2011; Contamine et al. 2011; Larrinaga et al. 2014; Carozzi et al. 2017; Donnini and Corinaldesi 2017; De Santis et al. 2017; Wei et al. 2019) and the bond behavior of FRCM-concrete or FRCM-masonry joints (Hashemi and Al-Mahaidi 2010; D'Ambrisi et al. 2013; Tran et al. 2014; Sneed et al. 2015; Raoof et al. 2016) have been extensively studied, as these investigations can characterize FRCMs and provide the necessary properties for their applications, such as the flexural strengthening of RC beams (Hashemi and Al-Mahaidi 2010; Ambrisi and Focacci 2011; Escrig et al. 2017) and confinement of RC columns (Ombres and Mazzuca 2017).

The bond behavior between FRCM composites and concrete has been investigated by shear bond tests, in which the local bond-slip relationship can be obtained. The bond slip relationship led to analytical or numerical modeling that agrees well with the experimental data (Carozzi et al. 2016; D'Antino et al. 2018). However, this relationship is affected by various failure mechanisms, like debonding between the fabric and matrix or between the FRCM and substrate, slippage of the fabric and matrix cracking. It was found that slippage of the fabric through the matrix usually occurs as the dominant failure mode or accompanying other failure modes in tensile tests on the FRCM composites and shear tests on FRCM composites-concrete interfaces. Thus, it is of critical importance to investigate the bond behavior between fabric and matrix to understand the load transfer between the composites and concrete and further the corresponding strengthening systems.

It can be found that the fabric-matrix bond is affected by diverse factors. These factors involve fabric type (Sueki et al. 2005; Williams Portal et al. 2014), geometry and surface condition of the fabric (Peled et al. 1998), matrix type (Peled et al. 2008), and fabrication method (Peled et al. 2006). Nevertheless, the report regarding the bond between carbon fabric and cementitious matrix is relatively limited, though the tensile characterization of the carbon FRCM composites has been reported in (Arboleda 2014; Donnini et al. 2015; Carozzi et al. 2017; D'Antino and Papanicolaou 2017; De Santis et al. 2017). The effects of the matrix type (Badanoiu and Holmgren 2003) and embedded length (Lancioni et al. 2017) on the pullout behavior of the carbon yarn in the cementitious matrix can be found in the existing literature. The carbon yarn is usually embedded in the matrix, which makes it appear more like an internal reinforcement than an external reinforcement. For internal reinforcement, a bond length can always be found such that the tensile capacity is reached, which is herein termed the critical embedment length. To determine the critical embedment length for the embedded carbon yarn in a cementitious matrix is still a problem.

This chapter aims at studying the bond behavior at the interface between the carbon yarn and the cementitious matrix. Pullout tests in which the embedded carbon yarn was gradually pulled through the matrix were carried out on the carbon yarn embedded in various cementitious

matrices. These matrices were made by varying water to cement ratios ( $w/c$ ), sand to cement ratios ( $s/c$ ) and contents of short carbon fibers ( $cf$ ). Afterwards, the bond slip relationship of the carbon yarn-matrix interface was determined using an analytical method in which a trilinear bond slip relationship had been assumed. The bond parameters were obtained by comparing the analytical predictions to the main features within the pullout curves. Analytical modeling was conducted and verified against the experimental. An approach was then proposed to obtain the critical embedment length based on the determined trilinear bond-slip relationship. At last, a parametric study was carried out to study how the bond parameters affect the critical embedment length.

## 2.2 Experimental investigation

### 2.2.1 Raw materials and specimens

The carbon yarn was obtained from a coil that can be used to manufacture carbon fabric. There are 12,000 filaments bundled together for each carbon yarn and each filament has a diameter of 7 microns. Each yarn has a width of 5 mm and a perimeter that equals two times the width because the thickness is too small. To obtain the tensile properties of the carbon yarn, six tensile coupons were tested in tension according to (GB/T 3362-2005). The obtained Young's modulus and the ultimate tensile strength are 170 GPa and 1796 MPa, respectively.

Table 2.1 lists the composition and proportions of various matrices. The matrices were prepared by varying water to cement ratio ( $w/c$ ), sand to cement ratio ( $s/c$ ) and the content of short carbon fibers ( $cf$ ). The cementitious matrix to make the FRCM or TRC is normally finely grained (the maximum size of the aggregates in the range of 1-2 mm). Two types of quartz sand were used, fine sand (0-0.5 mm) and medium sand (0.5-1.0 mm), and the ratio by weight of these two types was 1:2. To gain good workability, superplasticizer (1.0 wt% of cement) was used for all the mixtures. Three matrix prismatic specimens measured  $40 \times 40 \times 160$  mm were cast to determine the flexural and compressive strength for each matrix. The matrix specimens were cured in water and then tested at a curing age of 28 days according to ISO 679:2009. The compressive and flexural strengths of various matrices are shown in Table 2.1.

Table 2.1 Composition, proportion and mechanical strengths of various matrices

No	Cement	Sand	Water	Carbon fiber	$f_c$ (MPa)	$f_m$ (MPa)
w0.30-s1.0	100	100	30	/	94.3	9.9
w0.35-s1.0	100	100	35	/	96.2	11.4
w0.40-s1.0	100	100	40	/	87.7	10.5
w0.45-s1.0	100	100	45	/	74.1	6.3
w0.35-s0.5	100	50	35	/	84.6	6.4
w0.35-s1.5	100	150	35	/	87.6	6.4
w0.35-s1.0-cf0.5	100	100	35	0.5	93.4	7.6
w0.35-s1.0-cf0.75	100	100	35	0.75	78.8	8.4
w0.35-s1.0-cf1.0	100	100	35	1	82.7	8.4

w0.35-s1.0-cf1.25	100	100	35	1.25	60.6	6.4
-------------------	-----	-----	----	------	------	-----

Note: the figures in the table indicate the content by mass of different constituents relative to that of cement.

Pullout specimens were made of matrix cylinders measuring  $50 \times 15$  mm (diameter  $\times$  height). Carbon yarn was centrally embedded in these cylinders and the nominal embedded length equaled 15 mm. All the specimens had a 100 mm long protruded part of carbon yarn. There are three parallel specimens for each matrix. These specimens were numbered per the matrix type. For instance, w0.3-s1.0-cf0.75-a indicates that this specimen was made of matrix w0.3-s1.0-cf0.75, and the following letter 'a' means one of the parallel specimens. Table 2.2 shows the measured geometries of all the specimens.

### 2.2.2 Test method for pullout tests

Fig. 2.1 shows the test setup for pullout tests. A steel frame was used to fasten the pullout specimens and connected to the testing machine. The protruded part of the carbon yarn in the specimens was clamped by a wedge-type grip after being reinforced with CFRP tabs. The direction of the applied force was carefully aligned with the longitudinal axis of the yarn in the pullout specimens. The specimens were loaded with an electronic universal test machine with a loading capacity of 10 kN. The displacement-controlled mode with a loading rate of .2 mm/min was adopted. The applied force was measured by a loading cell, while the displacement of the crosshead movement was measured. The pullout displacement of the carbon yarn was obtained by subtracting the tensile deformation of the protruded part from the measured displacement of the crosshead.



Fig. 2.1 Test setup for pullout tests

### 2.2.3 Test results

The pullout curve is a relationship between the applied force and the pullout displacement. Similar global behavior can be seen in the experimental pullout curve for all the specimens with a 15 mm bond length. Fig. 2.2 plots typical experimental pullout curves of three parallel specimens made of matrix w0.30-s1.0. The applied force rises with increasing pullout displacement and decreases until reaching a slowly descending branch. The post-peak pullout behavior is caused by degradation in the bond at the carbon yarn-matrix interface, while the

Table 2.2 Specimen geometries, test results and calibrated bond parameters as well as the comparison of the maximum pullout force between experiments and predictions

Specimens	Geometries		Test results		Calibrated bond parameters						$P_{Ana}$ (N)	$L_a$ (mm)
	$b$ (mm)	$L$ (mm)	$K_1$ (N/mm)	$K_2$ (N/mm)	$P_{max}$ (N)	$P_0$ (N)	$k_1$ (N/mm <sup>3</sup> )	$k_2$ (N/mm <sup>3</sup> )	$\tau_{max}$ (Mpa)	$\tau_0$ (Mpa)		
w0.30-s1.0-a	5.04	14.21	2092.7	792.5	452	109	16.65	5.28	3.23	0.76	452.6	27.86
w0.30-s1.0-b	6.06	14.50	2702.6	762.0	512	98	18.31	4.14	2.98	0.56	512.4	24.50
w0.30-s1.0-c	5.62	14.12	1879.5	753.0	517	196	13.30	4.54	3.33	1.23	517.8	23.56
w0.35-s1.0-a	5.28	14.06	2057.7	810.6	443	109	15.74	5.21	3.05	0.73	443.7	28.29
w0.35-s1.0-b	5.60	14.25	2701.5	817.2	535	98	20.09	4.88	3.43	0.61	543.2	22.95
w0.35-s1.0-c	5.26	14.42	2277.3	819.9	422	196	17.36	5.14	2.85	1.29	422.6	30.97
w0.40-s1.0-a	5.48	13.73	2100.0	812.9	513	125	15.84	5.16	3.49	0.83	513.7	23.16
w0.40-s1.0-b	5.46	15.47	3542.4	816.0	471	152	26.88	4.58	2.86	0.90	471.3	29.10
w0.40-s1.0-c	5.72	14.53	3434.6	814.8	500	104	25.87	4.67	3.08	0.63	500.3	25.33
w0.45-s1.0-a	5.50	15.30	2732.6	722.9	508	74	19.57	4.10	3.09	0.44	508.4	26.09
w0.45-s1.0-b	6.00	14.40	1834.8	822.8	456	21	11.92	4.53	2.70	0.12	456.9	28.05
w0.45-s1.0-c	5.28	14.47	2278.5	819.6	444	103	17.25	5.10	2.98	0.67	447.2	29.14
w0.35-s0.5-a	5.84	14.43	3843.7	766.6	610	277	29.33	4.34	3.70	1.64	612.2	20.04
w0.35-s0.5-b	6.06	14.31	2543.2	439.2	550	264	17.23	2.47	3.21	1.52	550.1	21.97
w0.35-s0.5-c	5.34	13.36	2400.8	1353.9	468	255	19.39	8.80	3.40	1.79	469.8	26.34
w0.35-s1.5-a	6.06	15.07	4888.4	820.8	697	153	13.71	4.54	3.92	0.84	698.2	18.15
w0.35-s1.5-b	5.66	14.40	2583.4	808.7	659	267	19.88	4.83	4.14	1.64	659.6	18.41
w0.35-s1.5-c	5.62	15.02	3171.2	821.4	726	130	16.25	4.81	4.41	0.77	727.1	17.31
w0.35-s1.0-cf0.5-a	6.06	14.64	4739.0	820.6	695	153	36.75	4.40	4.01	0.86	695.2	17.67
w0.35-s1.0-cf0.5-b	5.94	14.10	2747.2	820.5	735	127	19.49	4.67	4.49	0.76	735.7	16.02
w0.35-s1.0-cf0.5-c	6.88	14.62	3520.5	818.6	660	153	22.08	3.87	3.36	0.76	660.4	18.66
w0.35-s1.0-cf0.75-a	5.15	13.08	2156.1	819.2	540	141	18.12	5.81	4.10	1.05	540.7	20.78
w0.35-s1.0-cf0.75-b	5.50	12.90	2392.0	822.0	730	102	19.31	5.54	5.26	0.72	731.0	14.76

w0.35-s1.0-cf0.75-c	5.50	11.10	2171.3	821.0	585	41	19.76	6.47	4.88	0.34	589.5	16.07
w0.35-s1.0-cf1.0-a	5.68	15.42	3492.8	817.6	758	269	25.44	4.43	4.44	1.54	758.5	16.96
w0.35-s1.0-cf1.0-b	5.78	15.12	3056.8	820.7	780	66	21.52	4.46	4.58	0.38	780.6	16.13
w0.35-s1.0-cf1.0-c	5.30	15.16	3780.6	820.4	764	163	30.52	4.85	4.88	1.01	764.4	16.54
w0.35-s1.0-cf1.25-a	5.00	15.42	2415.7	818.1	563	171	18.49	5.03	3.75	1.11	563.7	23.51
w0.35-s1.0-cf1.25-b	4.52	14.52	2798.8	902.7	630	200	25.56	6.51	4.93	1.52	630.7	19.53
w0.35-s1.0-cf1.25-c	5.82	16.18	3733.3	820.2	673	190	26.11	4.12	3.67	1.01	673.7	20.25

last slowly descending part is attributed to the interfacial friction during pulling the carbon yarn out of the matrix. Fig. 2.3 shows the typical failure mode of the pullout specimens with a bond length of 15 mm. All the pullout specimens failed by slippage of the carbon yarn through the matrix for a 15 mm bond length. Besides, some major features of the pullout curve were obtained to determine the bond slip relationship, as shown in Table 2.2.

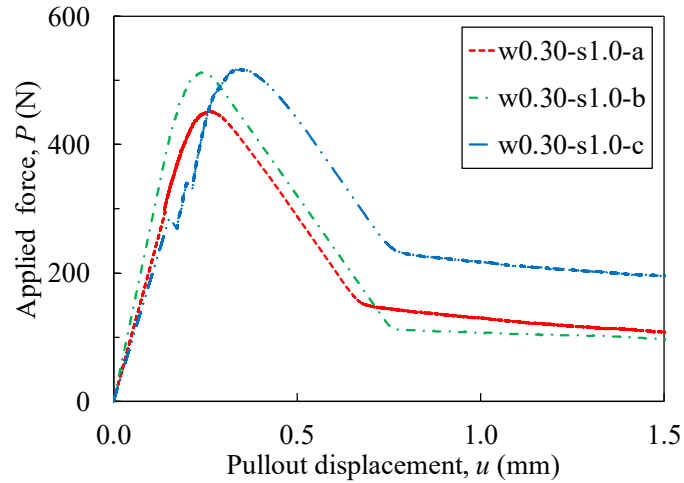


Fig. 2.2 The experimental pullout curves for three parallel specimens made of matrix w0.30-s1.0

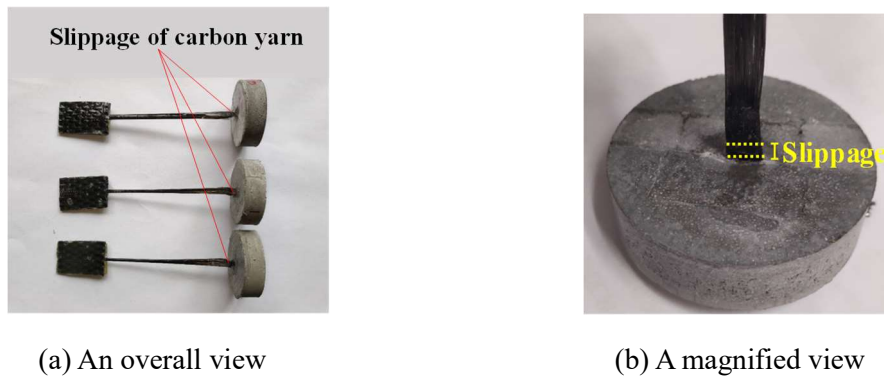


Fig. 2.3 The failure mode of pullout specimens, (a) an overall view and (b) a magnified view

## 2.3 Analytical extraction of the bond slip relationship

### 2.3.1 Description of the carbon yarn-matrix interfacial problem

Pullout tests on the carbon yarn embedded in the matrix are usually performed in order to obtain the bond slip relationship. The relationship can be determined analytically or numerically by comparing the analytical or numerical prediction to the experimental pullout curve. The analytical method may apply to some bond slip relationships such as a multilinear bond slip relationship, while the numerical method pertains to any bond slip relationship. In the previous paper (Zhu et al. 2018), the trilinear bond slip relationship was found to be able to represent the carbon yarn-matrix interface. Fig. 2.4 shows a diagram of an embedded carbon yarn in the cementitious matrix.

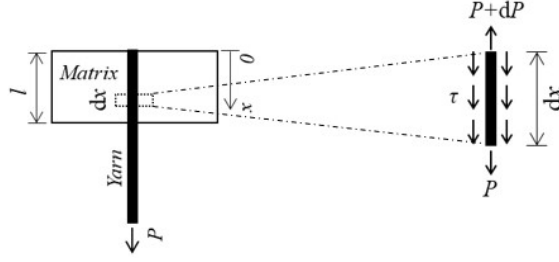


Fig. 2.4 An embedded carbon yarn in the cementitious matrix

Eq. (2.1) is valid considering the equilibrium of force in  $\Delta x$ .

$$Ad\sigma = c\tau dx \quad (2.1)$$

Where  $A$  and  $c$ , respectively, are the cross-sectional area and perimeter of the carbon yarn;  $\sigma$  is the tensile stress in the carbon yarn; and  $\tau$  is the local shear stress on the carbon yarn-matrix interface.

Substituting linear tensile behavior of the carbon yarn and the strain- displacement relationship into Eq. (2.1) yields,

$$\frac{d^2 s}{dx^2} - \frac{c\tau(s)}{EA} = 0 \quad (2.2)$$

Where  $s$  indicates the slip of the embedded carbon yarn, which is defined as the difference in the displacement of the carbon yarn and matrix;  $E$  is Young's modulus of the carbon yarn; and  $\tau(s)$  is the relationship between local shear stress and  $s$  on the carbon yarn-matrix interface, i.e. bond slip relationship. Eq. (2.2) is also termed the interfacial governing equation.

It is obvious that the free-end strain in the carbon yarn identically equals zero, and the slip at the loaded end, i.e. the pullout displacement,  $u$ , can be measured at any loading level. Thus, the boundary conditions at the loaded and free end can be formulated in Eq. (2.3) and Eq. (2.4), respectively.

$$s(x=L) = u \quad (2.3)$$

$$\left. \frac{ds}{dx} \right|_{x=0} = 0 \quad (2.4)$$

### 2.3.2 Analytical solution of the interfacial issue

Prior to determining the bond-slip relationship of the carbon yarn in the matrix, the closed-form solution of the interfacial governing equation was derived. As previously mentioned, a trilinear relationship (shown in Fig. 2.5) has been proposed to represent the bond behavior between the carbon yarn and the cementitious matrix. The three linear portions indicate the elastic, debonding and friction state, respectively.

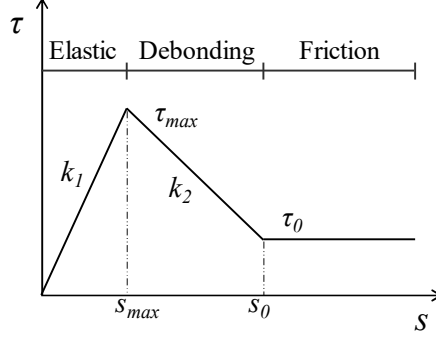


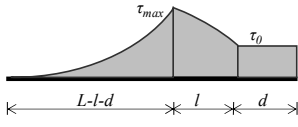
Fig. 2.5 The trilinear bond slip relationship for the carbon yarn-matrix interface

With adopting the trilinear relationship, the slip and tensile strain as well as bond stress distribution along the carbon yarn-interface can be derived upon analytically solving the interfacial equation. Similar derivation can refer to some studies (Carozzi et al. 2016; D'Antino et al. 2018; Sueki et al. 2005; Zhang et al. 2013, 2014). Table 2.3 presents the closed-form expressions for the slip distribution and the  $P-u$  curve. The analytical solution of the interfacial equation is helpful in not only determining the bond parameters in the bond-slip relationship based on the experimental results but also deriving the critical embedment length of the embedded carbon yarn.

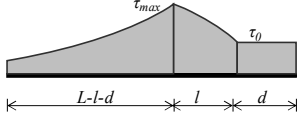
Table 2.3 The closed-form expressions for the slip distribution and the  $P-u$  relationship

Interface state (bond stress)	Analytical solution
<p>(a) Elastic state</p>	<p>For <math>-L &lt; x &lt; 0</math>, we have</p> $s(x) = \frac{P \cosh(\lambda_1 L + \lambda_1 x)}{EA \lambda_1 \sinh(\lambda_1 L)} \quad (2.5)$ $\lambda_1 = \sqrt{\frac{ck_1}{EA}} \quad (2.5a)$ <p>The <math>P-u</math> relationship becomes</p> $P = EA \lambda_1 \tanh(\lambda_1 L) u \quad (2.6)$
<p>(b) Elastic-debonding state</p>	<p>For <math>-l &lt; x &lt; 0</math>, we have</p> $s(x) = \frac{\tau_{max} \sin(\lambda_2 x + \varphi)}{k_2 \sin(\lambda_2 l - \varphi)} + \frac{k_1 + k_2}{k_1 k_2} \tau_{max} \quad (2.7)$ $\lambda_2 = \sqrt{\frac{ck_2}{EA}} \quad (2.7a)$ $\varphi = \lambda_2 l - \arctan\left(\frac{\lambda_1}{\lambda_2 \tanh(\lambda_1 L - \lambda_1 l)}\right) \quad (2.7b)$ <p>The <math>P-u</math> relationship becomes</p> $P = EA \lambda_2 \cot(\varphi) \left( u - \frac{k_1 + k_2}{k_1 k_2} \tau_{max} \right) \quad (2.8)$



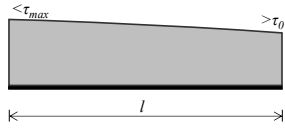


Or



(c) Elastic-debonding-friction state

Or



(c) Debonding state

The  $P\sim u$  relationship becomes

$$P = \frac{2EA}{d} \left[ u - \frac{\tau_{max}(k_1 + k_2) - k_1\tau_0}{k_1k_2} \right] + \frac{c\tau_0}{\lambda_2} \cot(\phi) \quad (2.9)$$

$$\phi = \lambda_2 l - \arctan \left( \frac{\lambda_1}{\lambda_2 \tanh(\lambda_1 L - \lambda_1 l - \lambda_1 d)} \right) \quad (2.9a)$$

Or

For  $-L < x < 0$ , we have

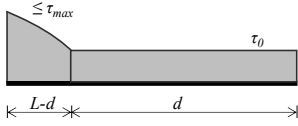
$$s(x) = \frac{P}{\lambda_2 EA} \sin(\lambda_2 x) - \frac{P \cos(\lambda_2 x)}{\lambda_2 EA \tan(\lambda_2 L)} + \frac{k_1 + k_2}{k_1 k_2} \tau_{max} \quad (2.10)$$

The  $P\sim u$  relationship becomes

$$P = \lambda_2 EA \tan(\lambda_2 L) \left( \frac{k_1 + k_2}{k_1 k_2} \tau_{max} - u \right) \quad (2.11)$$

For  $-L < x < -d$ , we have

$$s(x) = \frac{P - cd\tau_0}{EA\lambda_2} \left[ \sin(\lambda_2 x + \lambda_2 d) - \frac{\cos(\lambda_2 x + \lambda_2 d)}{\tan(\lambda_2 L - \lambda_2 d)} \right] + \frac{k_1 + k_2}{k_1 k_2} \tau_{max} \quad (2.12)$$



(d) Debonding-friction state

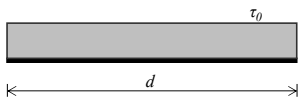
The  $P\sim u$  relationship becomes

$$P = cd\tau_0 + \frac{c\tau_0}{\lambda_2} \tan(\lambda_2 L - \lambda_2 d) \quad (2.13a)$$

$$u = \frac{Pd}{EA} - \frac{c\tau_0 d^2}{2EA} + \frac{k_1 + k_2}{k_1 k_2} \tau_{max} - \frac{\tau_0}{k_2} \quad (2.13b)$$

For  $-L < x < 0$ , we have

$$s(x) = \frac{c\tau_0}{2EA} (x^2 + 2Lx + L^2) + \frac{k_1 + k_2}{k_1 k_2} \tau_{max} - \frac{\tau_0}{k_2} \quad (2.14)$$



(e) Friction state

The  $P\sim u$  relationship becomes

$$P = c\tau_0 (L - u) \quad (2.15)$$

Depending on slip distribution, different interfacial states are likely to develop. The slip distribution and the  $P\sim u$  relationship corresponding to different interfacial states are briefly interpreted below. Note that the strain but not slip at the free end of the carbon yarn was used in the derivation.

If the loaded end slip,  $u$ , is lower than  $s_{max}$ , the whole interface falls in the elastic state. Eq. (2.5) and Eq. (2.6) (shown in Table 2.3) can be used to predict the slip distribution and the  $P\sim u$  relationship can be determined, respectively. The bond stress decreases with increasing distance from the loaded end, and  $P$  increases as  $u$  increases.

If the loaded end slip reaches  $s_{max}$ , namely,  $u = s_{max}$ , debonding first occurs at the loaded end. With increasing  $u$ , debonding will propagate towards the free end, and the interface is in the

elastic-debonding state. The interface can be divided into the elastic part and the debonding part. The debonding and elastic parts are defined as  $l$  and  $L-l$ , respectively. Eq. (2.7) can be used to predict the slip in the debonding part, while the slip in the elastic part can be obtained by substituting  $L$  with  $L-l$  in Eq. (2.5). Note that the slip and tensile strain are continuous at the point connecting the elastic and debonding parts. The  $P\sim u$  relationship can then be derived, see Eq. (2.8) in Table 2.3.

After completing the elastic-debonding state, different interfacial states may develop with a further increment of  $u$ , depending on the magnitude of bond length. The Debonding portion of the bond-slip relationship will develop in the case that the bond length is sufficiently long, and the interface can have three parts, i.e. the elastic part ( $L-l-d$ ), the debonding part ( $l$ ) and the friction part ( $d$ ). Note that the slip and tensile strain at the point connecting the elastic part and the debonding part or connecting the debonding part and the friction part are continuous. Eq. (2.9) can be used to predict the  $P\sim u$  curve in the elastic-debonding-friction state. The Debonding portion in the bond-slip relationship cannot fully develop for a short bond length, and the elastic-debonding-friction state appears. The slip distribution and the  $P\sim u$  relationship for the short bond length in the debonding state can be expressed by Eq. (2.10) and Eq. (2.11) in Table 2.3, respectively.

When the slip along the whole interface exceeds  $s_{max}$  and  $u$  is higher than  $s_0$ , there are the debonding part and the friction part on the interface. Eq. (2.12) and Eq. (2.13) can be used to predict the slip distribution and the  $P\sim u$  curve, respectively.

If the slip along the whole interface exceeds  $s_0$ , it is easy to solve the governing equation by inserting the friction branch of the bond slip relationship. The slip distribution and the  $P\sim u$  curve can be predicted by Eq. (2.14) and Eq. (2.15), respectively.

### 2.3.3 Analytical extraction of the bond slip relationship

With the analytical formulation of the  $P\sim u$  relationship, it is possible to determine the bond parameters necessary for defining the bond-slip relationship based on the experimentally obtained  $P\sim u$  curve. The necessary bond parameters have at least four parameters,  $k_1$ ,  $k_2$ ,  $\tau_{max}$  and  $\tau_0$  (see Fig. 2.5). Then, several major characteristics of the experimental  $P\sim u$  curve are extracted and used to determine the bond parameters. The slope,  $K_1$ , which differs from  $k_1$  in the bond-slip relationship, of the initial linear increasing part in the  $P\sim u$  curve can be extracted. Eq. (2.16) is valid according to Eq. (2.6). With solving Eq. (2.16),  $\lambda_1$  can be calculated and further  $k_1$  can be determined according to Eq. (2.5a).

$$K_1 = EA\lambda_1 \tanh(\lambda_1 L) \quad (2.16)$$

In the case of a short bond length, the decreasing branch of the  $P\sim u$  curve can be predicted by Eq. (2.11). The condition for judging a short bond length will be discussed later. Eq. (2.17) can be obtained based on Eq. (2.11).  $K_2$  is the slope of the post-peak decreasing branch of the  $P\sim u$  curve.  $k_2$  can be calculated by Eq. (2.7a) upon solving Eq. (2.17).

$$K_2 = EA\lambda_2 \tan(\lambda_2 L) \quad (2.17)$$

As the maximum force may occur corresponding to the elastic-debonding state for a short bond length, the  $P\sim u$  curve around the peak force can be predicted by Eq. (2.8). During the debonding process, debonding propagates from the loaded end towards the free end, while  $P$  is close to a level that can be calculated by Eq. (2.18).

$$P = \frac{c\tau_{max} \sin(\lambda_2 L)}{\lambda_2} \quad (2.18)$$

By replacing  $P$  with  $P_{max}$ ,  $\tau_{max}$  can be obtained by Eq. (2.19).

$$\tau_{max} = \frac{P_{max} \lambda_2}{c \sin(\lambda_2 L)} \quad (2.19)$$

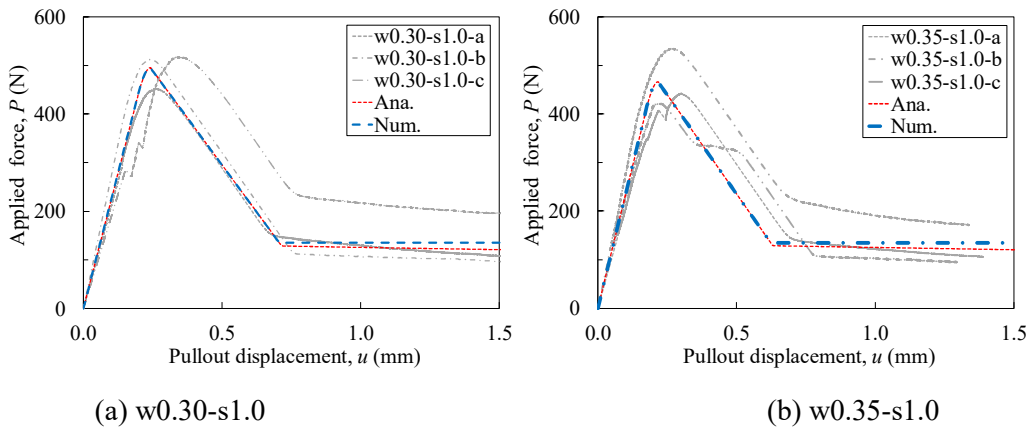
In the final interfacial state,  $P$  does not vary significantly with  $u$ , which can be predicted by Eq. (2.15). As  $u$  is much smaller in comparison to the bond length,  $\tau_{max}$  can be obtained by Eq. (2.20).

$$\tau_0 = \frac{P_0}{cL} \quad (2.20)$$

where  $\tau_0$  is the residual bond strength, and  $P_0$  means the applied force corresponding to the point where the last branch of the  $P\sim u$  curve initiates.

#### 2.3.4 Verification of the evaluated bond slip relationship

The necessary bond parameters for defining the trilinear bond-slip relationship can be obtained according to the above evaluation process. Table 2.2 shows the evaluated bond parameters for all the specimens. The  $P\sim u$  curve can be obtained using the different expressions for the  $P\sim u$  relationship shown in Table 2.3 and the evaluated bond parameters. An average  $P\sim u$  curve was predicted for each matrix using the average evaluated bond parameters and the average geometrical properties. Fig. 2.6 compares the analytical results and experimental  $P\sim u$  curves for all the specimens. There is a reasonable agreement between the analytical and experimental results, which confirms that the proposed evaluation process is reliable to obtain the trilinear bond-slip relationship. Besides, the bond at the carbon yarn-cementitious matrix interface is further found to be able to be represented by a trilinear bond-slip relationship for various cementitious matrices.



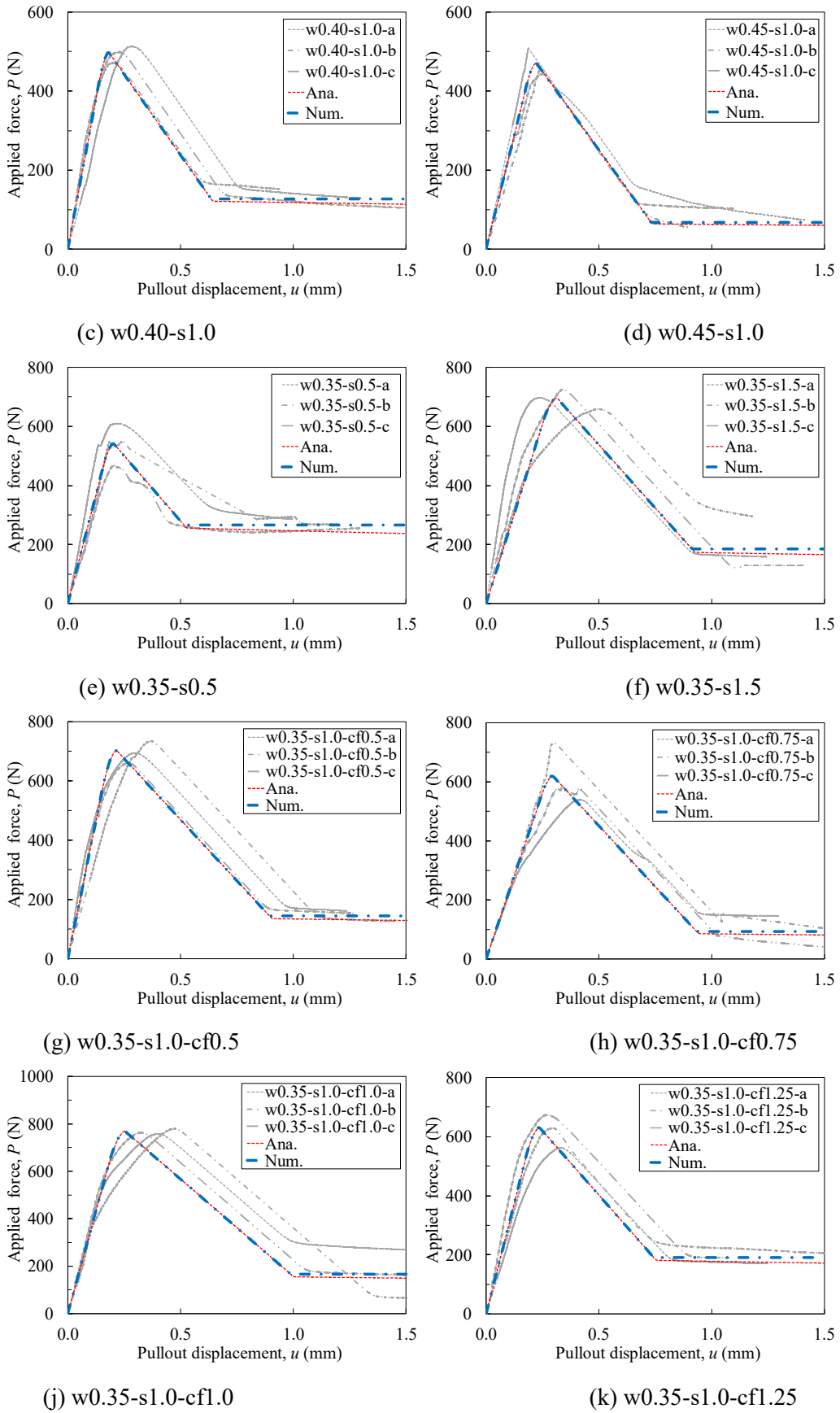


Fig. 2.6 Comparison between the experimental, analytical and numerical results for pullout specimens made of different matrices

Fig. 2.7 presents the impacts of test parameters on the bond-slip relationship between carbon yarn and the cementitious matrix. Each curve is plotted by taking the average values of the bond parameters obtained from three parallel specimens. A minor difference in the bond-slip relationships is seen for  $w/c$  ranged from 0.3 to 0.4, except a reduction of 0.4 MPa in the residual bond strength for  $w/c$  increases from 0.4 to 0.45.

Fig. 2.7(b-c) shows that the maximum bond stress,  $\tau_{max}$ , rather than other parameters is most affected by  $s/c$  and content of the short cut carbon fibers ( $cf$ ). A small decrease in  $\tau_{max}$  is seen with increasing  $s/c$  from 0.5 to 1.0, while a further increment in  $s/c$  leads to an improvement in  $\tau_{max}$ . The improvement may be due to that the presence of sand can prevent shrinkage-induced cracks on the interface between the carbon yarn and matrix. There is an improvement in  $\tau_{max}$  for  $cf$  varied from 0 to 0.75%, while a further increment results in a reduction in  $\tau_{max}$ . The positive effect of the inclusion of short fibers can be explained by the cross-linkage theory (Hartig 2011). The presence of short fibers in the matrix may result in more cross-links connecting the carbon yarn to the matrix and thus improve the bond at the carbon yarn-matrix interface. Apart from that, a larger amount of  $cf$  above 0.75% leads to more air bubbles in the fresh matrix during mixing, and the matrix becomes more porous and therefore the bond strength of the interface is reduced.

## 2.4 Determination of $L_a$ for the embedded carbon yarn

### 2.4.1 Numerical simulation of the pullout curve

Numerical simulation was conducted to validate the reliability of the proposed method of obtaining bond parameters and to model pullout curves for different bond lengths. The interfacial governing equation as a second-order differential equation (Eq. (2.2)) can be numerically solved by introducing boundary conditions and the known bond-slip relationship. Provided that a displacement,  $u$ , is applied to the loaded end of the carbon yarn, the slip distribution and the tensile strain can be obtained with a numerical method. Further,  $P$  can be obtained for different levels of  $u$ , and therefore the whole  $P$ - $u$  curve can be modeled. The numerical method used is shown as follows.

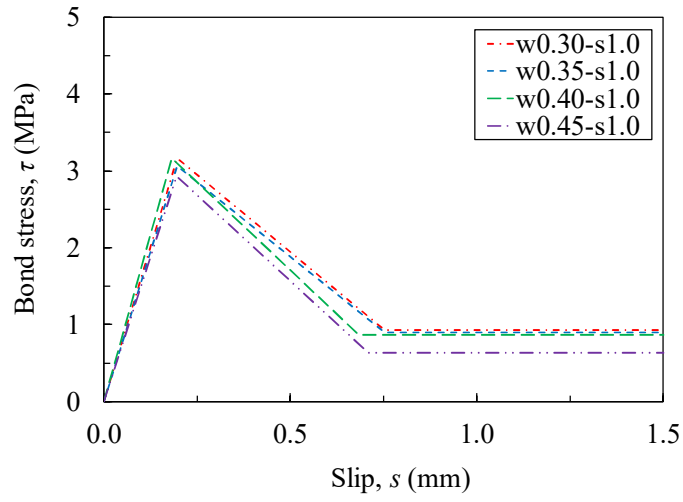
The entire bond length of the carbon yarn can be discretized into  $n$  equal pieces with  $n+1$  nodes. The starting node numbered '1' is defined at the free end, while the ending node ' $n+1$ ' at the loaded end. For any node  $i$ , Eq. (2.21) is valid as per Eq. (2.2).

$$\left( \frac{d^2 s}{dx^2} \right)_i - \left( \frac{c\tau(s)}{EA} \right)_i = 0 \quad (2.21)$$

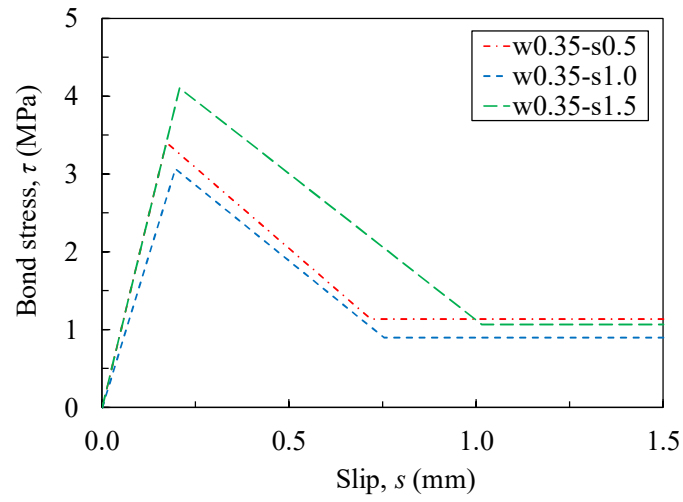
With a finite difference method, Eq. (2.21) can be transformed into

$$s_i = \frac{1}{2} \left( s_{i+1} + s_{i-1} - \frac{c\tau(s_i)}{EA} \Delta x^2 \right) \quad (2.22)$$

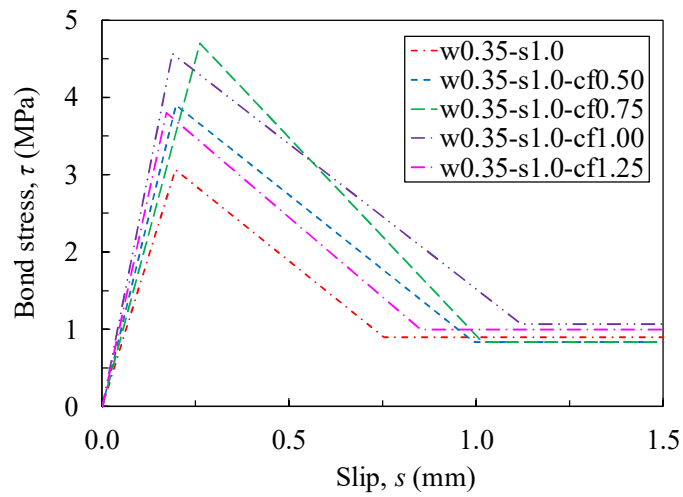
where  $s_{i-1}$ ,  $s_i$  and  $s_{i+1}$  correspond to the slip of three neighboring nodes  $i-1$ ,  $i$  and  $i+1$ , respectively; and  $\Delta x$  is the interval length.



(a) The effects of  $w/c$



(b) The effects of  $s/c$



(c) The effects of  $cf$

Fig. 2.7 The effects of the test parameters on the bond slip relationship of the carbon yarn embedded in the matrix, including (a)  $w/c$ , (b)  $s/c$  and (c)  $cf$

According to Eq. (2.3) and Eq. (2.4), the boundary conditions at the free end and the loaded end can be expressed by Eq. (2.23) and Eq. (2.24), respectively.

$$\left(\frac{ds}{dx}\right)_{s_1} = 0 \quad (2.23)$$

$$S_{n+1} = u \quad (2.24)$$

Eq. (2.21) can be solved following an iteration process, and thus the slip at any node can be obtained. Further, the bond stress at any node can also be calculated. The pullout force can be obtained by integrating the bond stress over the carbon yarn's bond length, see Eq. (2.25).

$$P = \int c\tau(x)dx \quad (2.25)$$

With the finite difference method, Eq. (2.26) is used to calculate the pullout force.

$$P = c \left( \frac{\tau_1 + \tau_{n+1}}{2} + \sum_{i=2}^n \tau_i \right) \Delta x \quad (2.26)$$

where  $\tau_i$  means the bond stress at node  $i$ .

Hence, the above numerical method can establish the relationship between  $P$  and  $u$ .

Fig. 2.6 compare the  $P\sim u$  curve obtained from the analytical derivation, numerical simulation and experiments. The analytical and numerical results overlap, and both predict well the experimental curves, indicating the reliability of the proposed method of obtaining the bond parameters.

Besides, three additional specimens with a bond length of 30 mm were tested and analyzed to demonstrate the capability of the numerical method to simulate the  $P\sim u$  curve with a long bond length. These three specimens were made of the matrix w0.30-s1.0 and tested under the same conditions. these specimen lengths exhibited the failure by tensile fracture of the carbon yarn but not fiber slippage. Fig. 2.8 plots the  $P\sim u$  curves for the specimens with a bond length of 30 mm.

The  $P\sim u$  curve for these specimens was numerically modeled with adopting the evaluated bond parameters for the same matrix. There is a good agreement between the numerical simulation and the experimental results, indicating that the same bond parameters can be used to predict the  $P\sim u$  curves of pullout specimens up to the point of tensile fracture of the carbon yarn. Dalalbashi et al. reported the effect of the embedded length on the pullout behavior of the TRM (textile reinforced mortar) made of steel fiber and the extracted bond slip law is similar for different embedded lengths (Dalalbashi et al. 2018a). The bond-slip relationship is said to be a material parameter that should be independent of the fiber's geometrical aspects; and the pullout behavior of the steel fiber in the matrix with different fiber radii and embedded lengths has been successfully simulated with the same bond-slip relationship (Banholzer et al. 2006). Zhang analytically modeled the pullout curve of glass yarn in a matrix with two bond lengths with the same bond-slip relationship (Zhang et al. 2014). Portals et al. calibrated the local bond-slip behavior of basalt and carbon textiles in TRC for a short bond length (35 mm for basalt and 25

mm for carbon) and employed the calibrated bond slip model as a basic material property in 1D and 3D modeling of pullout specimens with long bond lengths, which led to a good prediction of the experimental results (Williams Portal et al. 2014). Therefore, it is reasonable to utilize the same bond slip relationship to simulate the pullout behavior for different bond lengths.

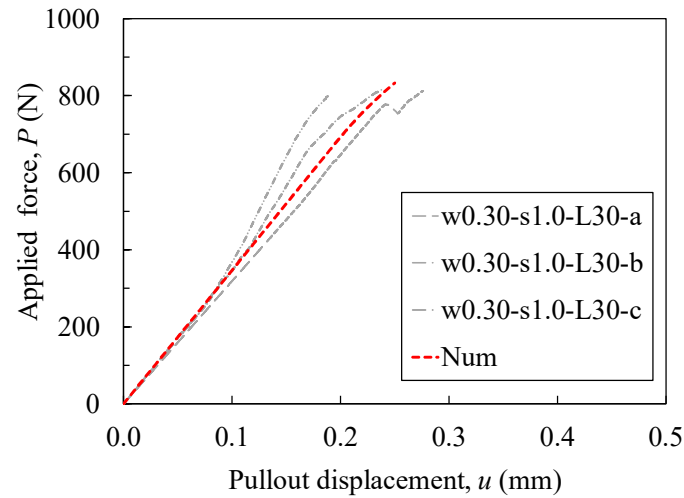


Fig. 2.8 Comparison between the experimental and numerical results for specimens made with Matrix w0.3-s1.0 and with a bond length of 30 mm

#### 2.4.2 Numerical determination of $L_a$

For reinforcements externally bonded to concrete, there exists an important concept of the effective bond length,  $L_{eff}$ , which is defined as a bond length beyond which the bond strength does not increase with a further increment of the bond length (Chen and Teng 2001; Dai et al. 2006). As for the embedded reinforcement, however,  $L_{eff}$  does not exist, while a bond length can always be found so that the reinforcement's tensile capacity can be reached. This is due to that significant bond stress can develop even at large slips for the internal reinforcement, which is related to the friction along the interface. The critical embedment length,  $L_a$ , is defined as a minimum bond length required for the maximum pullout force to reach the tensile capacity of the internal reinforcement. Carbon yarn was embedded in the cementitious matrix and appeared like an internal reinforcement more than an external reinforcement. Therefore, the critical embedment length can always be found for the embedded carbon yarn.

##### 2.4.2.1 Evaluation of $L_a$ for the embedded carbon yarn

To accurately obtain  $L_a$  of the embedded carbon yarn from experimental tests is difficult, as  $L_a$  means a limit state where the bond strength equals the tensile capacity of the embedded carbon yarns. Either fiber slippage or fiber fracture rather than a limit state may appear in experiments. The above numerical method was employed to determine  $L_a$  for the embedded carbon yarn. The pullout curves were first obtained for carbon yarns with different bond lengths. The predicted maximum pullout force was then plotted against these bond lengths. At last,  $L_a$  can be obtained by equating the maximum pullout force with the tensile capacity of the carbon yarns. Fig. 2.9 plots the simulated  $P-u$  curves for carbon yarns with different bond lengths. The post-peak decreasing branch of the  $P-u$  curve behaves more abruptly, as the bond length is increased. The pullout displacement is the sum of the free end slip and the elastic deformation of the entire bond length, which equals the integral of the yarn's strain over the bond length. Provided that



the slip increases at the free end, a reduction in the loaded end strain in the decreasing branch of the  $P\sim u$  curve results in the reduced elastic deformation of the whole bond length. If the bond length is larger, there is a more significant reduction in the elastic deformation of the whole bond length, and thus the increase in the displacement at the loaded end is the smaller. The snapback behavior of the  $P\sim u$  curve discussed in (Focacci et al. 2017) cannot be captured in Fig. 2.9, because the displacement at the loaded end is subjected to a continuous increase.

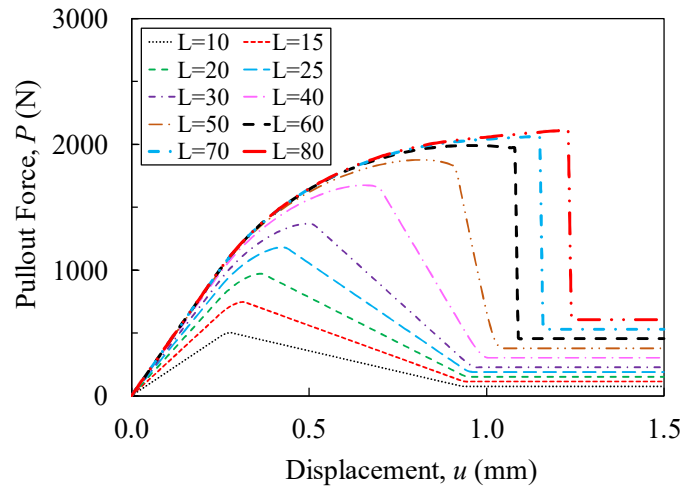


Fig. 2.9 The effect of the bond length on  $P\sim u$  curves for pullout specimens using the same bond slip relationship

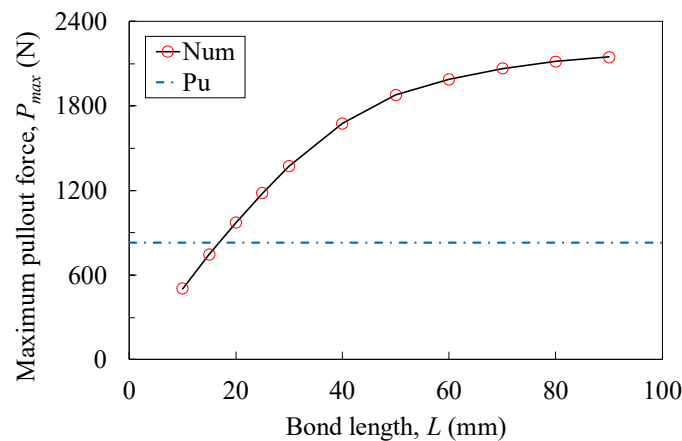


Fig. 2.10 Determination of  $L_a$  of carbon yarn in the matrix from numerical results

Fig. 2.10 presents a relationship between the simulated maximum pullout force and the bond length. The bond strength increases with increasing bond length while less increase is seen for larger bond lengths.

In the case of small bond lengths, the interfacial stress state at the peak pullout force is in the elastic-debonding state or debonding state, and the peak pullout force can increase significantly with an increase in bond length. For a long bond length, the interfacial state changes to the elastic-debonding-friction state, and a further increase in the bond length only results in an increase in the frictional component of the peak pullout force and thus a small increase in the peak pullout force.  $L_a$  can be calculated through linear interpolation with equating the bond strength with the tensile capacity of the carbon yarns. For example,  $L_a = 16.8$  mm can be

obtained for the embedded carbon yarn in the matrix, providing  $k_1 = 19.06$  MPa/mm,  $\tau_{\max} = 4.75$  MPa,  $k_2 = 5.94$  MPa/mm and  $\tau_0 = 0.7$  MPa.

### 2.4.3 A proposed approach for calculating $L_a$

As previously described, the analytical solution of the interfacial problem has been obtained in terms of the slip distribution and the  $P\sim u$  curve, see Table 2.3. The tensile capacity of the carbon yarns can be reached for a short bond length, and the interfacial state is the elastic-debonding state. The tensile strain of the embedded carbon yarn is equal to the first-order derivative of the slip with respect to  $x$ . In the elastic-debonding state, debonding starts at the loaded end and proceeds towards the free end, while the pullout force converges to a loading level, as shown in Eq. (2.18). By replacing the maximum pullout force with the yarn's tensile capacity,  $L_a$  can be calculated by Eq. (2.27).

$$L_a = \frac{1}{\lambda_2} \arcsin \left( \frac{P_u \lambda_2}{c \tau_{\max}} \right) \quad (2.27)$$

In the case of a relatively long bond length in which the first and the second portions of the trilinear bond-slip relationship can fully develop, Eq. (2.8) can be used to calculate the maximum pullout force. The maximum pullout force corresponds to the elastic-debonding state in which the bond stress along the whole interface is above  $\tau_0$ . Therefore, Eq. (2.28) can be obtained to calculate  $L_a$ .

$$L_a = \frac{1}{\lambda_1} \operatorname{arctanh} \left( \frac{\lambda_1}{\lambda_2} \frac{1}{\tan \left( \operatorname{arccot} \left( \frac{P_u \lambda_2}{c \tau_0} \right) + \lambda_2 l_1 \right)} \right) + l_1 \quad (2.28)$$

$$l_1 = \frac{1}{\lambda_2} \arcsin \left( -\frac{\tau_0}{\tau_{\max}} \right) + \frac{\pi}{2\lambda_2} \quad (2.28a)$$

Where  $l_1$  denotes the bond length required to fully develop the debonding portion of the bond slip relationship according to (Carozzi et al. 2016) and can be used as a condition for judging whether the bond length is short or long and whether the elastic-debonding-friction state or the debonding state occurs following the elastic-debonding state.

If complete activation of the first and second portions of the trilinear bond-slip relationship cannot provide a sufficiently large bond strength to assure the occurrence of tensile failure of the embedded carbon; the third portion of the bond-slip relationship must be activated. Therefore, the interfacial state at the tensile failure of the carbon yarn will correspond to the elastic-debonding-friction state, and the maximum pullout force should be obtained so that the bond stress along the entire interface is larger or equal to  $\tau_0$ . Eq. (2.29) can then be derived to calculate  $L_a$ .

$$L_a = \frac{1}{c\tau_0} \left( P_u - \frac{c\tau_{max}}{\lambda_2} \sqrt{1 + \frac{\lambda_2^2}{\lambda_1^2}} \right) + l_1 + l_2 \quad (2.29)$$

$$l_2 = \frac{1}{\lambda_1} \operatorname{arccosh} \left( \frac{2\tau_{max}}{\tau_0} \right) \quad (2.29a)$$

where  $l_2$  denotes the length of the elastic portion along the interface, in which the bond stress is larger than  $\tau_0$ .

Therefore, an approach to calculate  $L_a$  has been established based on the above discussion. Fig. 2.11 shows the approach to calculate  $L_a$  with inputting the material and geometrical properties. Based on the evaluated bond parameters,  $L_a$  was calculated for each matrix and then compared with the numerical results. Calculated  $L_a$  overlaps with the numerical results, indicating the reliability of the proposed approach. Calculated  $L_a$  using the approach shown in Fig. 2.11 is shown in Table 2.2 for each specimen.

#### 2.4.4 Parametric study on effects of bond parameters on $L_a$

The effects of bond parameters on the  $L_a$  of the embedded carbon yarn will be addressed in this section. It requires four bond parameters, i.e.,  $k_1$ ,  $k_2$ ,  $\tau_{max}$  and  $\tau_0$  to fully define the bond slip relationship. When one out of the four bond parameters is analyzed, other parameters are fixed. For instance, the average values of the bond parameters for matrix w0.35-s1.0-cf0.75 were used as a reference in the parametric study.

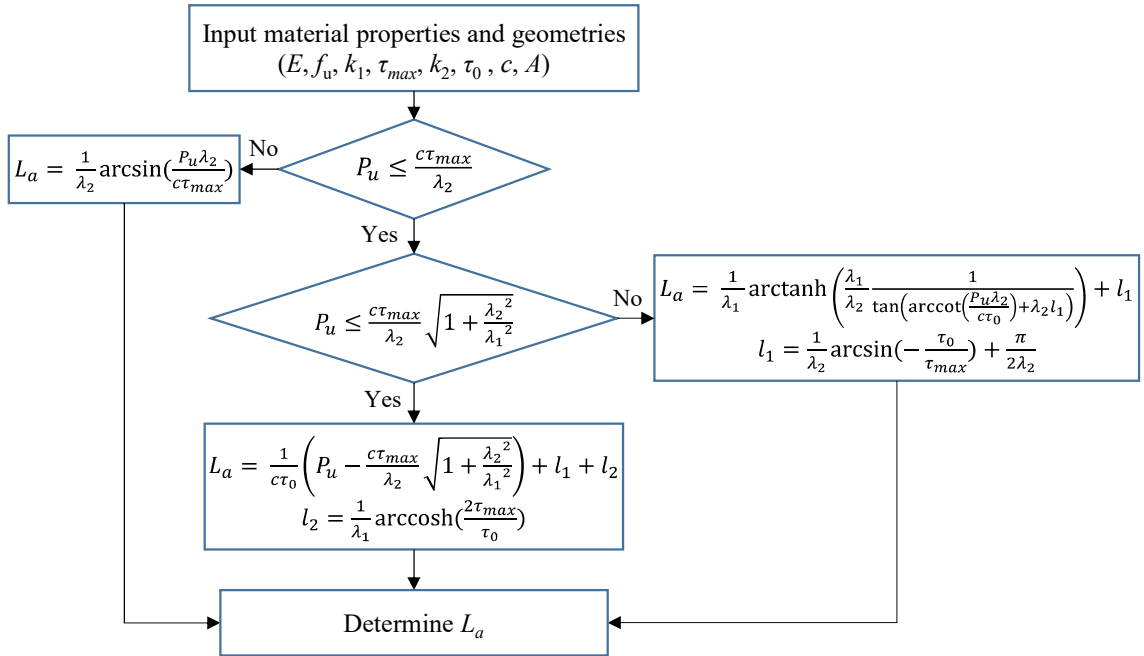


Fig. 2.11 The proposed approach for evaluating  $L_a$

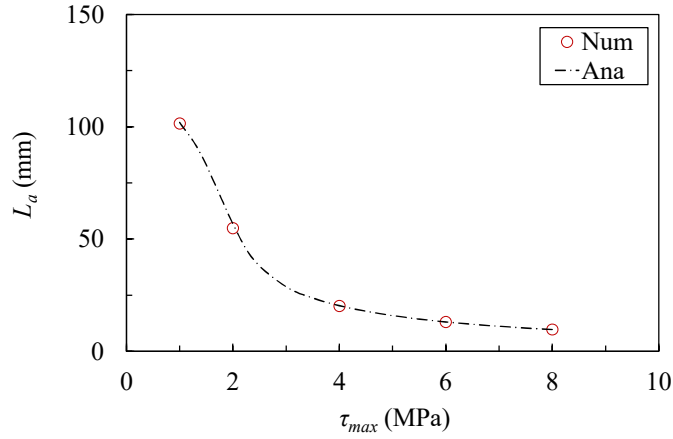
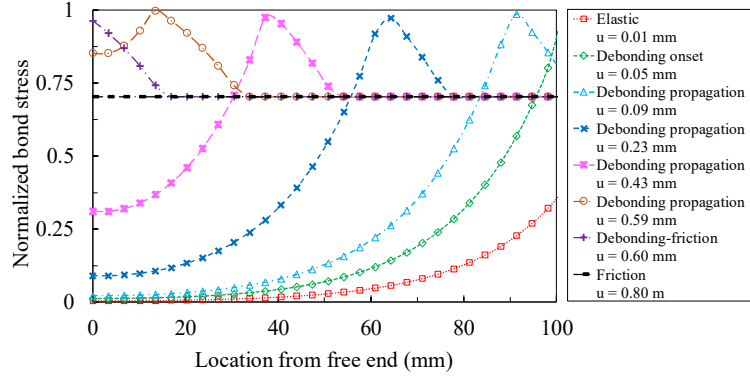


Fig. 2.12 The effect of  $\tau_{max}$  on  $L_a$  of carbon yarn in the cementitious matrix

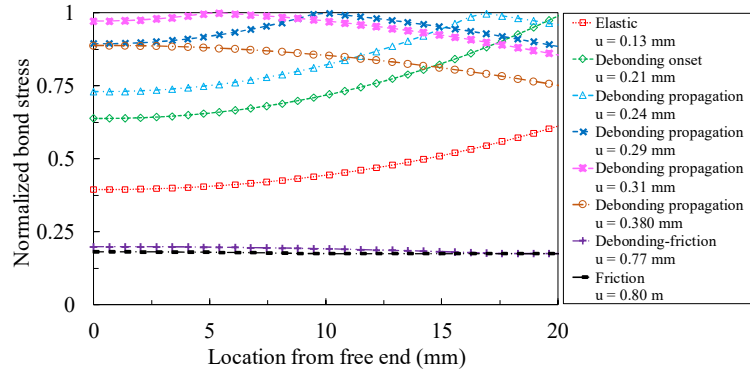
Fig. 2.12 shows the effect of  $\tau_{max}$  on  $L_a$ .  $L_a$  decreases significantly with  $\tau_{max}$  increasing from 1 MPa to 3 MPa, and a further increment in  $\tau_{max}$  leads to a slight reduction in  $L_a$ . The effects of  $\tau_{max}$  on  $L_a$  may be explained according to the load transfer from the carbon yarn to the matrix. Fig. 2.13 describes the distribution in bond stress along  $L_a$  for different  $\tau_{max}$  obtained from numerical modeling. The simulated bond stress is normalized to  $\tau_{max}$ . When  $\tau_{max}$  is small, the interfacial stress state at the tensile failure of the yarn is in the elastic-debonding-friction state, and increasing  $\tau_{max}$  leads to an improvement in the elastic- and debonding- components of the bond strength, thus causing a significant reduction in  $L_a$ . For a large  $\tau_{max}$ , a short bond length is enough to ensure the occurrence of the tensile failure of the carbon yarn. According to Fig. 2.13 (b-c) the bond stress distribution becomes more uniform with increasing  $\tau_{max}$ . Thus,  $L_a$  decreases slightly for larger  $\tau_{max}$ . At the beginning of loading, the entire interface falls in the elastic state, and the bond stress decreases towards the free end of the carbon yarn. Then, debonding initiates at the loaded end if  $\tau_{max}$  is attained and propagates towards the free end with increasing displacement. Whether the interface falls into the elastic-debonding-friction state (Fig. 2.13(a)) or the debonding state (Fig. 2.13(b-c)) is dependent on the bond length. For the former state, friction will appear when  $s_0$  is reached at the loaded end and proceed to the free end. As for the latter state, the interface remains in the debonding state and bond stress decreases with increasing displacement. At last, the friction state appears along the entire interface and the bond stress becomes constant.

Fig. 2.14 presents the effect of  $k_1$  on  $L_a$ . The elastic-debonding state occurs at the failure of the embedded carbon yarn, and the bond stress profile resembles the case in Fig. 2.13(b). There is a nearly constant value of  $L_a$  for  $k_1$  in the range of 5-40 MPa/mm.

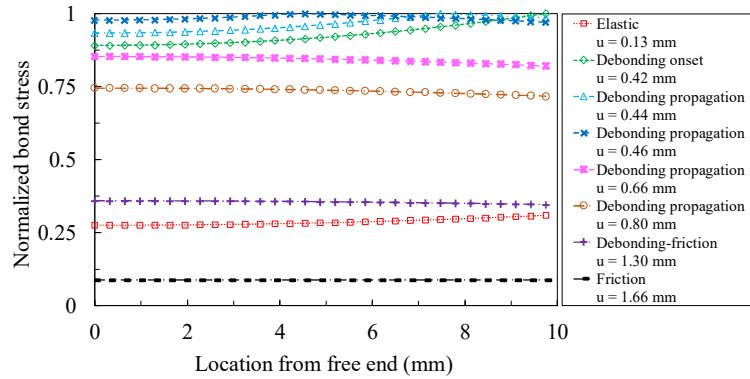
Fig. 2.15 and Fig. 2.16 show the effects of  $k_2$  and  $\tau_0$  on  $L_a$  of the embedded carbon yarn, respectively. No much difference can be seen in  $L_a$  with varying  $k_2$  (0-20 MPa/mm) and  $\tau_0$  (0.5-2.5 MPa). The interfacial state becomes the elastic-debonding state or the debonding state corresponding to the failure of the embedded carbon yarn, as shown in Fig. 2.13(b-c). This is to say  $L_a$  is mainly affected by  $\tau_{max}$ .



(a)  $\tau_{max} = 1$  MPa



(b)  $\tau_{max} = 4$  MPa



(c)  $\tau_{max} = 8$  MPa

Fig. 2.13 Bond stress profile along the carbon yarn's critical embedment length with different  $\tau_{max}$  of (a) 1 MPa, (b) 4 MPa and (c) 8 MPa

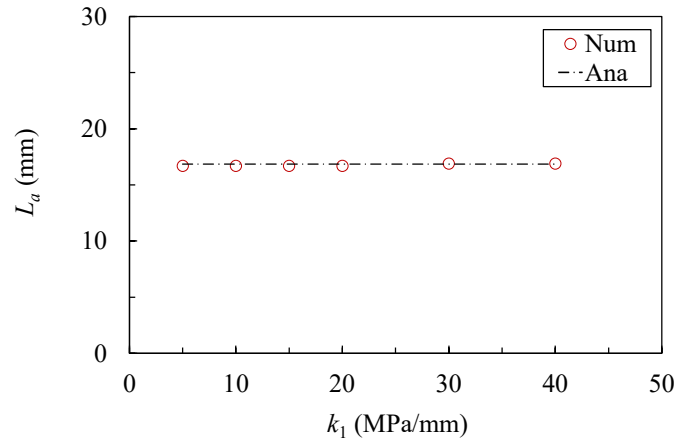


Fig. 2.14 The effect of  $k_1$  on  $L_a$  of carbon yarn in the cementitious matrix

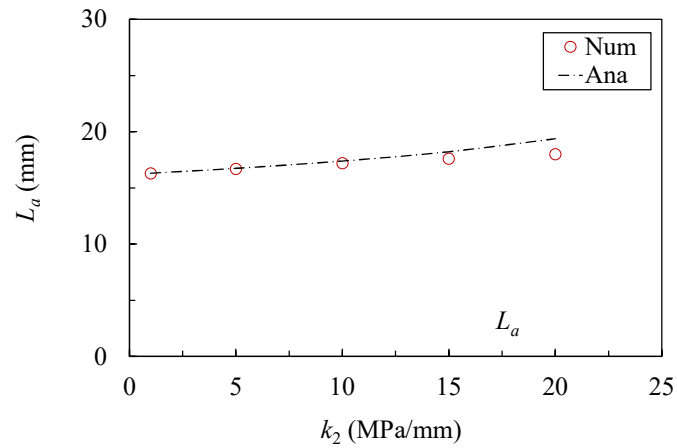


Fig. 2.15 The effect of  $k_2$  on the value of  $L_a$  of carbon yarn in the cementitious matrix

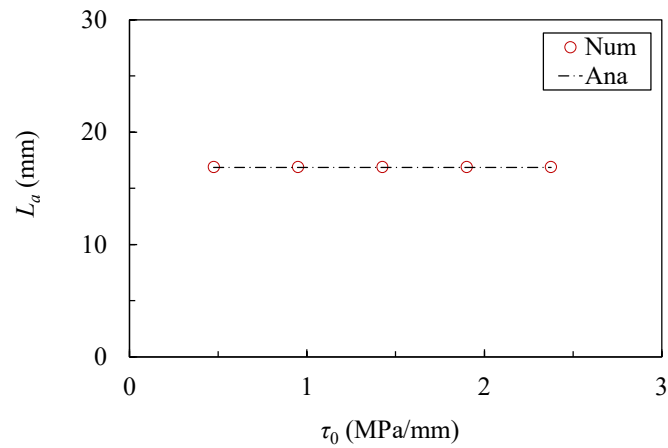


Fig. 2.16 The effect of  $\tau_0$  on the value of  $L_a$  of carbon yarn in the cementitious matrix

## 2.5 Conclusions of this chapter

Based on the test results and analyses, the following conclusions can be drawn in this chapter. The pullout behavior is similar for all the pullout specimens, which can be characterized by an increasing branch and the descending branch following by a slowly decreasing tail. Also, the

failure is due to the slippage of carbon yarn through the matrix for all the specimens with a bond length of 15 mm.

The bond parameters for defining the bond slip relationship were obtained for all the pullout specimens through an analytical method that is based on the analytical solution of the  $P-u$  curve. With the analytical solution, the main features of the  $P-u$  curves were used to determine the bond parameters. Good agreement between analytical modeling and test results indicates the applicability of the trilinear bond behavior for the carbon yarn-matrix interface and the reliability of the method to determine the bond parameters.

The type of matrix affects the bond behavior between carbon yarn and matrix. A minor difference can be seen in the bond slip relationship for  $w/c$  increasing from 0.30 to 0.45. While for  $s/c$ , and  $cf$ ,  $\tau_{max}$  instead of other bond parameters was affected significantly. As  $s/c$  increases from 0.5 to 1.0, there is a slight decrease in  $\tau_{max}$  but a further increment of  $s/c$  results in a considerable improvement in  $\tau_{max}$ . There is an increase in  $\tau_{max}$  for  $cf$  in the range of 0 to 0.75%, while a reduction with a further increment of  $cf$ .

Based on the analytical solution of the interfacial governing equation, an approach has been developed to calculate  $L_a$  of the carbon yarn embedded in the matrix with inputting material properties and geometries. The reliability of the proposed approach has been verified through a comparison of  $L_a$  obtained from the approach and numerical modeling.

Besides, the effects of bond parameters on  $L_a$  have been explored based on a parametric study. It can be found that  $\tau_{max}$  becomes the most affecting factor for determining  $L_a$ .

## Symbols

$A$ : the cross-sectional area of a single carbon yarn;

$c$ : the perimeter of a single carbon yarn, which is taken as two times the width of the yarn;

$cf$ : the content of short-cut carbon fibers in the cementitious matrix, which is expressed in the amount of mass of cement;

$E$ : Young's modulus of the carbon yarn obtained from axial tensile test;

$f_{mc}$ : the compressive strength of the cementitious matrix;

$f_{ml}$ : the flexural strength of the cementitious matrix;

$L$ : the bond length of the carbon yarn;

$L_a$ : the critical embedment length of the embedded carbon yarn;

$P$ : the applied force carried by the embedded carbon yarn during pullout test;

$P_{max}$ : the peak applied force carried by the embedded carbon yarn during pullout test;

$P_u$ : the tensile capacity of the carbon yarn;

$s$ : the slip of the carbon yarn embedded in the cementitious matrix;

$s/c$ : the sand to cement ratio in weight;

$u$ : the pullout displacement which is defined as the slip of the embedded carbon yarn at the loaded end;

$b$ : the width of the carbon yarn;

$w/c$ : the water to cement ratio in weight;

$\sigma$ : the tensile stress in the carbon yarn;

$\tau$ : the local bond stress of the carbon yarn;

$\tau_m$ : the average bond strength estimated by dividing the  $P_{max}$  by the bond area.

$k_1$ ,  $k_2$ ,  $\tau_{max}$  and  $\tau_0$ : the bond parameters involved in the trilinear BSR, which mean the slope of the first linear part, the absolute value of the slope of the second linear part, the maximum bond stress and residual bond stress.



## Chapter 3

### 3 Bond behavior of carbon fabric in cementitious matrix with considering matrix impregnation

#### 3.1 Introduction

The carbon fabric made of the multifilament carbon yarns is normally embedded in the cementitious matrix with a so-called dry state. The dry state herein means that there is no impregnation of the fabric with the organic matrix, such as epoxy resin. Due to the geometrical mismatch between free spacing among filaments and particle size of cement grains, the cementitious matrix cannot completely penetrate the fabric, leading to varying bond property across the cross-section of the yarn. The filaments within the carbon yarn can be grouped into two parts, i.e. outer part in which the filaments are adhered to the matrix and receive a strong bond between the matrix and inner part where the filaments are not in contact with the matrix and the stress transfer is due to the presence of inter-filament friction. Thus, the limited matrix impregnation complicates the bond between fabric and matrix.

To characterize the bond at the fabric-matrix interface, pullout tests (Xu et al. 2004; Banholzer 2006; Sueki et al. 2007; Peled et al. 2008; Lorenz and Ortlepp 2011; Zhang et al. 2013, 2014; Williams Portal et al. 2014; D'Antino et al. 2017; Dalalbashi et al. 2018a, 2018b; Lancioni et al. 2017; Zhu et al. 2018) were conducted in which the carbon yarn was gradually pulled through the matrix. Further, the bond slip relationship can be determined for the embedded fabric while the yarn was simplified as a monolithic reinforcing bar (Xu et al. 2004; Sueki et al. 2007; Lorenz and Ortlepp 2011; Lancioni et al. 2017; Williams Portal et al. 2014; Zhang et al. 2013, 2014; Zhu et al. 2018; Dalalbashi et al. 2018a; b). Such simplification may be valid when sufficient shear stress can be transferred among different filaments, like the thin and compact carbon yarn before manufacturing to the fabric. When the bond length is sufficiently long, the tensile failure of the yarn is likely to occur, as shown in Chapter 2. An approach described in Chapter 2 has been proposed to calculate the critical embedment length of the carbon yarn based on the geometries and material properties.

In the case of the fabric or textile in FRCM composites, the bond and failure mechanisms are more complex due to the random and partial matrix impregnation, which is different from the case described in Chapter 2. The partial matrix impregnation leads to varying bond characteristics of different filaments within an embedded carbon yarn and thus causes filaments to fail in a progressive manner in which the outermost filaments fail at first; such failure phenomenon is a so-called telescopic failure. The telescopic failure has been examined using FILT (Failure Investigation using Light Transmission properties) tests for the AR-glass filaments in the cementitious matrix (Banholzer 2006). Considering the heterogeneous nature between the carbon fabric and the cementitious matrix, a similar failure behavior can be expected. However, there is currently no available information regarding the bond between carbon fabric and cementitious matrix, which is influenced and complicated by the limited matrix impregnation. In addition, to quantify the degree of matrix impregnation into the multifilament carbon yarn is still a problem to be addressed.

The objective of this chapter is to investigate the complex bond between carbon fabric and cementitious matrix with the aim at clarifying the effects of matrix impregnation. Pullout tests were conducted on the FRCM composite specimens with different embedded lengths (30, 50 and 70 mm). In order to evaluate the degree of matrix impregnation, i.e. the percentage of the outer (impregnated) part, the number of the pullout filaments were analyzed with the help of an image processing and analysis technique. As the carbon yarn is subdivided into two parts (outer and inner parts), two types of interfaces are introduced in the carbon yarn-matrix system, i.e. the outer interface between the matrix and the outer part and the inner interface between the outer part and inner part. Subsequently, the bond parameters for different interfaces were determined in an analytical method based on pullout test results. Finite element modeling was then performed to model the pullout behavior of the specimens to verify the reliability of the proposed method and the accuracy of the obtained bond slip relationships. The load transfer and contribution of outer and inner parts to carrying the applied force as well as the effects of key parameters were also discussed.

## 3.2 Experimental investigation

### 3.2.1 Raw materials and carbon FRCM composite

A bidirectional carbon fabric consisting of carbon yarns disposed in two orthogonal directions was used. Fig. 3.1 shows the geometries of the carbon fabric. There are 12000 carbon filaments within each bundle of carbon yarn in both directions, and the diameter of each filament is 7 microns. The mesh size and the yarns' width were measured at 20 locations and then taken as the average values of the measurements. The fabric's mesh size measured 6.49 mm × 5.00 mm, and the width was 3.29 and 2.36 for the warp and weft yarns, respectively. Uniaxial tests were carried out to obtain the tensile properties of the warp carbon yarn according to GB/T 3362-2005. The obtained tensile strength and Young's modulus of the warp yarns are, respectively, 2077 MPa and 181 GPa.

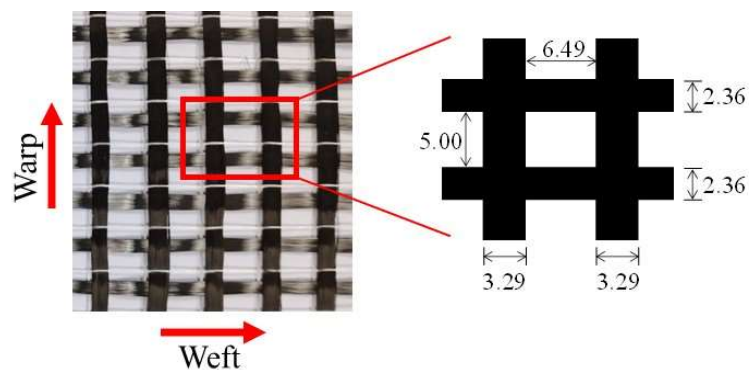


Fig. 3.1. Geometrical properties of the carbon fabric

The cementitious matrix had a  $w/c$  of 0.40 and  $s/c$  of 1.0. Normally, the maximum size of the aggregate is less than 1-2 mm, which leads to a finely grained matrix that allows good penetration through the fabric's mesh. According to ISO 679:2009 2009, three-point bending tests were carried out on three matrix prismatic specimens (40 mm × 40 mm × 160 mm) cured

after 28 days to determine the flexural tensile strength. After bending tests, each prismatic specimen was fractured into two halves which were tested under compression to obtain the compressive strength. The flexural and compressive strengths of the matrix are, respectively, 6.3 MPa and 74.1 MPa.

Carbon FRCM composites used in this study were the cementitious matrix reinforced by a layer of carbon fabric. A specially designed and fabricated wooden formwork was employed to cast FRCM composite panels with a dimension of 500 mm × 300 mm × 10 mm. A wet lay-up procedure was following in casting the composites: i) A first matrix layer of 5 mm thickness was placed and leveled on the base of the formwork; ii) a layer of carbon fabric was spread and slightly pressed on the first matrix layer; and iii) a matrix layer was finally applied and troweled. After casting, the panels were wrapped using plastic cover to prevent water evaporation. The panels were moved and cured in a chamber (100% RH and 20 °C) after demolding.

### 3.2.2 Specimen preparation and test implementation

There are two types of pullout tests in the existing literature to characterize the bond between fabric and matrix, i.e. one-sided and double-sided pullout tests. For one-sided pullout tests (Banholzer 2006; Dalalbashi et al. 2018a; b; Sueki et al. 2007; Zhang et al. 2013, 2014), one end of the yarn was embedded in the matrix, and the other end was coated with resin for clamping. The applied axial load transferred from the carbon yarn to the matrix through the bond at the yarn-matrix interface. In the case of the double-sided tests. As for the double-sided tests developed in (Lorenz and Ortlepp 2011; Williams Portal et al. 2014; Xu et al. 2004), the yarn's both ends were embedded in the matrix in a symmetrical or unsymmetrical configuration, while the applied load transferred from the matrix to the fabric. The choice of the unsymmetrical configuration allows the bond failure to occur on the side of the short embedded length, and the long embedded length can be sufficiently anchored.

The geometrically unsymmetrical configuration of pullout specimens for double-sided pullout tests is presented in Fig. 3.2. There was a layer of carbon fabric embedded in the matrix prism with a dimension of 200 mm × 30 mm × 10 mm, with each specimen containing three carbon yarns in the warp direction. The specimens' asymmetry was achieved by introducing an upper cut that cut off the middle carbon yarn to be studied and a pair of cuts that only kept the middle yarn intact. There are two matrix blocks in each specimen, i.e. the bond block (upper) with a short embedded length,  $L_a$ , and the anchorage block (lower) with a long anchoring length,  $L_b$ . Therefore, the first failure can be expected on the embedded length. Various embedded lengths of 30, 50 and 70 mm were studied, and the corresponding anchoring lengths were 170, 150 and 130 mm. The specimens were numbered according to their embedded length, e.g. L30 means an embedded length of 30 mm.

Fig. 3.2 shows the setup for double-sided pullout tests, where the specimen was fixed by clamping the matrix on its both extreme ends. CFRP sheets were applied to both ends with epoxy resin to avoid clamping-induced damage. Pullout tests were performed on a universal electronic testing machine with a loading capacity of 10 kN. The load was applied under a displacement-controlled mode with a rate of 0.2 mm/min. The applied force was measured by a loading cell with an accuracy of 1 N, while two clip-on extensometers (gauge length: 50 mm; accuracy: 0.001 mm) were used to measure the opening at the point between the bond and

anchorage block; the opening is also called the pullout displacement. The point was defined as the loaded end for both the embedded and anchorage length for the carbon yarn, while the opposite end was the free end. The pullout displacement was equal to the sum of the loaded end slip of the embedded and anchoring length.

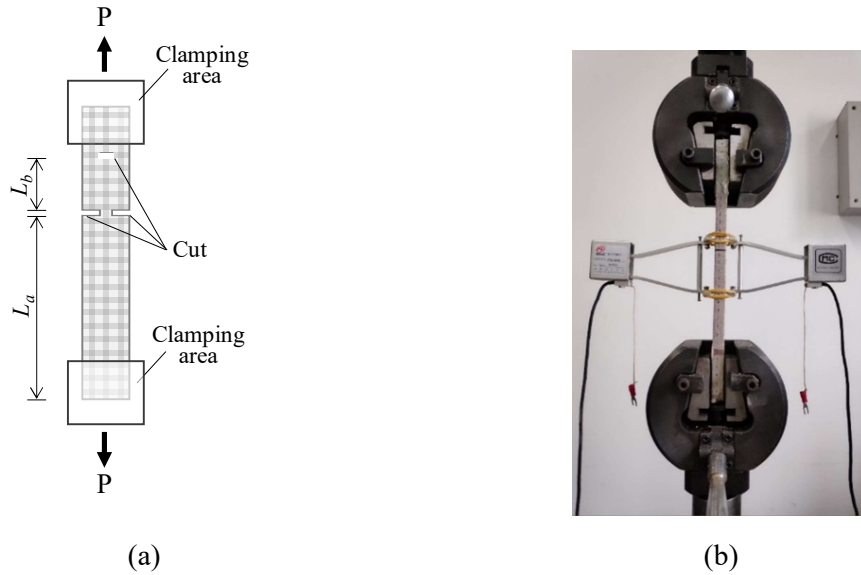


Fig. 3.2. Specimen configuration (a) and test setup (b) of double-sided pullout tests

### 3.2.3 Test results

Before describing the failure, the heterogeneity in the carbon yarn-matrix interface was presented. It is well known that the fabric cannot be fully penetrated by the cementitious matrix. Consequently, all filaments exhibit different bond properties within a single carbon yarn. As previously mentioned, the filaments can be grouped into two parts, i.e. the outer part and the inner part. Fig. 3.3 shows an SEM (Scanning Electronic Microscope) image and the idealized cross-section of an embedded carbon yarn. The filaments in the outer part show a strong bond adhesion with the matrix, while there is no contact between filaments and the matrix for the inner part. When the carbon yarn is stressed, the tensile stress is higher in the outer part than the inner part. Besides, two types of interfaces can be introduced, i.e. the outer interface and the inner interface.

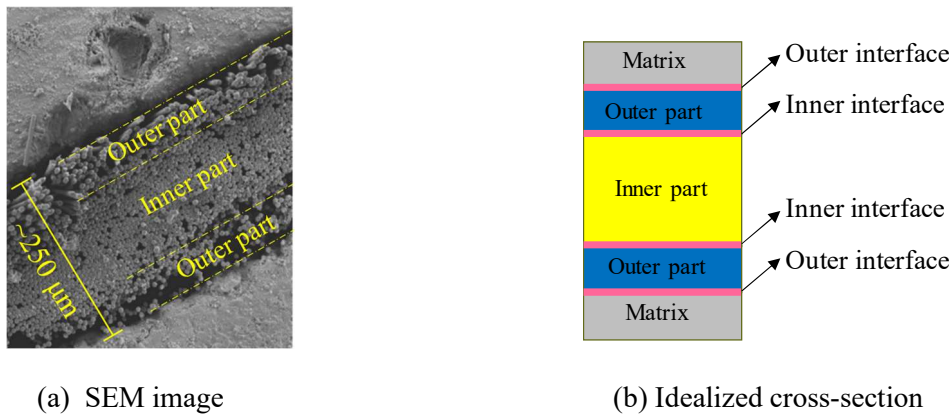


Fig. 3.3. SEM image (a) and the idealized cross-section (b) of an embedded carbon yarn

The failure observed in the pullout tests with a 30 mm embedded length was presented in Fig. 3.4. It can be seen that all the pullout specimens showed a similar failure mode that is the slippage of the carbon yarn through the matrix at first sight. Nevertheless, an apparent difference can be found by performing a close inspection in the failure mode for specimens with different embedded lengths. A schematic illustration of different failure modes was given in Fig. 3.5, including pure slippage of the carbon yarn and slippage-partial rupture of the carbon yarn. The specimens with a 30 mm embedment length failed by pure slippage of the carbon yarn through the matrix. As for the longer lengths (50 mm and 70 mm), the failure was changed to slippage-partial rupture of the carbon yarn that is a combination of slippage of the inner part and tensile rupture of the outer part.

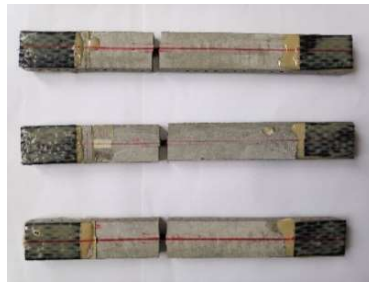
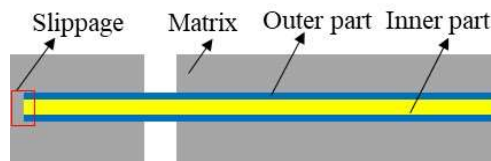
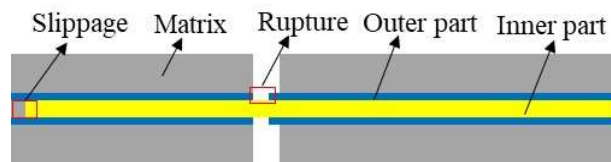


Fig. 3.4. Failure mode observed in pullout tests with 30 mm embedded length



(a) Pure slippage



(b) Slippage and partial rupture

Fig. 3.5. Schematic illustration of different failure modes in pullout tests, (a) pure slippage of the carbon yarn and (b) slippage and partial rupture of the carbon yarn

Fig. 3.6 plots the applied force versus pullout displacement curves (hereafter called pullout curves or  $P-u$  curves) obtained from pullout tests. As can be seen, all the specimens showed a similar pullout behavior characterized by an ascending portion up to the peak and a post-peak softening behavior followed by a slowly descending portion. The slope of the ascending portion is similar for all specimens with different embedment lengths, as it is mainly related to the bond activated on the outer interface. However, although the post-peak softening behavior and the horizontal portion are similar for various embedment lengths, the underlying mechanisms are quite different.

For 30 mm long embedded length, the reduction in the applied force after the peak is related to the degradation in the bond of the outer interface. Whilst it is because of the progressive rupture

of filaments in the outer part of the carbon yarn for longer embedded lengths (50 mm and 70 mm). As for the slowly descending portion, it is attributed to the friction at the outer interface for 30 mm embedded length, while for the longer embedded lengths it becomes the friction at the inner interface after breakage of the outer part. Besides, the peak force rises with increasing embedded length. The peak force increases rapidly for embedded length increasing from 30 mm to 50 mm, while less for a further increment in embedded length. When pullout specimens failed by the slippage of the whole carbon yarn, the peak pullout force is related to the bond behavior of the outer interface and increases significantly with increasing embedded length. As for specimens exhibited the slippage of the carbon yarn with partial rupture, the peak pullout force is related to the tensile capacity of the outer part and the force transferred through the inner interface. The force transferred is less effective through the inner interface than the outer interface, and thus the peak force increases at a decreasing rate for a further increment in the embedded length.

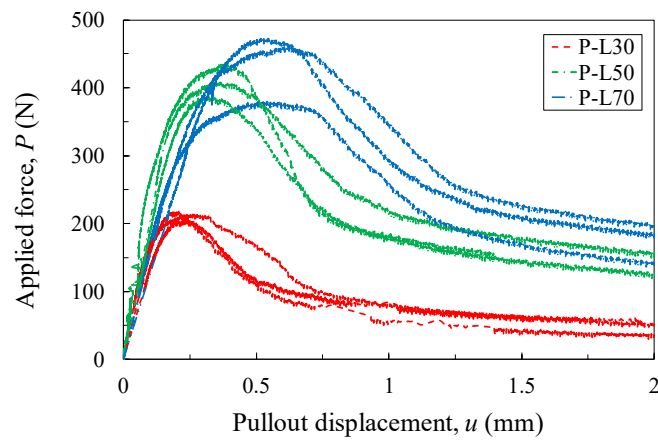


Fig. 3.6. The applied force vs. pullout displacement curves obtained from pullout tests

### 3.3 Discussion

#### 3.3.1 Estimation of the cross-sectional area of the outer part

As previously described, filaments within a single yarn can be grouped into the outer and inner parts due to limited impregnation of the matrix. A problem arises on how to estimate the percentage of the outer part within a single embedded carbon yarn, which means how much percentage is the impregnated filaments compared to the total number of the filaments. The percentage is also termed the degree of matrix impregnation. According to the SEM image shown in Fig. 3.3, it is hard to accurately differentiate the filaments between the outer and inner parts. An approach was proposed to estimate the degree of matrix impregnation by analyzing the number of the filaments remained in the matrix after pullout tests with long embedded lengths, which was equal to the total number of filaments subtracted by the number of the pullout filaments after tests.

In pullout tests, the carbon yarn was pulled through the matrix and then coated with epoxy resin. Samples were prepared by cutting the impregnated carbon yarn into pieces at the free end that is close to the upper cut in the pullout specimens. To analyze variations in the number of the pullout filaments along the embedded length, the carbon yarn collected from one pullout test with an embedded length of 70 mm was processed, and two samples were collected at the free

end and the loaded end of the embedded length. The cross-section of the samples was carefully ground and polished in order to remove the possible scratches and acquire images with high quality. Then, the samples were observed under an optical microscope, and the cross-sectional images can be acquired. As the viewing field of the microscope is limited, the cross-section of each sample should be subdivided into several areas. Afterwards, image processing and analysis were carried out with the NIT ImageJ software to analyze the number of filaments pulled out of the matrix. Fig. 3.7 illustrates the image processing procedure involving original image, contrast enhancement, binarization and counting. As can be seen in Fig. 3.7(d), black spots represent the filaments, of which the number can be analyzed.

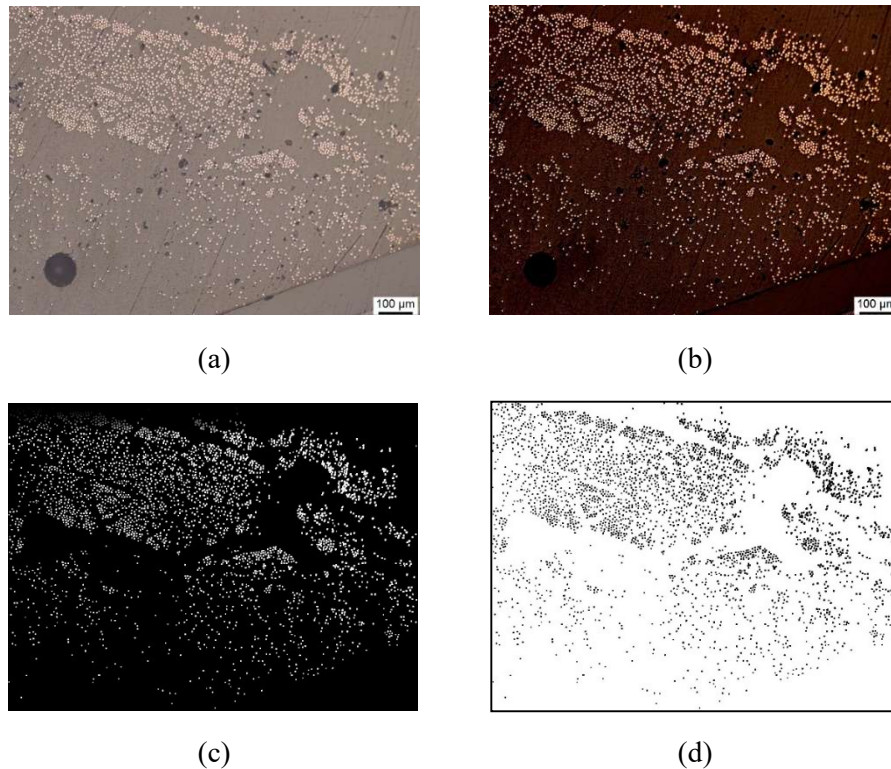


Fig. 3.7. Image processing procedure involving (a) original image, (b) contrast enhancement, (c) binarization and (d) counting

Fig. 3.8 shows the number of pullout filaments for different embedment lengths and the different locations within one embedded carbon yarn. For comparison purposes, the theoretical number of filaments in as-received carbon yarns that equals 12000 is also plotted in Fig. 3.8. For specimens with a 30 mm embedded length, the number of pullout filaments is close to that of the as-received yarn, indicating almost all the filaments were pulled out of the matrix after pullout tests. As for longer embedded lengths, the number of pullout filaments is almost equal, which means the equal number of filaments left in the matrix due to the partial rupture of the carbon yarn. No significant difference is found in the number of pullout filaments at different locations according to Fig. 3.8(b). The image processing and analysis result is consistent with the observed failure modes in the pullout tests. As the remained filaments in the matrix reflect the strong bond between the filaments and matrix, these filaments belong to the outer part within the embedded carbon yarn. The number of remained filaments is equal for embedded lengths of 50 mm and 70 mm, which means the number of filaments subjected to tensile failure equals



50 mm and 70 mm embedded lengths, and thus this number can be used to indicate the number of filaments within the outer part. Based on the result obtained from image analysis, the number of filaments in the outer part can be estimated at around 3600, which accounts for 30% of the total number of the filaments within the carbon yarn. In other words, the degree of matrix impregnation is about 30% for the carbon yarn embedded in the cementitious matrix.

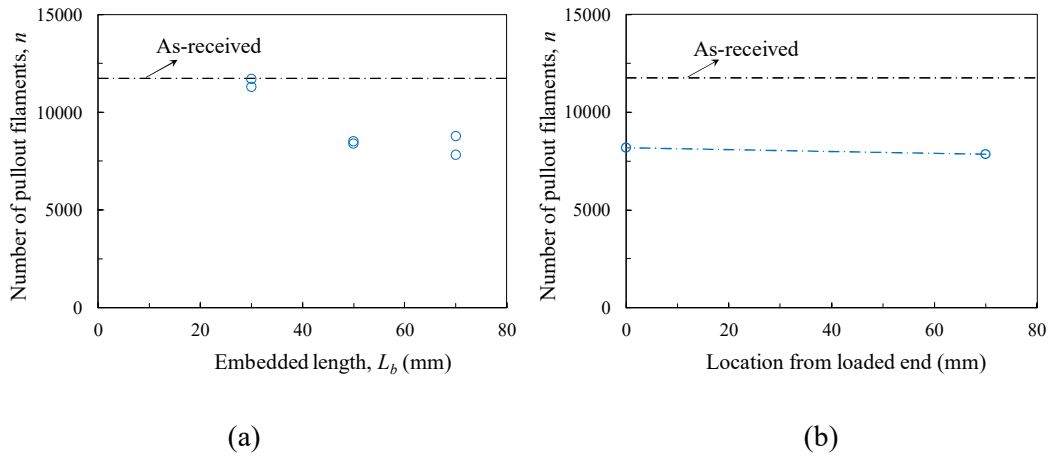


Fig. 3.8. The number of pullout filaments for different embedded lengths (a) and different locations within one carbon yarn.

### 3.3.2 Evaluation of bond slip relationships for the outer and inner interfaces

#### 3.3.2.1 Description of the interfacial issue in the carbon fabric-cementitious matrix system

As each carbon yarn in the fabric has many filaments, accurate modeling of the pullout behavior of the whole carbon yarn in the matrix should take into account the bond behavior of each filament and the interaction between different filaments. It may cause much computational effort and become extremely difficult in practical use, such as modeling the mechanical behavior of FRCM composite strengthening systems. Besides, to accurately determine the bond behavior of each filament remains a challenging task. Since the difference in the bond behavior of the filaments is mainly associated with matrix impregnation, an embedded carbon yarn can be at least subdivided into two parts. According to the idealized cross-section of the embedded carbon yarn as shown in Fig. 3.3(b), the carbon yarn was simplified as the outer and inner parts, and two types of interfaces were introduced. With this simplification, the computational effort in modeling the overall pullout behavior of the whole yarn can be reduced, while the bond behavior complicated by the matrix impregnation can be captured. Furthermore, it is also more practical to evaluate the bond behavior of different parts within the yarn rather than all the filaments.

As shown in Fig. 3.3(b), the inner part is located in the core of the cross-section of the carbon yarn and connected to the outer parts through the inner interface, while the outer parts encompass the inner part and are connected to the matrix through the outer interface. The cross-section of the embedded carbon yarn is assumed as a rectangular shape. The cross-sectional area of the outer part and the inner part can be estimated based on the image analysis results. Fig. 3.9 shows a diagram of the force equilibrium for a small segment  $dx$  of an embedded carbon yarn in the matrix.



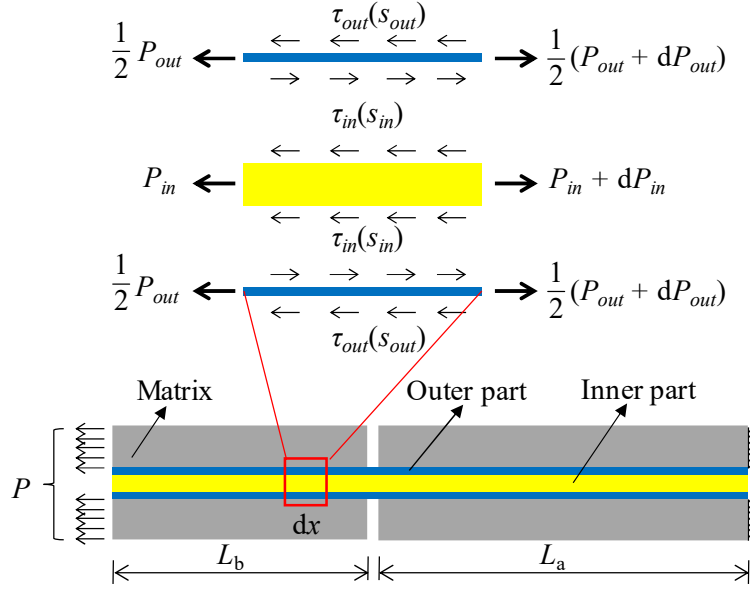


Fig. 3.9. Diagram of the force equilibrium for a small segment  $dx$  of an embedded carbon yarn

As there are two types of interfaces, the bond behavior of the embedded carbon yarn can be represented by a set of two interfacial governing equations. According to Fig. 3.9, this set of equations can be established as,

$$\frac{dP_{out}}{dx} = 2(\tau_{out} - \tau_{in})c \quad (3.1a)$$

$$\frac{dP_{in}}{dx} = 2\tau_{in}c \quad (3.1b)$$

where  $P_{out}$  and  $P_{in}$  represent the tensile force carried by the outer part and the inner part, respectively;  $\tau_{out}$  and  $\tau_{in}$  denote the shear stress at the outer interface and the inner interface, respectively; and  $c$  is the carbon yarn's width.

By substituting the linear tensile behavior of the carbon yarn and geometric equations, Eq. (3.1) can be changed to,

$$\frac{d^2 s_{out}}{dx^2} - \frac{2(\tau_{out} - \tau_{in})c}{EA_{out}} = 0 \quad (3.2a)$$

$$\frac{d^2 s_{in}}{dx^2} - \frac{2\tau_{in}c}{EA_{in}} = 0 \quad (3.2b)$$

Where  $s_{out}$  is the slip of the outer part relative to the matrix and  $s_{in}$  is the slip of the inner part relative to the outer part;  $E$  represents Young's modulus of the carbon yarn; and  $A_{out}$  and  $A_{in}$  are the cross-sectional area of the outer part and the inner part, respectively.

As can be seen in Fig. 3.9, the boundary conditions can be represented by the strain at the free and loaded end of the carbon yarn. The strain of the carbon yarn at the free end is identically equal to zero for the embedded and anchorage length, whilst the pullout displacement is the sum of the loaded end slip for the embedded and anchorage length.

In order to solve the interfacial governing equations, bond slip relationships of the outer and inner interfaces are required. When determining the bond slip relationship, different bond mechanisms should be considered for different interfaces. The filaments in the outer part are stressed due to the adhesion at the interface between the filaments and matrix. The outer interface herein defined is similar to the interface between carbon yarn and matrix which has been discussed in Chapter 2. According to the previous study (Zhu et al. 2018), a trilinear bond slip relationship can be used to represent the interface between the carbon yarn and matrix. Fig. 3.10(a) shows the trilinear bond slip relationship for the outer interface, including ascending, descending and constant branches. These three branches, respectively, indicate the elastic, debonding and friction state.

As for the filaments in the inner part, the bond is due to the presence of friction among them. It is commonly known that friction is the force that resists the relative sliding of two objects in contact. The static friction occurs when these objects are kept stationary, and the dynamic friction develops if one object is sliding over another object. The static friction force is marginally higher than the dynamic friction force. Considering the presence of friction, constant bond stress can be assumed for the bond slip relationship of the inner interface. During the pullout process, however, the inner part becomes more compact due to the Poisson effect of carbon filaments and the contraction of free space between the filaments, and the exiting pressure normal to the inner interface is reduced. Thus, the bond slip relationship featured by a descending behavior, as shown in Fig. 3.10(b) can be assumed for the inner interface.

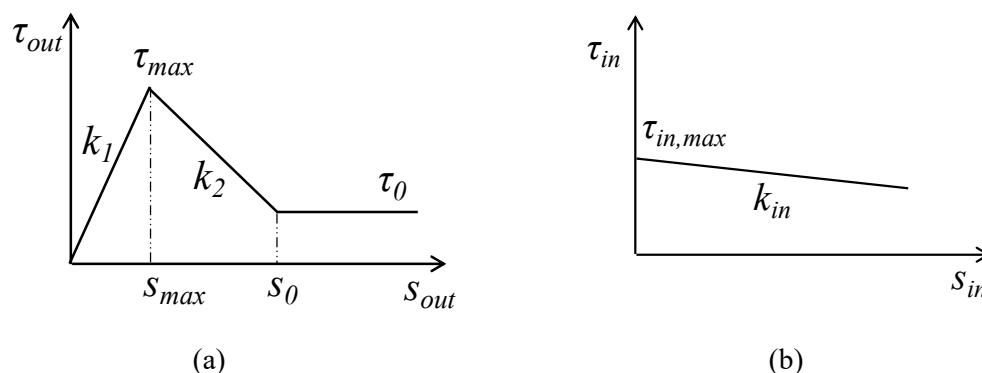


Fig. 3.10. Bond slip relationship for the outer interface (a) and the inner interface (b)

### 3.3.2.2 Evaluation of the bond parameters for the outer interface

After choosing different bond slip relationships for different interfaces, a problem becomes how to determine the bond parameters required to define the bond slip relationships. For a small embedded length (30 mm), specimens failed because of pure slippage of the whole carbon yarn, indicating the overall pullout behavior was controlled by the bond at the outer interface. Therefore, the test results obtained from pullout tests with 30 mm embedded length can be used to evaluate the bond parameters in the trilinear bond slip relationship for the outer interface. As it is not easy to solve the interfacial problem involving multiple interfaces, the inner

interface was neglected when evaluating the outer interface. Then, the bond behavior of the carbon yarn can be simplified as one governing equation with respect to the outer interface, as expressed by Eq. (3.3).

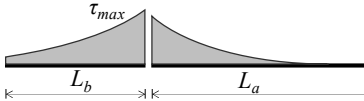
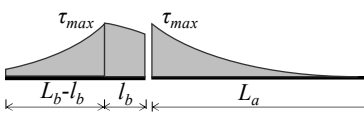
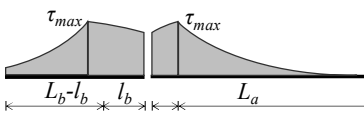
$$\frac{d^2 s_{out}}{dx^2} - \frac{2\tau_{out}c}{EA} = 0 \quad (3.3)$$

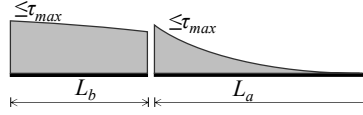
Where  $A$  is the cross-sectional area of the whole carbon yarn.

By introducing the boundary conditions and the trilinear bond slip relationship, Eq. (3.3) can be analytically solved and the overall pullout behavior can be derived.

The trilinear relationship has been used in some studies (Dalalbashi et al. 2018b; Zhang et al. 2013, 2014; Zhu et al. 2018) concerning one-sided pullout tests, and the corresponding overall pullout behavior has been derived based on the possible interfacial bond stress distributions, namely interfacial stress states. Similarly, the closed-form formula of  $P\sim u$  curve can be obtained for the double-sided tests when using the trilinear bond slip relationship, based on the possible interfacial states along the embedded and anchorage lengths. The analytical expressions of the  $P\sim u$  curve for double-sided pullout tests are tabulated in Table 3.1.

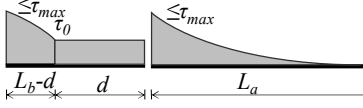
Table 3.1 Analytical expressions of  $P\sim u$  curve for double-sided pullout tests

Interfacial stress state	Analytical expressions for $P\sim u$ curve
 <p>(a) Elastic state</p>	$P = EA\lambda \frac{\tanh(\lambda L_a) \tanh(\lambda L_b)}{\tanh(\lambda L_a) + \tanh(\lambda L_b)} u$ $\lambda = \sqrt{\frac{2ck_1}{EA}}$
 <p>(b) Elastic-debonding state (I)</p>	$P = \frac{\omega^2 \lambda EA \tanh(\lambda L_a)}{\lambda \tan(\varphi) \tanh(\lambda L_a) + \omega^2} \left( u - \frac{k_1 + k_2}{k_1 k_2} \tau_{max} \right)$ $\omega = \sqrt{\frac{2ck_2}{EA}}$ $\varphi = \omega l_b - \arctan\left(\frac{\lambda}{\omega \tanh(\lambda L_b - \lambda l_b)}\right)$
 <p>(c) Elastic-debonding state (II)</p>	$P = \frac{\omega EA}{\tan(\varphi) + \tan(\varphi_a)} \left( u - 2 \frac{k_1 + k_2}{k_1 k_2} \tau_{max} \right)$ $\varphi_a = \omega l_a - \arctan\left(\frac{\lambda}{\omega \tanh(\lambda L_a - \lambda l_a)}\right)$



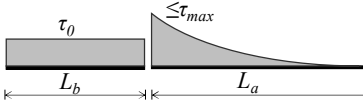
(d) Debonding state

$$P = \frac{EA\lambda\omega \tanh(\lambda L_a) \tan(\lambda L_b)}{\omega \tan(\lambda L_b) - \lambda \tanh(\lambda L_a)} \left( u - \frac{k_1 + k_2}{k_1 k_2} \tau_{max} \right)$$



(e) Friction-debonding state

$$P = \frac{2EA\lambda \tanh(\lambda L_a) (\tan(\omega L_b - \omega d) + \omega d)}{\lambda \omega L_b^2 \tanh(\lambda L_a) + 2 \tan(\omega L_b - \omega d) + 2 \omega d} \left( u - \frac{k_1 + k_2}{k_1 k_2} \tau_{max} \right)$$



(f) Friction state

$$P = \frac{\lambda EA c \tau_0 \tanh(\lambda L_a)}{c \tau_0 - \lambda EA \tanh(\lambda L_a)} (u - L_b)$$

The bond parameters of the trilinear bond slip relationship can be obtained by comparing the above analytical solution to the experimental  $P \sim u$  curve. The evaluated bond parameters of the trilinear bond slip relationship for the outer interface are  $k_1 = 24.96 \text{ N/mm}^3$ ,  $k_2 = 1.55 \text{ N/mm}^3$ ,  $\tau_{max} = 1.38 \text{ MPa}$  and  $\tau_0 = 0.23 \text{ MPa}$ , respectively.

### 3.3.2.3 Evaluation of the bond parameter for the inner interface

Two bond parameters,  $\tau_{in,max}$  and  $k_{in}$  are required to determine the bond slip relationship for the inner interface. As previously described, the pullout specimens with embedded lengths of 50 mm and 70 mm failed by to slippage-partial rupture of the carbon yarn. After the breakage of the outer part, the pullout behavior was controlled by the inner interface. Thus, the experimental results of these specimens were used to evaluate the bond parameters for the inner interface.

The interfacial governing equation for the inner interface can be expressed by Eq. (3.2b). With inserting the bond slip relationship of the inner interface, the relationship between the pullout force and the slip at the loaded end for the anchorage and embedded length can be derived respectively. As the anchorage length is much longer than the embedded length, the slip and the strain at the free end of the anchorage can be assumed to be null, the corresponding relationship between the pullout force and the slip at the loaded end can be derived as Eq. (3.4). Such derivation is similar to that described in Appendix A, which is further extended to be a generalized method of evaluating the bond behavior between FRP and concrete.

$$P = 2 \sqrt{EA_{in} c \left( \tau_{in,max} u_a - 0.5 k_{in} u_a^2 \right)} \quad (3.4)$$

where  $u_a$  is the loaded end slip of the anchorage length of the inner part.

In the case of the embedded length, the free end strain of the inner part is always zero, while non-zero slip may occur. The relationship between the pullout force and the slip at the loaded end of the embedded length can be expressed by Eq. (3.5),

$$P = EA_{in} \lambda_{in} \tan(\lambda_{in} L_b) \left( \frac{\tau_{in,max}}{k_{in}} - u_b \right) \quad (3.5)$$

$$\lambda_{in} = \sqrt{\frac{2ck_{in}}{EA_{in}}} \quad (3.5a)$$

Where  $u_b$  is the slip at the loaded end of the embedded length of the inner part.

The pullout displacement after breakage of the outer part can be treated as the sum of  $u_a$  and  $u_b$ . Combining Eq. (3.4) with Eq. (3.5), the  $P-u$  curve after the breakage of the outer part can be established and then compared with the experimental results in order to obtain the bond parameters for the inner interface. Based on the test result obtained with 50 mm and 70 mm embedded length, the obtained bond parameters for the inner interface are  $k_{in} = 0.12 \text{ N/mm}^3$  and  $\tau_{in,max} = 0.60 \text{ MPa}$ , respectively.

### 3.3.3 Numerical modeling of pullout tests

#### 3.3.3.1 Finite element model

In order to reproduce the pullout behavior of carbon fabric in the cementitious matrix and verify the accuracy of the bond slip relationships evaluated for the outer and inner interfaces, a nonlinear finite element (FE) analysis was carried out with a commercial Diana 10.3 package. The numerical modeling results were then compared to the experimental results obtained from pullout tests.

FE models of pullout specimens were created using the principle of symmetry. The model included exclusively the examined middle carbon yarn connecting the bond block with the anchoring block, while the other longitudinal and transverse carbon yarns were neglected. The examined carbon yarn was divided into two subparts, the outer part and inner part, where the respective cross-sectional area can be obtained from the image processing and analysis. The inner part was connected to the outer part through the inner interface, while the outer part to the matrix through the outer interface. The outer and inner interfaces were modeling using zero-thickness interface elements. Besides, a zero-thickness layer of interface elements was defined between the matrix at the opening of pullout specimens in order to connect the bond and anchorage blocks. The numerical model had the embedded and anchorage lengths which equal those of the pullout specimens. Based on the adopted test setup, the clamped side of the anchoring block was fixed in two perpendicular directions. A displacement-controlled analysis was carried out by applying the prescribed displacement to the end of the matrix of the bond block.

The plane stress hypothesis was applied assuming that the stress condition across the specimen width is uniform. Four-node quadratic plane stress elements were used to model the cementitious matrix and the outer and inner parts of the carbon yarn. The material behavior of the matrix in tension was assumed linearly elastic, as the tensile stress in the matrix was under the tensile strength and no tensile cracks occurred. As can be seen from tensile tests performed on the plain carbon yarns, these yarns show a linearly elastic behavior until the brittle failure featured by a full reduction in tensile stress after the ultimate tensile strength. However, while the carbon yarn is embedded in the matrix, non-uniform distribution in the tensile stress can be developed, as filaments within the yarn show various bond characteristics. Consequently, the filaments would fail progressively due to the non-uniform distribution of the tensile stress, as shown in Fig. 3.11(a). The filaments that would fail can be grouped in the outer part of the

carbon yarn according to the image analysis result. The tensile strength of the embedded carbon yarn should be lower than that of the plain carbon yarn, as the progressive failure cannot mobilize all filaments of the yarn simultaneously. The effective tensile strength ratio,  $\beta_t$ , was defined as the ratio of the tensile strength between the embedded carbon yarn and the plain yarn. The tensile strength of the embedded carbon yarn can be estimated by the difference between the peak pullout force and the residual force after progressive failure. Based on the test results with 50 mm and 70 mm embedded length, the value of 0.7 for  $\beta_t$  is suggested. To represent the progressive failure, a tension softening behavior can be defined for the embedded carbon yarn, in which the post-peak tensile stress declines gradually, as shown in Fig. 3.11(b). Such a softening behavior can also be assumed for the fiber reinforced polymer that exhibits progressive failure (Park et al. 2016; Xue et al. 2015). As can be seen in Fig. 3.11(b), the tension softening behavior can be described by the fracture energy  $G_f$  that is defined as the area under the softening part of the stress-strain curve. Different fracture energies in the range of 0 to 1000 N/mm were used in FE modeling in order to investigate the effects on the pullout behavior. When  $G_f$  is zero, the carbon yarn is reduced to be a pure brittle material.

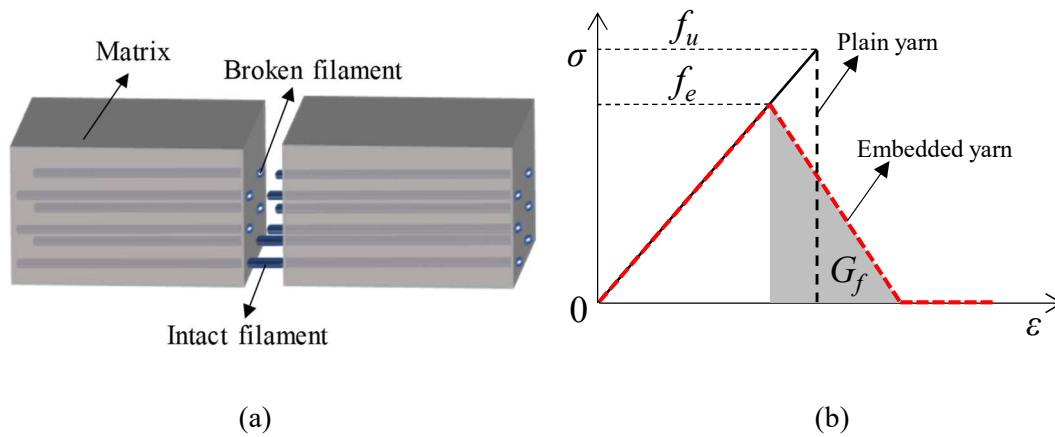


Fig. 3.11 Schematic illustration of (a) progressive failure of the filaments in the outer part and (b) tensile behavior of the outer part

In addition to the matrix and carbon yarn, the material behavior should be defined for different interfaces involved. The interfacial discrete cracking law with null tensile strength was defined at the interface elements connecting the bond and anchoring blocks. Another two sets of interface elements were employed to model the interfacial bond at the outer and inner interfaces, respectively. The evaluated bond slip relationships were assigned to these interface elements.

### 3.3.3.2 Comparison between experimental and numerical results

Numerical results obtained from FE modeling were then compared with the experimental results. Fig. 3.12 compares the  $P$ - $u$  curves obtained from experiments and FE modeling for specimens with 30 mm embedded length. As for 30 mm embedded length, specimens exhibit a failure mode characterized by the slippage of the carbon yarn, and thus the maximum pullout force is due to the transferred force that the outer interface can bear. Hence, the pullout behavior of the specimens is governed by the bond behavior of the outer interface. Since there is no tensile failure observed for all filaments within the embedded carbon yarn, the pullout behavior would not be affected by the fracture energy defined for the yarn. As can be seen in Fig. 2.12,

a good agreement can be achieved between experimental and numerical results, suggesting that the evaluated bond slip relationship for the outer interface is appropriate.

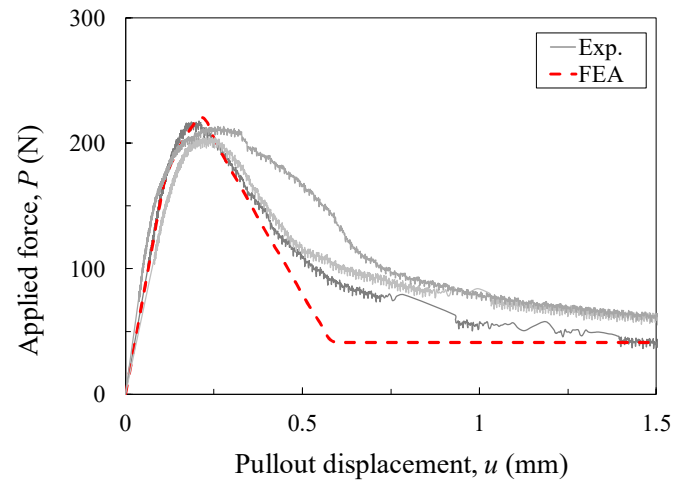


Fig. 3.12 Comparison of the  $P\sim u$  curve obtained from experiments and FE modeling for pullout specimens with 30 mm embedded length

As for longer embedded lengths ( $\geq 50$  mm), the specimens show a similar failure mode that is slippage-partial rupture of the embedded carbon yarn. The fracture energy of the carbon yarn can influence the pullout behavior, which is analyzed by comparing experimental with numerical results for different fracture energies. Fig. 3.13 compares the  $P\sim u$  curves obtained from experiments and FE modeling for specimens with 70 mm embedded length. Various values of  $G_f$  in defining the tensile softening behavior of carbon fabric were considered, which was indicated by the figure in the legend of Fig. 3.13. There are some discrepancies in the post-peak behavior of simulated  $P\sim u$  curves. The discrepancies were caused by the different fracture energies used in the FE modeling. Once the tensile strength is reached for filaments in the outer part of the carbon yarn, these filaments start to fail in a progressive manner. If  $G_f$  is higher, the tensile stress descends more slowly, which means the progressive failure phenomenon is more pronounced. Therefore, the simulated  $P\sim u$  curve shows a milder descending behavior after the peak for higher fracture energy. The fracture energy mainly affects the post-peak descending branch of the  $P\sim u$  curve, while the pre-peak ascending branch and the last slowly descending branch are not affected as they are dependent on the interfacial behavior of the outer and inner interfaces, respectively. It is clear that the fracture energy of 600 N/mm for the embedded carbon yarn can provide the best simulation of the whole experimental  $P\sim u$  curves. Except for the post-peak descending branch of the simulated curves, the reasonable agreement can be seen between experimental and numerical results, indicating the accuracy of the evaluated bond slip relationships for outer and inner interfaces.

Variations in tensile force carried in the outer and inner parts during the pullout process were analyzed based on FE modeling results. As  $G_f$  mainly affects the post-peak descending branch of the  $P\sim u$  curve, the numerical results that best approximate the experimental results were chosen, i.e. the numerical results with  $G_f = 600$  N/mm. Simulated variations in tensile force at the loaded end of the outer and inner parts of the carbon yarn with 70 mm embedded length and with  $G_f = 600$  N/mm are plotted in Fig. 3.14. The tensile force of the outer part is equal to the difference in the forces transferred through the outer and inner interface, while the tensile force

of the inner part equals the force transferred solely through the inner interface. As for small pullout displacements, the tensile force at the loaded end of the inner part is higher than that of the outer part. According to the defined material behavior of the inner interface, the maximum bond stress can be reached once the non-zero slip occurs. Hence, the force transferred from the outer interface can be effectively transferred to the inner interface. When the maximum force that the inner interface can bear is reached, the force carried by the inner part is reduced. With increasing pullout displacement, the tensile force of the outer part becomes higher until the tensile capacity is reached. Afterwards, progressive failure appears for the outer part, and thus the tensile force of the outer part experiences a gradual reduction. After the tensile failure of the outer part, the pullout behavior of the specimen is controlled by the inner interface, indicating by the superposition of the  $P\sim u$  curve of the whole carbon yarn and the inner part.

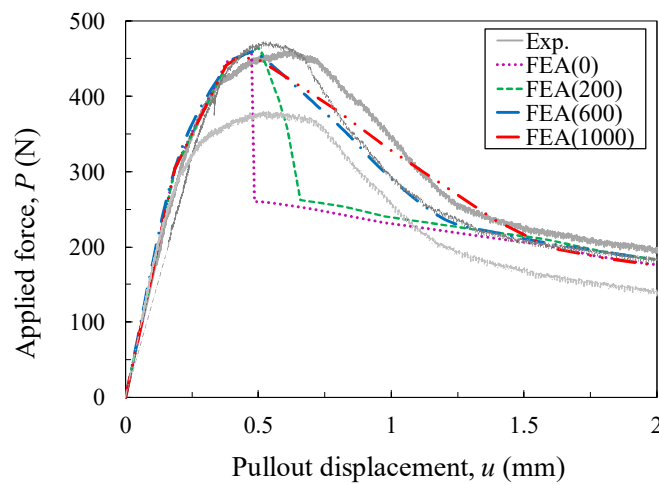


Fig. 3.13 Comparison of the  $P\sim u$  curve obtained from experiments and FE modeling for pullout specimens with 70 mm embedded length

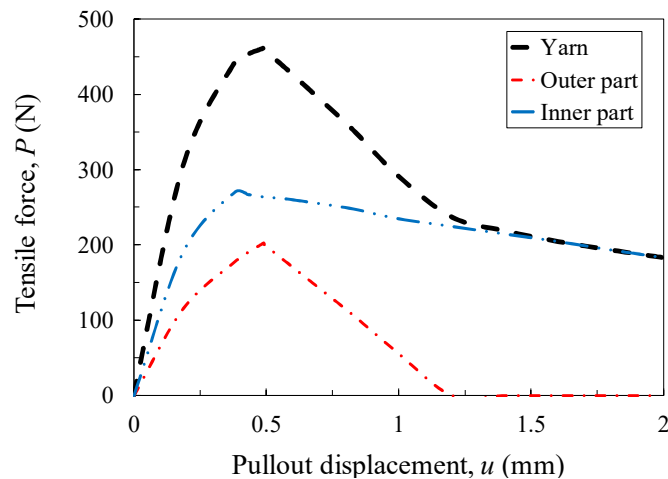
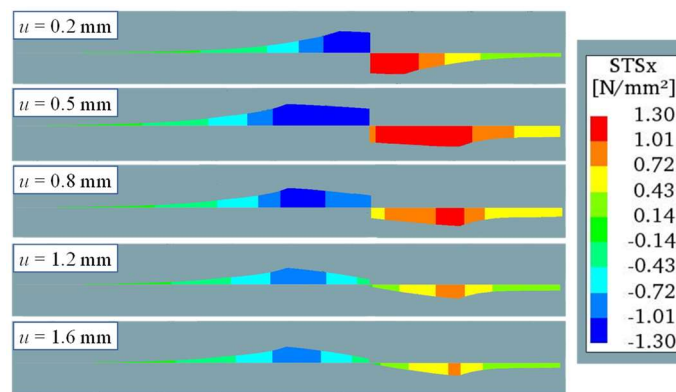


Fig. 3.14 Simulated variations in tensile force at the loaded end of the outer and inner parts of the carbon yarn with  $G_f = 600$  N/mm

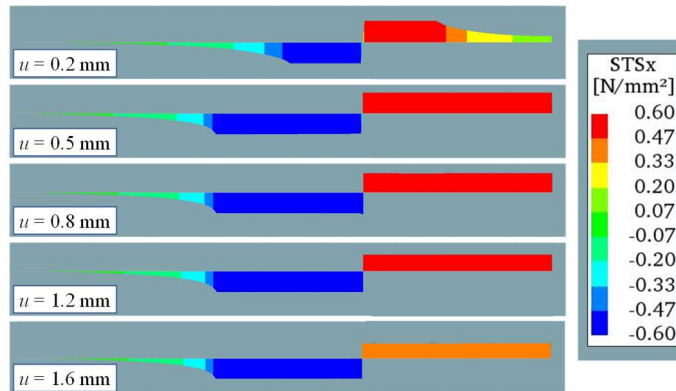
Fig. 3.15 shows the simulated bond stress distribution at the outer and inner interface for pullout specimens with 70 mm embedded length and with  $G_f = 600$  N/. For the outer interface,



debonding initiates at the loaded end and propagates towards the free end for the anchorage and embedded length of the carbon yarn. As the anchorage length is sufficiently long, the bond stress at the free end is equal to zero due to the null slip, and two interface stress states (elastic and elastic-debonding states) appear during the pullout process of the carbon yarn. While for the embedded length, the multiple interface stress states can be developed with increasing pullout displacement, including the elastic, elastic-debonding, debonding, debonding-friction and friction states. The maximum pullout force is reached when the outer interface on the embedded length side is in the debonding state. As for the inner interface, the maximum bond stress occurs first at the loaded end of the embedded length and shifts to the free end. A quasi-uniform bond stress distribution is developed along the inner interface on the embedded length side. This is due to the defined material behavior for the inner interface, in which the bond stress descends slightly with increasing the slip after the origin.



(a)



(b)

Fig. 3.15 Simulated bond stress distribution at the outer (a) and inner (b) interfaces of pullout specimens with 70 mm embedded length and with  $G_f = 600$  N/mm

### 3.3.4 Parametric study on effects of key parameters

This section presents a parametric study to provide an understanding on how matrix impregnation, the fabric effective tensile strength and embedded length affect the pullout behavior of the carbon fabric in the cementitious matrix.  $\beta_m$  was used to indicate the degree of matrix impregnation, which equals the percentage of the outer part.  $\beta_m$  can be changed by

modifying the matrix, like adding some small particles. Besides, it is also practical to increase  $\beta_m$  by changing the size of the yarn and the type of filament. For instance,  $\beta_m$  increases with decreasing the yarn thickness. If the carbon yarn is very thin or contains only a few filaments, then a high degree of matrix impregnation can be achieved.

Provided the matrix impregnation is non-uniform across the outer part, there is a non-uniform distribution in the tensile stress within the outer part. Such distribution is simplified as a linear distribution to establish the relationship between  $\beta_t$  and  $\beta_m$ . Fig. 3.16 presents a simplified tensile stress distribution of the carbon yarn corresponding to the point at which the failure of the outer part initiates. The whole area of the yarn is normalized as a unity so that the area of the outer and inner part becomes  $\beta_m$  and  $1-\beta_m$ , respectively. Therefore, Eq. (3.6) can be established according to the definition of  $\beta_t$ .

$$\beta_t = \frac{f_e}{f_u} = \frac{f_u + \sigma_a}{2f_u} = \frac{1}{2} + \frac{\sigma_a}{2f_u} \geq 0.5 \quad (3.6)$$

Where  $\sigma_a$  equals the tensile stress of the filament without matrix impregnation while the peripheral filaments reach the tensile strength. It is obvious that  $\beta_t$  has a minimum value larger than 0.5. Besides,  $\beta_t$  can be taken as 0.7 for  $\beta_m = 0.3$  according to the present study. For a small  $\beta_m$  (close to zero),  $\beta_t = 1.0$  can be suggested.

FE modeling was conducted to gain an understanding of the effects of  $\beta_m$  and  $\beta_t$ .  $\beta_m$  is fixed when analyzing  $\beta_t$ , and vice versa. The effect of  $\beta_m$  on the  $P\sim u$  curve of pullout specimens with an embedded length of 70 mm is presented in Fig. 3.17. There is an increase in the maximum pullout force with increasing  $\beta_m$  from 0.3 to 0.5 and no significant increase for a further increment of  $\beta_m$ . When  $\beta_m$  is larger than 0.5, the failure mode converts from the slippage and partial rupture of the carbon yarn to the slippage of the whole yarn.

The effect of  $\beta_t$  on the  $P\sim u$  curve of pullout specimens with an embedded length of 70 mm is plotted in Fig. 3.18. An increase in  $\beta_t$  results in a rise in the maximum pullout force. The specimen behavior shows a more ductile behavior before the peak force for a larger  $\beta_t$ , though the same failure featured by the slippage and partial rupture of the carbon yarn takes place. This is due to that the  $P\sim u$  curve before the peak is dominated by the outer interface. The higher the transferred force at the outer interface, the more ductile behavior (smaller increase in  $P$  with a larger increase in  $u$ ) is. Higher  $\beta_t$  which means a larger tensile capacity of the outer part allows the force transferred at the outer interface to achieve a higher level and thus the more ductile pullout behavior is caused.

When analyzing the effect of the embedded length, the actual conditions of  $\beta_t$  and  $\beta_m$  were adopted in FE modeling, i.e.  $\beta_t = 0.7$  and  $\beta_m = 0.3$ . The effect of the embedded length on the  $P\sim u$  curves is presented in Fig. 3.19. There is a pronounced increase in the maximum pullout force for the embedded length increasing from 70 mm to 100 mm, while no increase is seen for a further increment of 50 mm in the embedded length. Besides, the ductility of the specimen is improved by increasing the embedded length. Note that for 150 mm long embedded length, the applied force increases up the peak with displacement and then decreases, which is due to the rupture of the outer part; then the force increases again until another peak, which is because after breakage of the outer part, the inner interface can still transfer the force to the inner part.

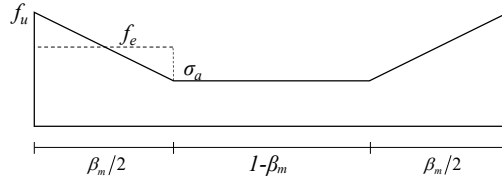


Fig. 3.16 Simplified tensile stress distribution of the carbon yarn at the beginning of breakage of the outer part

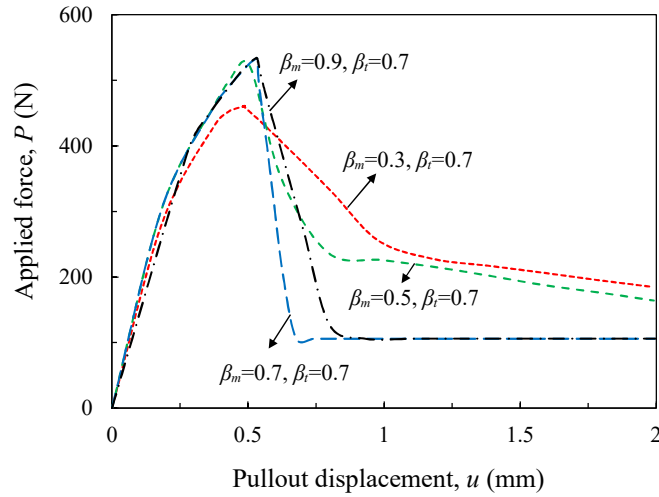


Fig. 3.17 The effect of  $\beta_m$  on  $P\sim u$  curves

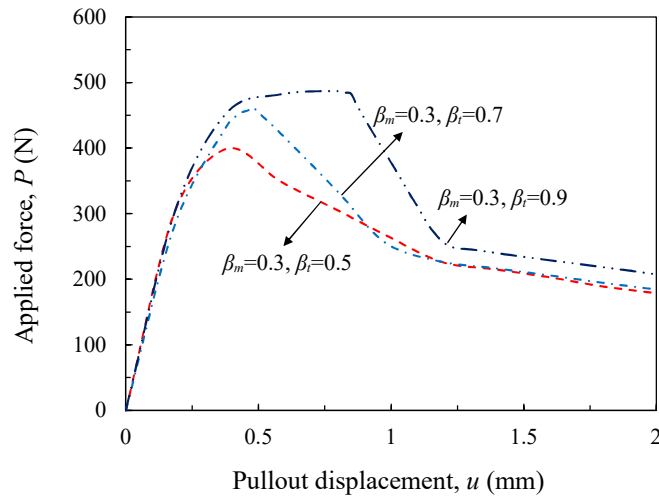


Fig. 3.18 The effect of  $\beta_i$  on  $P\sim u$  curves

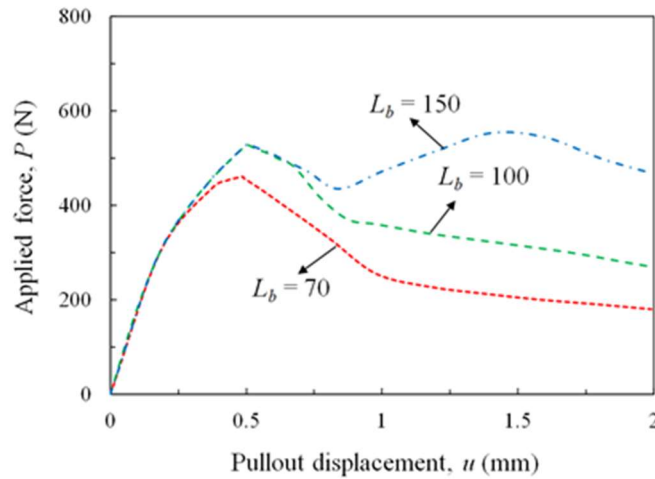


Fig. 3.19 The effect of embedded length on  $P\sim u$  curves

### 3.4 Conclusions of this chapter

Based on the test results and analyses, the following conclusions can be drawn in this chapter.

The pullout specimens exhibited different failure modes that were dependent on the embedded length. As for 30 mm embedded length, all specimens experienced a failure mode featured by the slippage of the whole carbon yarn through the matrix. As for longer embedded lengths ( $\geq 50$  mm), the specimens failed by the slippage-partial rupture of the carbon yarn. The peak pullout force increases rapidly as embedded length increases from 30 mm to 50 mm, and a small increase in the peak pullout force is found for a further increment of the embedded length.

The number of the filaments pulled out of the matrix after pullout tests were evaluated through image processing and analysis. The results show that the number of pullout filament for the specimens with 30 mm embedded length is nearly equal to that of the as-received sample, indicating the slippage of the whole carbon yarn, while for longer embedded lengths, the number of the pullout filaments accounts for 70% of the total number, which means that 30% of filaments are left in the matrix after rupture. The filaments left in the matrix indicate, inversely, the filaments that are impregnated by the matrix. Therefore, the degree of matrix impregnation is equal to 30%.

The embedded carbon yarn can be subdivided into two parts considering the matrix impregnation, including the outer part and inner part. Two types of interfaces were introduced with different bond slip relationships corresponding to different bond mechanisms. A trilinear bond slip relationship was assigned for the outer interface between the outer part and matrix, while a linear descending relationship for the inner interface between the outer and inner parts. These two bond slip relationships were evaluated in an analytical manner using the experimental results obtained from pullout tests. A finite element model incorporating these two interfaces was developed to simulate pullout tests. The results show that the predicted force versus pullout displacement curves agree well with the experimental results, suggesting the accuracy of the bond slip relationships evaluated for the outer and inner interfaces. Besides, the effects of fracture energy on the  $P\sim u$  curve and the contribution of the outer and inner part to carrying the applied force were also discussed based on FE modeling results.

A parametric study was carried out to understand how the degree of matrix impregnation ( $\beta_m$ ) and the strength factor ( $\beta_i$ ) as well as embedded length affect the pullout behavior of the FRCM composites. With increasing  $\beta_m$ , there is an increase in the maximum pullout force until reaching a constant level, accompanying the failure mode changed from the slippage and partial rupture of the carbon yarn to the slippage of the whole yarn. Increasing  $\beta_i$  and embedded length would lead to the increased maximum pullout force and the more ductile pullout behavior.

### Symbols

$A_{in}$ : the cross-sectional area of the inner part within a single carbon yarn;

$A_{out}$ : the cross-sectional area of the outer part within a single carbon yarn;

$c$ : the width of a single carbon yarn;

$E$ : Young's modulus of the carbon yarn obtained from axial tensile test;

$f_u$ : the tensile strength of a plain carbon yarn;

$f_e$ : the effective tensile strength of the outer part;

$G_f$ : the fracture energy required to define the softening behavior of the embedded carbon yarn;

$k_1$ ,  $k_2$ ,  $\tau_{max}$  and  $\tau_0$ : the bond parameters involved in the trilinear BSR for the outer interface, which mean the slope of the first linear part, the absolute value of the slope of the second linear part, the maximum bond stress and residual bond stress;

$k_{in}$ , and  $\tau_{in,max}$ : the bond parameters involved in the BSR for the inner interface, which mean the absolute slope of the descending part and the maximum bond stress;

## Chapter 4

### 4 Mechanisms of degradation of carbon fabric polarized in cementitious matrix

#### 4.1 Introduction

ICCP has been recognized as an effective method of protecting steel in concrete from corrosion (Pedferri 1996; ACI 222R-01 2001; NACE SP0290-2007 2007). The principle of ICCP involves applying protection current to steel in concrete and thus shifting the steel potential negatively to the immunity zone in which steel corrosion can be effectively halted. In ICCP systems, an external anode and the steel are connected to the positive and negative terminals of a power source, respectively. The applied current flows from the anode to the steel through concrete. Hence, the external anode should transfer the electronic current to the ionic current by the anodic reaction in which the hydroxide ions are oxidized to produce oxygen. Thus, the suitable anode should carry with its resistance to tolerate anodic polarization and have a low consumption rate. The development of a suitable anode is always of interest in the area of ICCP for reinforced concrete. Several types of anodes have been investigated and reported in the literature, including organic coating anodes, conductive cementitious overlay anodes and titanium-based anodes (ACI 222R-01 2001; Byrne et al. 2016). The mixed metal oxides coated titanium-based anode is the most widely applied and successful anode in ICCP. Such anode shows the satisfactory capacity of delivering high anodic current density and a very low consumption rate, but the cost is high, which discourages, to some extent, its large-scale application in practical engineering.

Carbon fibers are increasingly attractive for use as an anode in ICCP. Carbon fibers that are utilized in combination with the organic or inorganic matrix are normally used in strengthening concrete structures, such as FRP strengthening (ACI 440.2R 2008) and FRCM strengthening (ACI 549.4R-13 2013). Besides, carbon fibers possess the potential to become an impressed current anode due to their electrical conductivity. Bertolini et al. (2004) (Bertolini et al. 2004) reported a conductive coating overlay consisting of carbon fibers for use in ICCP and found that the overlay worked well for 2 years at a current density up to 20 mA/m<sup>2</sup>. Jing and Wu (Jing and Wu 2011) studied the effects of the content of carbon fibers in the conductive coating overlay for use in ICCP. While using the conductive coating overlay, a primary anode should be used to deliver the anodic current to the overlay. There are available studies regarding the use of carbon fibers as an impressed current anode but not as the conductive component aimed at improving the coating conductivity, see (Chini and Antonsen 2008; Nguyen et al. 2012; Zhang and Tang 2014; Zhu et al. 2014, 2015). Mork et al. (2007) studied a harbor structure that was protected by ICCP with using carbon fiber meshes as an anode and found that the ICCP system can operate in a good condition when the applied current density was in the range of 2~5 mA/m<sup>2</sup> and the voltage was up to 1.8 V. Van Nguyen et al. (2016) utilized carbon fabrics or rods as an impressed current anode for ICCP in solutions and reinforced concrete, along with an aim at improving the ultimate strength of concrete beams. It was also found that the applied current decreased during the application of ICCP, and the reduction was attributed to the dissolution of carbon fibers. Sun and Zhu et al. (Sun et al. 2016a, 2016b; Zhu et al. 2016) examined the tensile behavior and the electrochemical performance of CFRP anodically

polarized in various solutions and concrete. The results show that the relatively stable electrochemical performance can be maintained for CFRP polarized at a current density up to  $6.4 \text{ A/m}^2$  for 50 days, while the CFRP tensile strength decreases with increasing the charge density. It was revealed that the degradation mechanisms differed for CFRP polarized in different electrolytes, and the epoxy resin seems to be more vulnerable during anodic polarization. Zhang (2018) investigated the effect of anodic polarization on the matrix in the vicinity of CFRP mesh anode. The results show that a ring-pattern degradation zone forms around the embedded carbon yarn and the degraded zone enlarges with increasing current density, along with the depletion of calcium indicated by the reduced calcium to silica ratio. Based on the existing studies, carbon fibers have proven to be suitable for use as an anode in ICCP for reinforced concrete, while the choice of operating current density or potential and the possible damage on the matrix and the resin in CFRP should be carefully considered. However, carbon fibers are more likely to degrade when being anodically polarized in the acid or alkaline media, which can be supported in the studies related to the surface treatment of carbon fibers through anodic polarization (Kozłowski and Sherwood 1985; Yumitori and Nakanishi 1996; Bismarck et al. 1999; Liu et al. 2010b; Sun et al. 2019). In the field of anodic surface treatment of carbon fibers, large current densities are normally applied within a short period and thus the chemical composition and morphology of the fibers can be significantly altered. Such studies involved different aqueous electrolytes with an aim at increasing the efficiency of surface treatment. The situation that carbon fibers are polarized in the cementitious matrix can be quite different from the carbon fibers subjected to surface treatment in liquid, such as the porous nature of the cementitious matrix, chemical composition of pore solution and a small current density as well as a longer operating period. Therefore, there is a need to study the polarized caused changes in the chemical composition and morphology of carbon fabric in the cementitious matrix.

The objective of this chapter is to study the electrochemical behavior of carbon fabric for use as an anode in the cementitious matrix and examine the changes in the chemical composition and microstructure of the carbon fabric and matrix to shed light on the mechanisms of degradation of the carbon fabric subjected to anodic polarization. Galvanostatic anodic polarization was applied to MFRCM composites. Various anodic current densities ranged from 0 to  $1000 \text{ mA/m}^2$  and two polarization periods were considered. The electrochemical behavior of MFRCM was regularly monitored in terms of applied current, cell voltage and the instant-off anodic potential during the application of anodic polarization. After completing polarization, a series of characterization techniques were applied to examine the polarization induced changes in the chemical composition and microstructure of carbon fabric and the surrounding matrix.

## **4.2 Experimental program**

### **4.2.1 Materials and specimen preparation**

The raw materials for making MFRCM composites included cement, sand, short carbon fibers and carbon fabric. These raw materials were the same as those used in Chapter 3. The MFRCM composites herein used had a water-cement ratio of 0.35 and a sand-cement ratio of 1.0. Two groups of MFRCM composites were prepared with one group of the composites containing

short carbon fibers in the amount of 0.75 wt% of cement and the other without short carbon fibers. These two groups of MFRCM composites were labeled as M35C and M35, respectively. The same lay-up procedure that was illustrated in Chapter 3 was followed to cast MFRCM composites. Then the composites were covered using plastic wrap immediately after casting and demolded one day later. The composites were then cured for two months in a moist chamber (100% RH) with a temperature of 20 °C. Special care should be taken to protect the protruded carbon fabric from the matrix, which will be treated as connection points to the external circuit.

#### 4.2.2 Application of galvanostatic anodic polarization

Galvanostatic anodic polarization was applied to MFRCM composites. Fig. 4.1 shows the apparatus for applying anodic polarization. As can be seen, a pool was constructed by taking the MFRCM composite as the bottom plate and the surrounding plastic plates as walls. The gap between different plates was sealed with epoxy resin. In addition, the edges of the MFRCM composite were also sealed. Then, a saturated calcium hydroxide solution used as an electrolyte was added into the pool so that the stainless-steel plate can be fully immersed. The protruded carbon fabric and stainless steel were connected to the positive and negative poles of the constant current supplier, respectively. The applied current flowed from the carbon fabric to the steel via the matrix and the electrolyte. Different anodic current densities ranged from 0 to 1000 mA/m<sup>2</sup> and polarization periods of 45 and 90 days were considered. The anodic current density was calculated by the applied current divided by the contact area between carbon fabric and cementitious matrix. The percentage of the surface area of carbon fabric per m<sup>2</sup> is estimated at around 0.54 using an image process and analysis technique. During polarization, the applied current, cell voltage and instant-off anodic potential were regularly measured and recorded with a multi-channel data logger. The method stipulated in NACE SP0290-2007 for measuring the instant-off potential was followed. When measuring the instant-off potential, CSE (saturated copper/copper sulfate electrode) was used as a reference electrode.

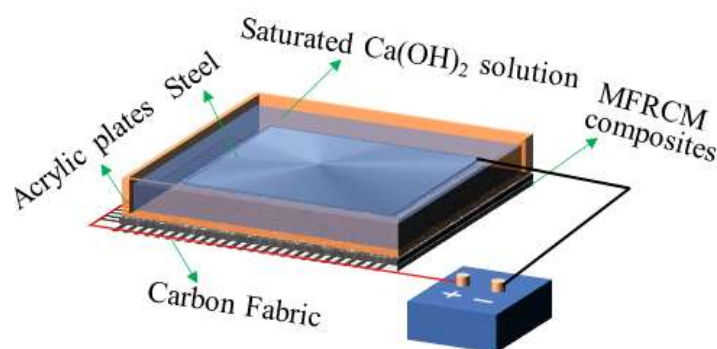


Fig. 4.1 Apparatus for anodic polarization of MFRCM composites

Test parameters for MFRCM composites under anodic polarization are given in Table 4.1. A total of 24 situations were considered in the present study. For illustration, the MFRCM composites were labeled according to the matrix type (M35 and M35C), polarization period  $t$  (45 and 90 days) and anodic current density  $i$  (0-1000 mA/m<sup>2</sup>). For instance, M35-T45-i125 means the MFRCM composite is made of matrix M35 without short carbon fibers and anodically polarized with  $t = 45$  days and  $i = 125$  mA/m<sup>2</sup>. The composites without anodic polarization were considered as the reference composites, namely M35-Ref and M35C-Ref.



Table 4.1 Test parameters for MFRCM composites without and with anodic polarization

No	Specimen	w/c	Short carbon fibers	$i$ (mA/m <sup>2</sup> )	$t$ (day)
1	M35-Ref			0	45
2	M35-T45-i125			20	45
3	M35-T45-i125			60	45
4	M35-T45-i125			125	45
5	M35-T45-i250			250	45
6	M35-T45-i500	0.35	No	500	45
7	M35-T45-i750			750	45
8	M35-T45-i1000			1000	45
9	M35-T90-i20			20	90
10	M35-T90-i60			60	90
11	M35-T90-i125			125	90
12	M35-T90-i250			250	90
13	M35C-Ref			0	45
14	M35C-T45-i125			20	45
15	M35C-T45-i125			60	45
16	M35C-T45-i125			125	45
17	M35C-T45-i250			250	45
18	M35C-T45-i500	0.35	Yes	500	45
19	M35C-T45-i750			750	45
20	M35C-T45-i1000			1000	45
21	M35C-T90-i20			20	90
22	M35C-T90-i60			60	90
23	M35C-T90-i125			125	90
24	M35C-T90-i250			250	90

#### 4.2.3 Material characterization for MFRCM composites

The purpose of characterization is to examine the polarization caused changes in the carbon fabric and matrix within MFRCM composites after anodic polarization. After finishing anodic polarization, samples obtained from MFRCM composites were prepared and examined using a series of characterization techniques, including SEM (scanning electron microscope), EDS (energy dispersive X-ray analysis), FTIR (Fourier Transform Infrared Spectroscopy) and XPS (X-ray photoelectron spectroscopy).

SEM was conducted to observe the morphology of the carbon fabric in the MFRCM composites without and with anodic polarization, while EDS to analyze the elemental composition of the

carbon fabric and matrix. A low-speed precise cutting machine with a sintered diamond saw blade was employed to process MFRCM composites to the samples for SEM and EDS analyses. Alcohol rather than water was used to cool the saw blade during cutting so that the substances to be analyzed will not be dissolved by water. Then, the samples were desiccated and stored in a vacuum drying oven. Before SEM and EDS analysis, golden sputtering was applied to increase the conductivity of the samples. SEM images were obtained under secondary electron mode at an accelerating voltage of 10 V.

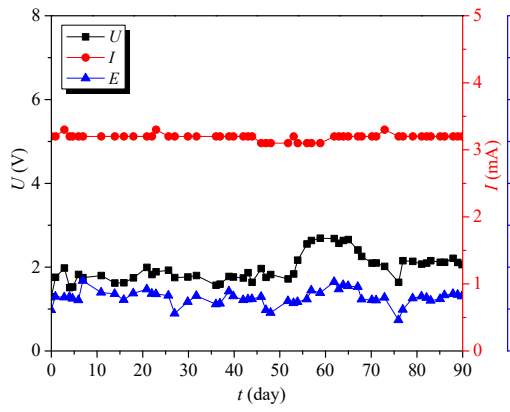
FTIR has proven to be a reliable method to analyze the functional groups on carbon filaments. FTIR spectra were collected using a PerkinElmer FTIR spectrometer (spectrum 100) equipped with an ATR (attenuated total reflection) accessory. The spectra were acquired with operating 64 scans in the range from 600 to 4000  $\text{cm}^{-1}$  with a resolution of 4  $\text{cm}^{-1}$ . The samples for FTIR analysis were extracted from carbon fabric within the MFRCM composites without and with anodic polarization. The extracted carbon fabric was ground to powder and then desiccated in a vacuum drying oven operated at 60 °C prior to FTIR analysis.

X-ray photoelectron spectroscopy (XPS) was employed to quantify the surface functional groups of carbon fabric extracted in the MFRCM composites without and with anodic polarization. XPS was carried out on a ULVAC-PHI 1800 spectrometer with Al  $K\alpha$  X-ray source. The wide scan XPS spectra of carbon fabric were acquired in the range of energy from 0 to 800 eV, while the high-resolution XPS spectra of C 1s were also obtained.

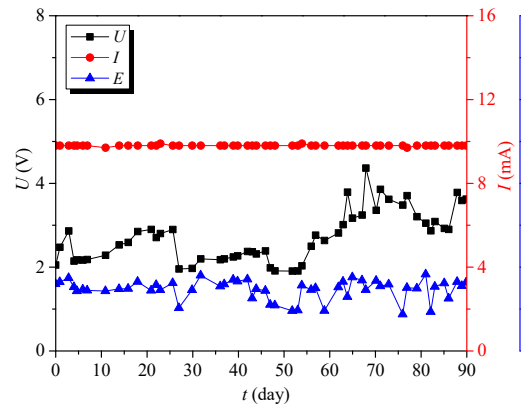
### **4.3 Test results and discussion**

#### **4.3.1 Electrochemical behavior of carbon fabric in cementitious matrix**

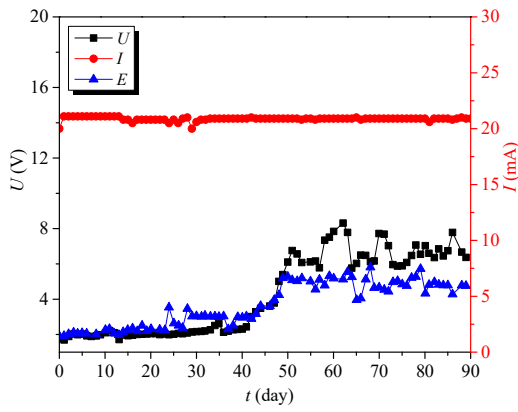
As similar electrochemical performance is shown for MFRCM composites without and with short carbon fibers, only the results from the composites without short carbon fibers are presented. Fig. 4.2 shows measured applied current, cell voltage and instant-off anodic potential for MFRCM composites without short carbon fibers. As for current density no more than 125  $\text{mA/m}^2$ , the constant applied current can be maintained, while the cell voltage and instant-off potential show a slightly increasing trend during polarization. For larger current densities, drastic variations in the applied current and cell voltage can be seen after polarizing the composites for a certain time. Specifically, the applied current experiences a drop, while the cell voltage ascends exponentially. The cell voltage increases and then remains a constant level 60 V due to the limited capacity of the power source.



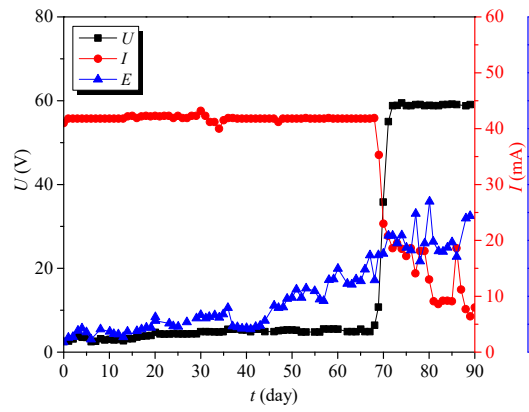
M35-T90-i20



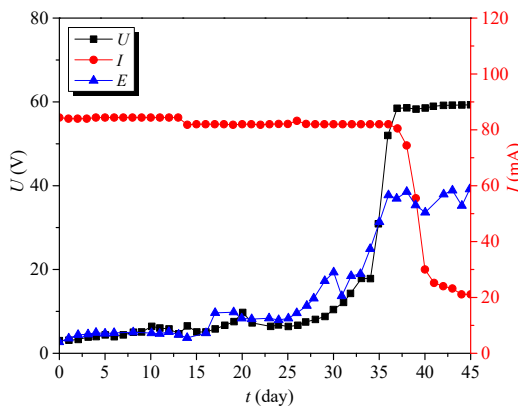
M35-T90-i60



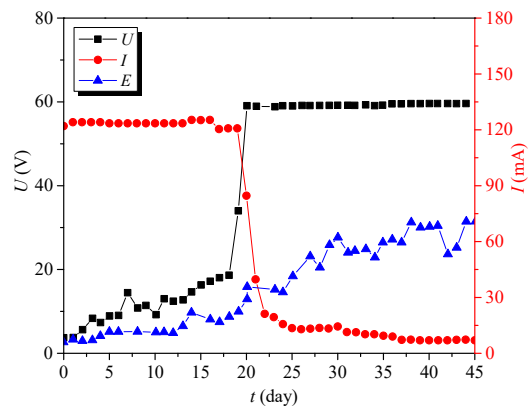
M35-T90-i125



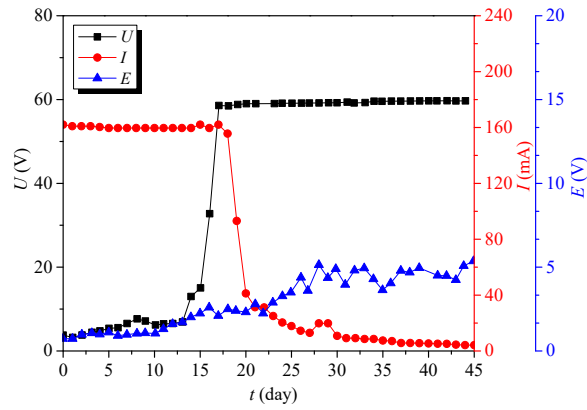
M35-T90-i250



M35-T45-i500



M35-T45-i750



M35-T45-i1000

Fig. 4.2 Cell voltage, current and potential of MFRCM composites without short carbon fibers

The point at which the drastic changes initiates in the electrochemical performance is defined as the service life of the MFRCM composites. Fig. 4.3 shows the relationship between service life and current density for MFRCM composites. As current density increases, the service life shows a similar decreasing trend for the composites regardless of the presence of short carbon fibers. The service life can also be expressed in terms of charge density which equals the product of current density and polarization time. Fig. 4.4 shows the relationship between charge density at service life and current density for MFRCM composites. The results show that the charge density at service life is close for MFRCM composites polarized at different current densities. Thus, the service life of the MFRCM composites is taken as the average value of charge densities obtained for different current densities, which is equal to  $1501200 \text{ C/m}^2$ .

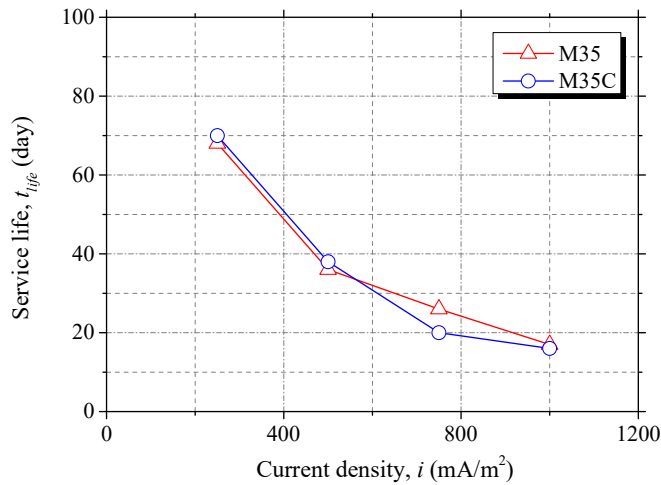


Fig. 4.3 Relationship between service life and current density for MFRCM composites

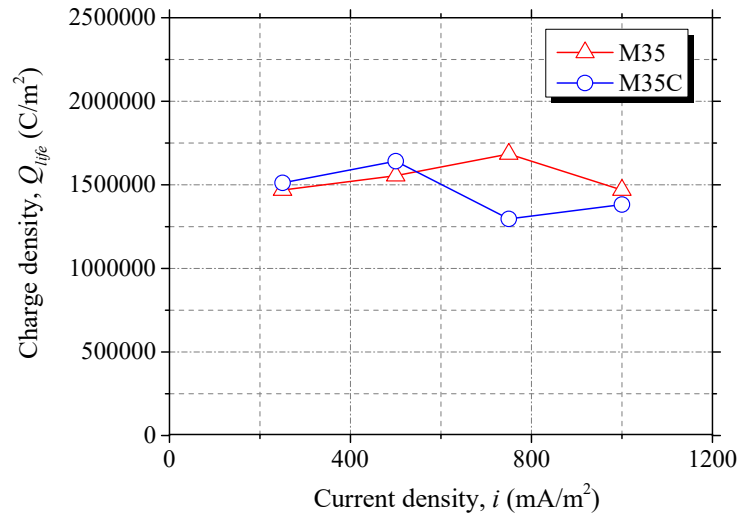
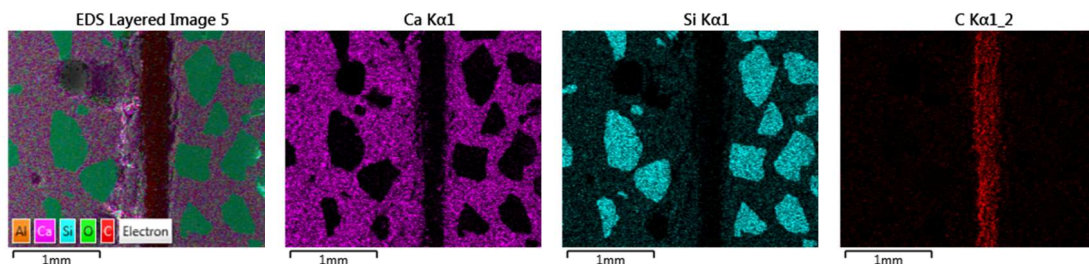


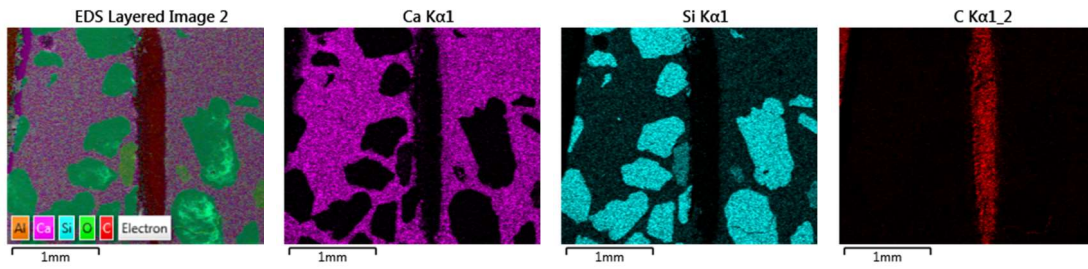
Fig. 4.4 Relationship between charge density at service life and current density for MFRCM composites

#### 4.3.2 Elemental distribution in the matrix around the carbon fabric

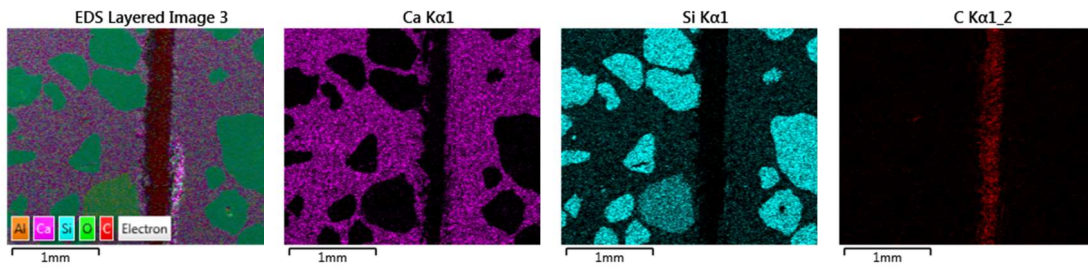
EDS was employed to characterize the elemental distribution in the cementitious matrix near the carbon fabric. As the inclusion of short carbon fibers does not affect the EDS results, only the results of MFRCM composites without short carbon fibers are shown in Fig. 4.5. The overlapped and individual distribution of different elements in the cementitious matrix nearby the carbon fabric is indicated. The elements to be analyzed consist of calcium, silica and carbon. The local intensified distribution of silica and carbon is attributed to the presence of fine aggregate and carbon fabric, respectively. It can be found that the calcium is still distributed around the embedded carbon fabric for MFRCM composites despite the applied current density, and there is no sign of a significant reduction in calcium content near the carbon fabric. In some cases, there exists a degradation zone near the anode, which is characterized by decreased calcium content (Peelen et al. 2008; Koster et al. 2009; Zhang 2018). This is due to that as hydroxyl ions are being consumed during anodic electrode reaction, the calcium-containing cement hydrates would dissolve and the calcium ions be released into the pore solution, which will then migrate from the anode towards the cathode under the external electric field. However, when the carbon fabric serves the anode, a sufficient amount of cement hydrates is precipitated on the carbon fabric as a large surface area can be achieved for the fabric consisting of thousands of fine carbon filaments. The reason can be further suggested by SEM and EDS analyses on the carbon fabric.



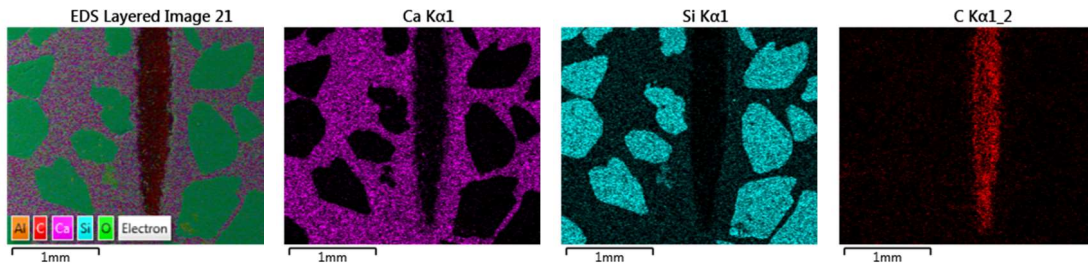
(a) M35-Ref



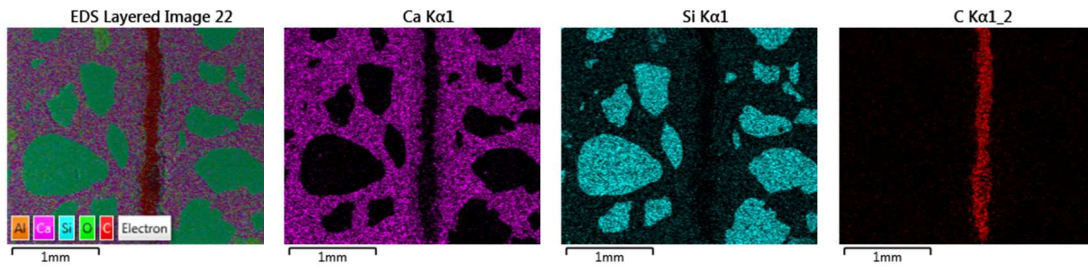
(b) M35-T45-i20



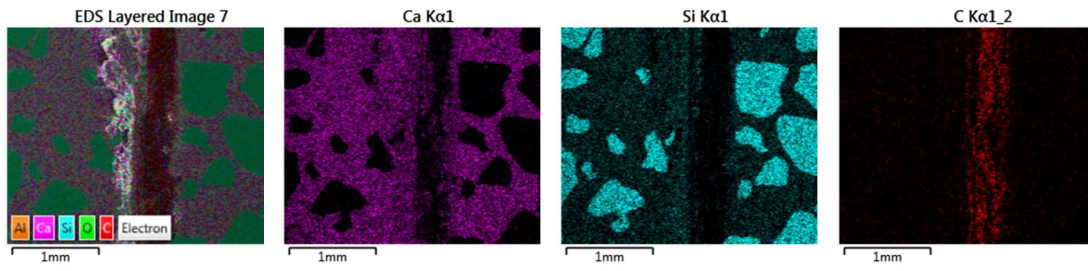
(c) M35-T45-i60



(d) M35-T45-i125



(e) M35-T45-i250



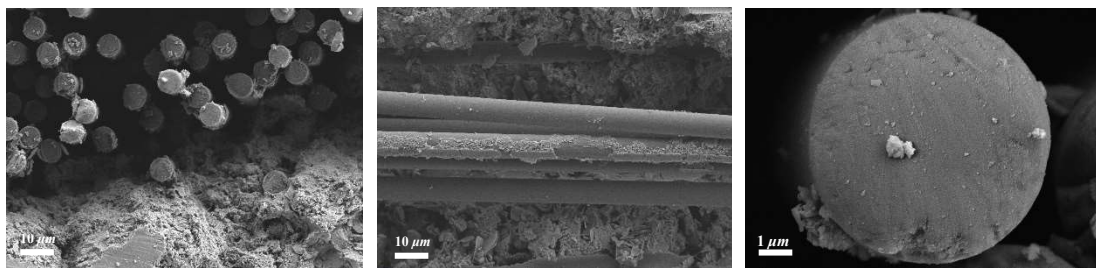
(f) M35-T45-i500

Fig. 4.5 EDS results of the matrix around the carbon fabric in MFRCM composites without short carbon fibers

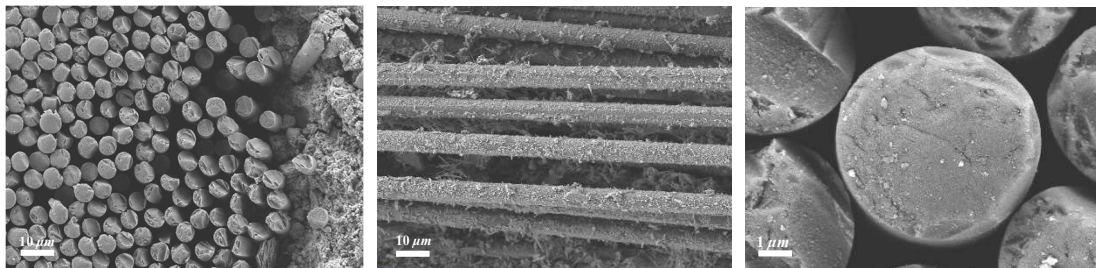


### 4.3.3 Morphology and surface elements of the embedded carbon fabric

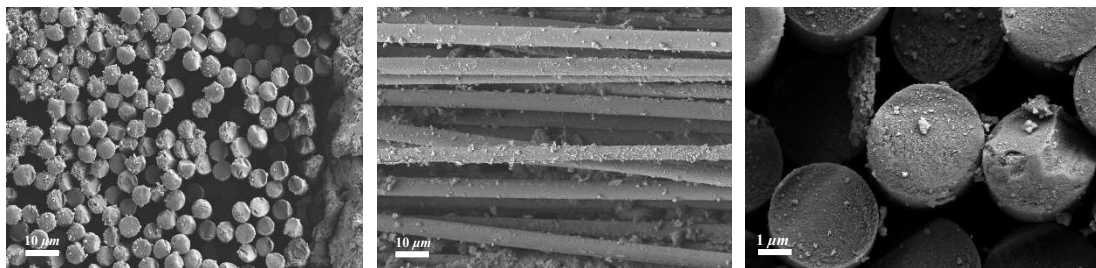
The morphology of the carbon fabric was examined for the MFRCM composites under anodic polarization. Fig. 4.6 shows SEM images of carbon fabric in the MFRCM composites without short carbon fibers. For reference MFRCM composites, the carbon filaments exhibit a smooth surface and are partially coated by the cement hydrates, and the cross-section remains flat as well. With increasing current density to  $60 \text{ mA/m}^2$ , there is little change in the surface morphology of the carbon filaments, while the cross-section shows a sign of unevenness. As current density is further increased, multiple transverse cracks occur along the longitudinal axis of carbon filaments, and the cross-section of filaments evolves into uneven and spalling states. The spalling state is characterized by the superficial pieces separated from the core of the filament. Filament cracking is because anodic electrode reactions destroy the microstructure of the carbon filaments, which will be discussed later.



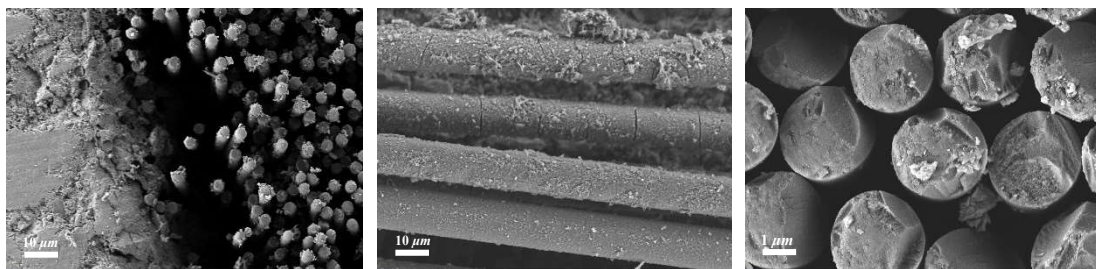
(a) M35-Ref



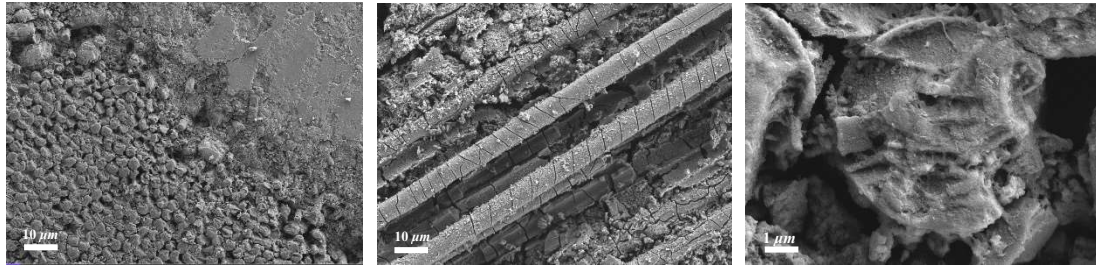
(b) M35-T45-i20



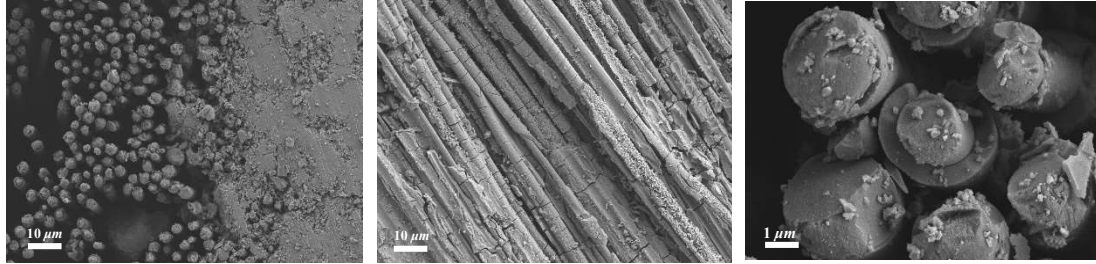
(c) M35-T45-i60



(d) M35-T45-i125



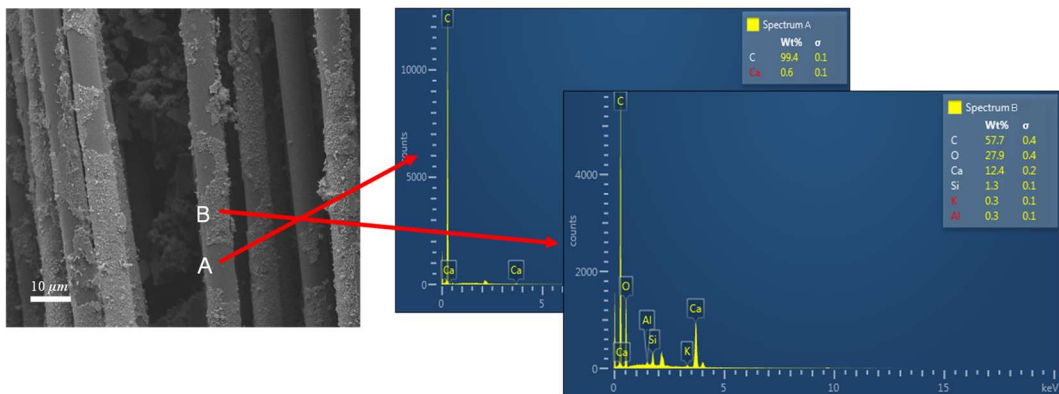
(e) M35-T45-i250



(f) M35-T45-i500

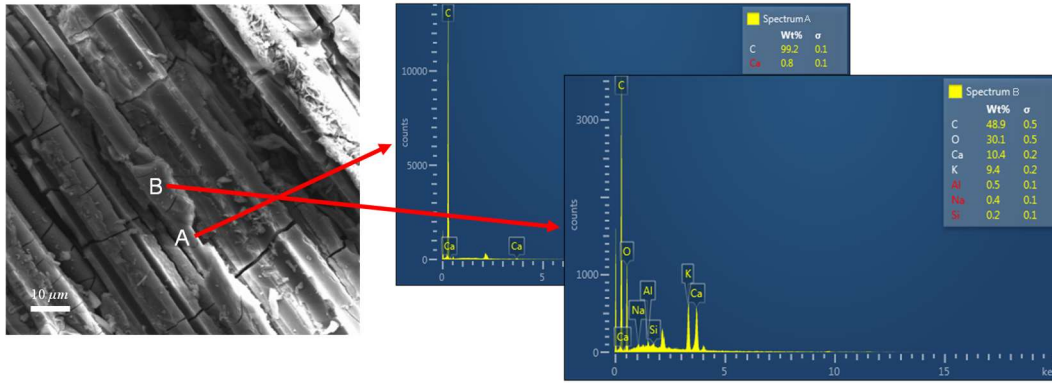
Fig. 4.6 SEM images of carbon fabric in MFRCM composites without short carbon fibers

EDS was also carried out on MFRCM composites in order to analyze the effects of anodic polarization on surface elements of the carbon fabric. Fig. 4.7 presents the EDS results of the carbon fabric in MFRCM composites without short carbon fibers. As can be seen, the principal chemical composition consists of calcium and oxygen, indicating the presence of precipitated cement hydrate, such as portlandite (CH). While the applied current density is  $500 \text{ mA/m}^2$ , the chemical composition of the hydrates on the carbon fabric in the composites is similar to that observed for the reference composite. The SEM observation and EDS results confirm that there is no severe calcium leaching caused by the anodic polarization, which is inconsistent with the previous section regarding the element mapping of the cementitious matrix around carbon fabric.



(a) M35-Ref



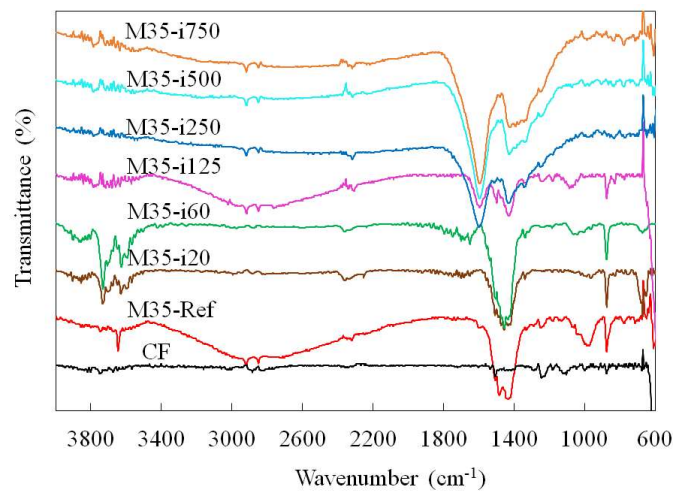


(b) M35-T45-i500

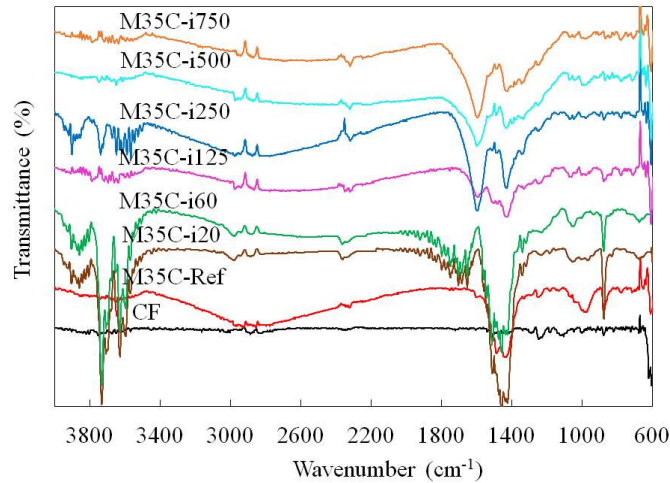
Fig. 4.7 EDS results of carbon fabric in the MFRCM composites without short carbon fibers

#### 4.3.4 Surface chemical composition of the embedded carbon fabric

Fig. 4.8 shows the FTIR spectra of carbon fabric in the MFRCM composites without and with short carbon fibers. For comparison purposes, the FTIR spectrum for the as-received carbon fabric is also included in Fig. 4.8. The results show that the spectra of the composites exhibit similar variations for various current densities regardless of the presence of short carbon fibers. Table 4.2 shows the interpretation of the peaks in the FTIR spectra for the MFRCM composites. Compared to the as-received carbon fabric, the reference composite shows two bands at around  $3640\text{ cm}^{-1}$  and  $1430\text{ cm}^{-1}$  that are related to O-H stretching vibration and O-H in-plane deformation vibration, which is due to that the adsorbed hydroxyl ions from the pore solution of the matrix. The band appears at about  $980\text{ cm}^{-1}$ , which is because of the introduction of C-OH onto the carbon fabric in the composites during anodic polarization. Likewise, the bands at  $1600\text{ cm}^{-1}$  and  $1245\text{ cm}^{-1}$ , which are associated with the stretching vibration of C=O and C=C (Sellitti et al. 1990; Zielke et al. 1996; Boehm 2002; Lee et al. 2017) and the stretching vibration of C-O-C, are also introduced onto the carbon fabric in the composites. The functionalities on the carbon fabric are increased during anodic polarization in comparison to the as-received carbon fabric.



(a)



(b)

Fig. 4.8 FTIR spectra of carbon fabric in the MFRCM composites without (a) and with (b) short carbon fibers

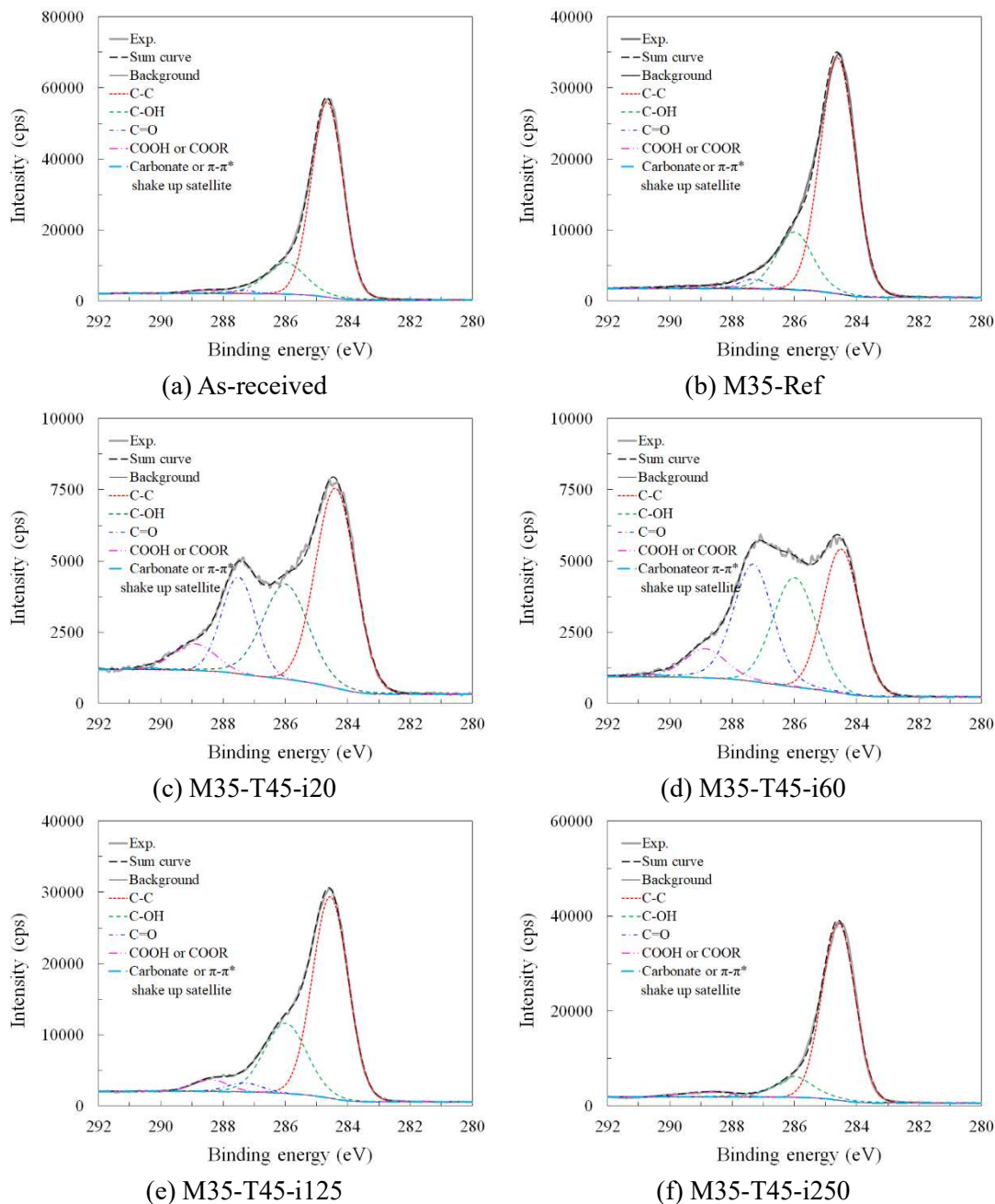
Table 4.2 Interpretation of the peaks in the FTIR spectra for MFRCM composites

Peak (cm <sup>-1</sup> )	Interpretation
3640	O-H stretching vibration
1600	C=O and C=C stretching vibration
1430	O-H in-plane deformation vibration
1245	C-O-C stretching vibration
980	C-OH stretching vibration

In addition to FTIR, XPS was conducted to quantify the content of functional groups on the carbon fabric in the MFRCM composites, with the aim at examining the impacts of anodic polarization. As the FTIR analysis suggests that the changes in the functional groups of carbon fabric are similar for the MFRCM composites without and with short carbon fibers, only the results obtained from the composites without short carbon fibers are presented. Fig. 4.9 displays C1s high-resolution spectra of carbon fabric in the MFRCM composites without short carbon fibers. For comparison purposes, the C1s spectrum of the as-received carbon fabric is also included. The as-received carbon fabric shows a typical C1s spectrum featured an asymmetric peak centered at ca. 284.6 eV. The shape of the XPS spectra of carbon fabric in MFRCM composites varies, depending on the applied current density. To reveal the type and the content of the surface functional groups, the C1s spectra were deconvoluted with a Gaussian-Lorentzian mix function and Shirley background subtraction. Based on a literature survey, there are several types of carbon-containing functional groups that can be obtained from deconvoluting the C1s spectrum, as shown in Table 4.3.

Fig. 4.9 gives the deconvolution results of the C1s spectra of carbon fabric in MFRCM composites without short carbon fibers. The following deconvoluted peaks of C1s can be observed, including C-C (284.6 eV), C-OH (phenolic or alcohol groups, 286.3 eV), C=O (carbonyl or quinone groups, 287.1 eV), COOH or COOR (carboxyl groups, 288.4 eV) and carbon involved in CO<sub>3</sub><sup>2-</sup> or π-π\* shake-up satellite (290.8 eV). The XPS results are in line with the findings observed in FTIR analysis. The relative content of surface component

functionalities is tabulated in Table 4.4. In comparison to the reference composite, there is an increase in the content of C-OH, C=O, and COOH or COOR for the composites polarized at a current density up to 125 mA/m<sup>2</sup>, while the content of these groups experiences a reduction for large current densities. This is due to that for small current densities these functional groups can be introduced to carbon fabric by oxidizing the active carbon atoms, while as current density is increased, the groups can further be oxidized.



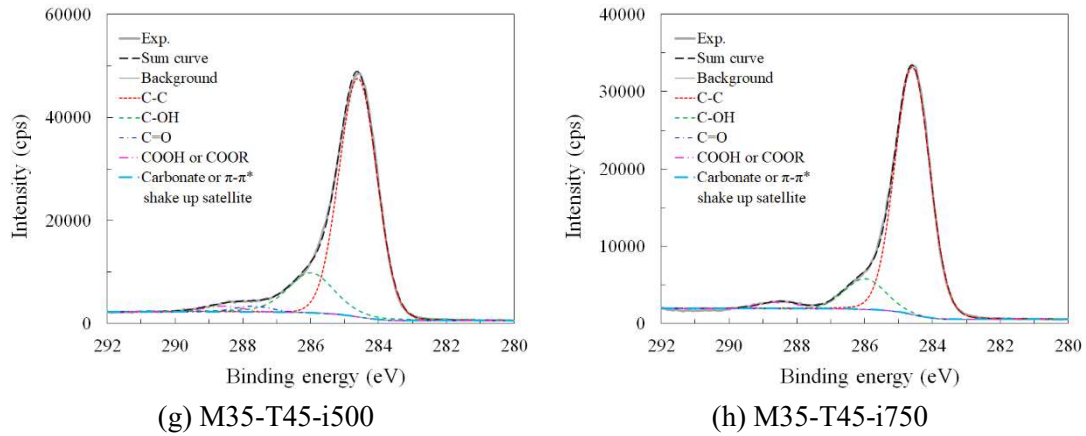


Fig. 4.9 Deconvoluted C1s XPS spectra of carbon fabric in MFRCM composites without short carbon fibers

Table 4.3 Possible carbon-containing functional groups on carbon fibers

Reference	The binding energy of carbon involved functionalities (eV)				
	C-C	C-OH	C=O	COOH or COOR	CO <sub>3</sub> <sup>2-</sup> or $\pi\sim\pi^*$ shake-up satellite
Harvey J. (1987)	284.6	286.2	287.6	288.6	290.6
Weitzsackert and Sherwood (1995)	284.6	286.1	287.7	289.1	290.6
Gardner et al. (1995).	284.6	286.1~286.3	287.6~287.7	288.6~289.0	290.6~290.7
Zielke et al. (1996)	284.6	286.1	287.6	288.1~289.1	---
Bubert et al. (2002)	284.5	286.5 (C-OR)	287.8	290.0	---
Yue et al. (1999)	284.6	286.1~286.3	287.3~287.6	288.4~288.9	290.4~290.8
Dai et al. 2011	284.6	286.1	287.7	289.4	290.6
Liu et al. (2010a, 2010b)	284.6	286.0~286.4	287.1~287.3	289.0~289.4	---
H. Song et al. (2016)	284.4	286.2	287.5	288.5	---
Lee et al. (2017)	284.6	286.6 (-OH, C-O)	288.9	288.9	---

Table 4.4 The content of functional groups of carbon fabric in the MFRCM composites

Sample	The relative content of surface components				
	C-C	C-OH	C=O	COOH or COOR	CO <sub>3</sub> <sup>2-</sup> or $\pi\sim\pi^*$ shake up satellite
CF	79.7%	17.9%	1.0%	1.3%	0.0%
M35-T45-Ref	74.9%	21.1%	2.5%	1.3%	0.3%

M35-T45-i20	46.5%	27.2%	19.3%	6.7%	0.3%
M35-T45-i60	32.4%	28.8%	30.5%	8.0%	0.3%
M35-T45-i125	65.4%	28.2%	2.8%	3.7%	0.0%
M35-T45-i250	78.8%	16.5%	1.5%	3.3%	0.0%
M35-T45-i500	78.0%	18.1%	1.9%	2.0%	0.0%
M35-T45-i750	85.3%	12.4%	0.0%	2.3%	0.0%

#### 4.4 Discussion

Due to the characteristic of carbon fiber precursors and the manufacturing process, carbon filaments exhibit anisotropic material properties in the radial direction. A layered structure is formed for carbon filaments, which is well known as the sheath-core structure. Carbon filaments consist of many hexagonal crystalline layers as basic structural elements, which are highly oriented parallel to the fiber axis in the sheath region and disoriented in the core region. Fig. 4.10 shows a schematic diagram of the carbon filaments' sheath-core structure, according to (Raphael et al. 2018). The sheath region is featured by fewer defects, higher density, larger oxygen content and higher mechanical strength compared to the core region. In hexagonal basal planes that ply up to form the crystalline layer,  $sp^2$  hybridized carbon atoms are connected through a covalent bond, while the plied crystalline layers connected due to Van der Waals force. The recognition of the microstructure of carbon filaments is helpful to understand the degradation mechanisms of carbon fabric in the MFRCM composites subjected to anodic polarization.

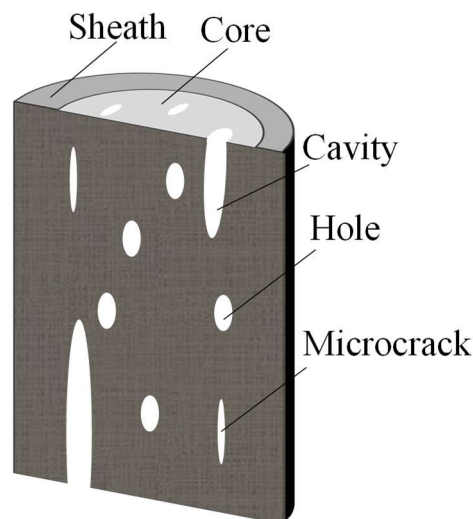
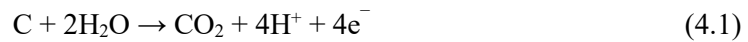


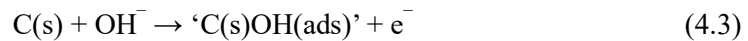
Fig. 4.10 Schematic diagram for carbon filaments' sheath-core structure

Due to the chemical nature of graphitic layers on the surface of carbon filaments, carbon filaments behave like an inert material. In order to improve the wettability of carbon filaments, anodic oxidation is often used as a surface treatment method, which can introduce different oxide species onto the surface of the filaments. It has been found that carbon filaments anodically polarized showed various degradation, depending on the electrolytic media and operating conditions (Bismarck et al. 1999; Kainourgios et al. 2017; Liu et al. 2010a; Sun et al. 2019; Yue et al. 1999). In the acidic and neutral electrolyte, carbon dioxide is evolved by

oxidizing carbon atoms, while oxygen evolution occurs due to oxidation of hydroxyls in the alkaline electrolyte. Eq. (4.1) takes place in acidic or neutral aqueous solutions, while the electrode reaction becomes oxygen evolution in the alkaline solution, as shown in Eq. (4.2).



The dissolution of anodically polarized carbon filaments in acid solutions is attributed to direct oxidation of carbon atoms, while the mechanism of carbon filaments dissolved in alkaline solutions is more complicated. In the alkaline media, the hydroxyl radicals are produced through oxidizing hydroxyl ions according to Eq. (4.3) (Kozłowski and Sherwood 1985; Christensen et al. 1999).



Where C(s) indicates that microstructure of carbon filaments remains intact,

The radicals further react to produce different functionals on the carbon filaments, including phenolic, alcohol, carbonyl, quinone and carboxyl groups. Fig. 4.11 shows the possible functionals introduced to the carbon fibers (Zielke et al. 1996). While for the surface of carbon filaments, the crystalline layers are highly ordered along the longitudinal axes. The oxidation on the surface of carbon filaments usually initiates at the active sites, as such sites can provide more free valences.

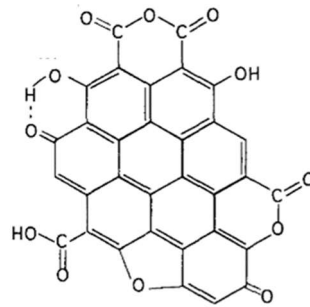
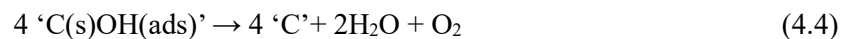


Fig. 4.11 Possible functionals introduced to the carbon fiber

In addition to introducing different oxides, the degradation of anodically polarized carbon filaments also proceeds. After the formation of free radicals, they will be further decomposed and thus lead to the dissolution of carbon filaments. Eq. (4.4) shows the reactions responsible for the breakage of carbon filaments (Kozłowski and Sherwood 1985; Christensen et al. 1999).



Where 'C' implies the breakage of graphitic layers in carbon filaments.

It can be seen that anodic polarization of carbon fabric in alkaline media is essentially a corrosive process, which accounts for the occurrence of cracks on the carbon filaments during polarizing MFRCM composites. A schematic diagram is used to illustrate how the corrosion process caused by anodic polarization affects the morphology of carbon filaments in MFRCM composites, as shown in Fig. 4.12. If the composites are without or with little anodic polarization, the carbon fiber remains intact. Once the cracks occur in the carbon filaments, the corrosive anodic reaction propagates from the surface towards the core and eventually causes the filaments to break. As evidenced in SEM observations, most cracks on the carbon filaments



after anodic polarization are oriented transverse to the longitudinal axis. In this case, the carbon filaments can be inferred to suffer from localized corrosion along the cracks during anodic polarization. This is probably due to that capillary action is present when embedding multifilament carbon fabric inside the matrix, and the matrix pore solution that connects carbon filament with matrix or connects filament with filament is distributed in a discrete manner. The anodic polarization is solely possible when there is a pore solution that constitutes a continuous electrolytic media between matrix and carbon filaments or among filaments. With the development of cracking, the pore solution can penetrate the carbon filament through the cracks, which allows the filament to be corroded at the internal defects, such as holes, microcracks and cavities. The internal corrosion of the filaments could happen randomly, which may enlarge holes or cavities and prolong micro-cracks, and therefore increase the possibilities of occurrence of an uneven cross-section of the filaments. If the corrosive process propagates across the radial directional of carbon filament, the filament will fracture. If the internal corrosion proceeds along the axis of the fiber, the transverse connection between the graphitic layers is reduced. Besides, the ingress of the pore solution also increases the distance between the graphitic layers, and thus surface fragments will spall from the filament with exposing the internal part, as shown in Fig. 4.12.

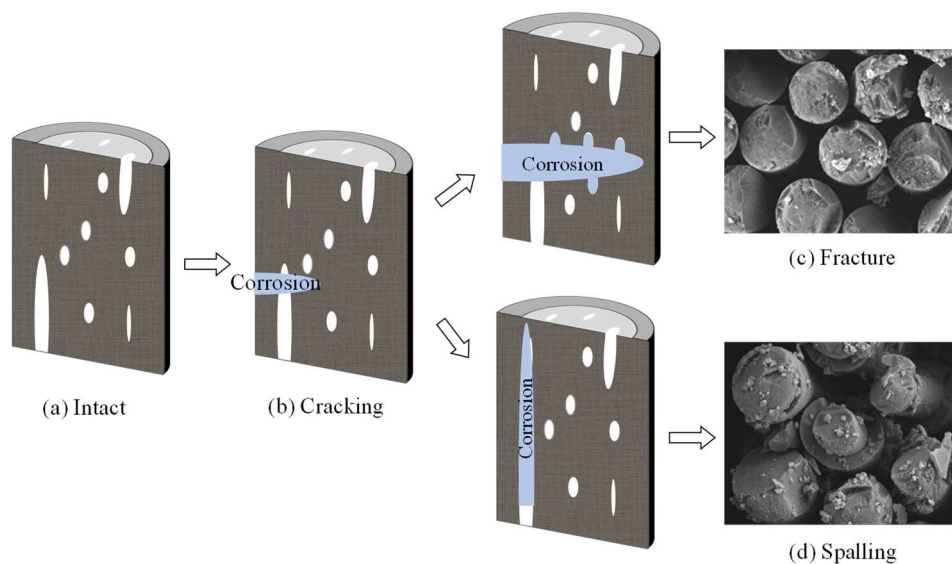


Fig. 4.12 Degradation of carbon filaments in the MFRMC subjected to anodic polarization

The degradation of carbon fabric in the MFRMC composites with anodic polarization can also be correlated with the electrochemical performance. Fig. 4.13 illustrates the overall tendency of cell voltage for the MFRMC composites with anodic polarization. For current densities smaller than  $125 \text{ mA/m}^2$ , cell voltage exhibits a slight increase during anodic polarization, while larger current densities cause an exponential growth after a certain period. In the case of the composites with little anodic polarization (a→b), i.e. with small current densities, the carbon-containing functional groups are introduced to the carbon filaments and the fiber cracks caused by anodic polarization appear. Both introduced functionalities and cracks result in lowering the conductivity of the filament, as the functional groups normally have a small conductivity (Chung 2002) and the cracks reduce the cross-section. When the filaments are broken for MFRMC composites polarized at larger current densities (b→c(d)), the anodic surface area of

the carbon fabric can be remarkably decreased due to significant damage and thus an exponential rise in the cell voltage can be caused.

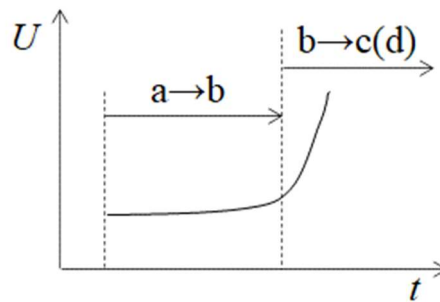


Fig. 4.13 Schematic interpretation of the effect of anodic polarization on cell voltage for MFRCM composites

#### 4.5 Conclusions of this chapter

Based on the test results and analysis, the main conclusions can be drawn as follows.

MFRCM composites can maintain the relatively stable electrochemical performance for an anodic current density up to  $125 \text{ mA/m}^2$ , while for larger current densities a significant rise in cell voltage can be seen for the composite after being polarized for a certain period. The service life of the composites shows a reduction with increasing the current densities regardless of the presence of short carbon fibers in the composites. Further, the estimated charge density at the service life is close for the composites polarized at various current densities, which is about  $1501200 \text{ C/m}^2$ .

During polarization, the carbon fabric within the MFRCM composites shows a sign of severe degradation. The EDS results show that the elemental distribution of calcium and silica in the matrix close to the carbon fabric is not significantly affected, and the matrix does not endure severe calcium depletion, as evidenced by a high amount of calcium on the carbon fabric in the MFRCM composites. Instead, the carbon fabric is subjected to severe degradation during polarization. SEM images indicate the changes in the morphology of carbon filaments. Multiple transverse cracks occurred on the carbon filaments for the MFRCM composites with anodic polarization, and cracking further causes the filaments to break or spall.

The FTIR and XPS results show that anodic polarization has an apparent effect on the surface functional groups of the carbon fabric in the MFRCM composites. Regardless of the current density, the surface chemical composition of the carbon fabric is the same for all polarized MFRCM composites. The XPS results show that the functional groups increase on the carbon fabric during anodic polarization at a current density up to  $125 \text{ mA/m}^2$ , while larger current densities lead to a reduction in these functionalities.

It can be found that the degradation of MFRCM composites under anodic polarization is mostly related to damage in the carbon fabric due to the corrosive anodic reactions. The changes in the morphology of carbon filaments are a consequence of the corrosive anodic reactions and microstructural characteristics. In addition, the degradation of MFRCM composites can be also correlated to the electrochemical performance of the composites. With small current densities, the carbon-containing functional groups are introduced to the carbon filaments and the fiber



cracks caused by anodic polarization appear. Both introduced functionalities and cracks result in lowering the conductivity of the filament, as the functional groups normally have a small conductivity and the cracks reduce the cross-section. When the filaments are broken for MFRCM composites polarized at larger current densities, the anodic surface area of the carbon fabric can be remarkably decreased due to significant damage and thus an exponential rise in the cell voltage can be caused.

## Chapter 5

### 5 Bond behavior of carbon fabric in cementitious matrix subjected to anodic polarization

#### 5.1 Introduction

As previously mentioned, a comprehensive and sustainable repair method has been proposed to simultaneously achieve structural strengthening and corrosion control for reinforced concrete structures. The method combines the advantages of ICCP and SS and is, thus, called ICCP-SS. In the ICCP-SS systems, MFRCM, as a core component, should play a dual role as a reinforcement and an impressed current anode. Hence, the MFRCM composite should carry with its capacity of maintaining good electrochemical performance and transferring the stress to the structures to be strengthened. As for carbon FRCM composites without being considered as an anode, slippage of carbon fabric through the matrix is a common failure mode encountered in the mechanical characterization of the composites and the corresponding strengthening systems (Awani et al. 2017; Carozzi et al. 2020; Koutas et al. 2019). Hence, the mechanical behavior of carbon FRCM composites and the corresponding strengthening system depends greatly on the interfacial interaction between carbon fabric and cementitious matrix through the bond. A brief introduction about the research status and progress regarding the carbon fabric-cementitious matrix interfacial bond can refer to the introduction in Chapter 2 and Chapter 3. An extremely important factor affecting the bond behavior of carbon fabric in the cementitious matrix is matrix impregnation. As the matrix cannot fully penetrate the carbon yarn consisting of thousands of filaments, different bond characteristics are exhibited by these filaments, depending on their location on the cross-section. Considering the effect of matrix impregnation, these filaments can be grouped into two parts, the outer part and inner part, and two interfaces introduced, including the outer interface between the matrix and outer part and the inner interface between the outer part and inner part. The determination of the respective bond slip relationship for these two interfaces can refer to Chapter 3. Besides, the mechanisms of stress transfer and the contribution of outer and inner parts to carrying the applied force were also discussed.

Due to the electrical conductivity of carbon fabric, increasing attention has been paid to using it as an anode in ICCP for reinforced concretes (Chini and Antonsen 2008; Nguyen et al. 2012; Zhang and Tang 2014; Zhu et al. 2014, 2015). A summary of the research status and progress on carbon fiber anodes was presented in Chapter 4. It can be seen that the use of carbon fibers as an anode is relatively new and the information on the degradation behavior of carbon fibers is still rare. Besides, the existing relevant studies were mostly focused on the effectiveness of ICCP, electrochemical performance, degradation of CFRP anode and the surrounding matrix as well as the tensile stress of CFRP. However, no information is available on the stress transfer between carbon fabric and matrix after anodic polarization. This is a large gap to be filled towards a deep understanding of the mechanical behavior of MFRCM composites and the effectiveness of the structures repaired with ICCP-SS.

The objective of this chapter is to investigate the bond behavior of anodically polarized carbon fabric embedded in the cementitious matrix. Doubled-sided pullout tests were carried out on MFRCM composites without and with anodic polarization. Different levels of polarization were

achieved by applying different current densities (0 to 125 mA/m<sup>2</sup>) and durations (45 and 90 days). Different embedded lengths of carbon fabric in the matrix were considered, including 30, 50 and 70 mm. Afterwards, the respective bond slip relationship for the outer and inner interfaces was determined using pullout test results. At last, the effects of anodic polarization on the bond slip relationships were correlated to the extent of anodic polarization.

## 5.2 Experimental program

This chapter aimed at investigating the bond behavior between carbon fabric and cementitious matrix within MFRCM composites under anodic polarization. The MFRCM composites studied herein were the same as those in Chapter 4. The detailed information about the raw materials, preparation of MFRCM composites, curing and introduction of anodic polarization can refer to Chapter 4. After completing anodic polarization, samples were prepared for material characterization to reveal the mechanisms of degradation for the polarized composites, while at the same time specimens were also processed for subsequent pullout tests to investigate the carbon fabric-cementitious matrix interfacial bonding.

Asymmetrical double-sided pullout tests were conducted on the polarized MFRCM composites, where specimen preparation and specimen configuration were the same as those in Chapter 3. Three embedded lengths of 30, 50 and 70 mm were considered. According to the matrix type, polarization period, current density and embedded length, the pullout specimens were labeled in the following rule. Taking specimen M35C-T45-i20-L30 for example, M35C means that the specimen is made of matrix M35C with short carbon fibers (and matrix M35 without short carbon fibers); T45 means that the polarization time is 45 days; i20 means that the current density is 20 mA/m<sup>2</sup>; and L30 means that the embedded length is 30 mm. For comparison, specimens labeled as M35-Ref and M35C-Ref indicates the specimens without anodic polarization for the composites without and with short carbon fibers, respectively. Test parameters for pullout tests performed on the polarized MFRCM composites are shown in Table 5.1. Note that the composites polarized at a current density at  $\geq 250$  mA/m<sup>2</sup> were not tested, as these composites exhibited very severe degradation and the corresponding specimens were easy to break during specimen preparation. Before pullout tests, likewise, the pullout test specimens were strengthened with gluing CFRP sheets to their both ends to facilitate clamping. Testing machine and measuring instruments as well as the test implementation were the same as those in Chapter 3.

Table 5.1 Test parameters for pullout tests performed on the polarized MFRCM composites

No	Specimen	Short carbon fibers	$i$ (mA/m <sup>2</sup> )	$t$ (day)	$L_b$ (mm)
1	M35-Ref-L30		0	0	30
	M35-Ref-L50		0	0	50
	M35-Ref-L70		0	0	70
2	M35-T45-i20-L30		20	45	30
	M35-T45-i20-L50	NO	20	45	50
	M35-T45-i20-L70		20	45	70
3	M35-T45-i60-L30		60	45	30
	M35-T45-i60-L50		60	45	50
	M35-T45-i60-L70		60	45	70

	M35-T45-i125-L30		125	45	30
4	M35-T45-i125-L50		125	45	50
	M35-T45-i125-L70		125	45	70
	M35-T90-i20-L30		20	90	30
5	M35-T90-i20-L50		20	90	50
	M35-T90-i20-L70		20	90	70
	M35-T90-i60-L30		60	90	30
6	M35-T90-i60-L50		60	90	50
	M35-T90-i60-L70		60	90	70
	M35-T90-i125-L30		125	90	30
7	M35-T90-i125-L50		125	90	50
	M35-T90-i125-L70		125	90	70
	M35C-Ref-L30		0	0	30
8	M35C-Ref-L50		0	0	50
	M35C-Ref-L70		0	0	70
	M35C-T45-i20-L30		20	45	30
9	M35C-T45-i20-L50		20	45	50
	M35C-T45-i20-L70		20	45	70
	M35C-T45-i60-L30		60	45	30
10	M35C-T45-i60-L50		60	45	50
	M35C-T45-i60-L70		60	45	70
	M35C-T45-i125-L30		125	45	30
11	M35C-T45-i125-L50	Yes	125	45	50
	M35C-T45-i125-L70		125	45	70
	M35C-T90-i20-L30		20	90	30
12	M35C-T90-i20-L50		20	90	50
	M35C-T90-i20-L70		20	90	70
	M35C-T90-i60-L30		60	90	30
13	M35C-T90-i60-L50		60	90	50
	M35C-T90-i60-L70		60	90	70
	M35C-T90-i125-L30		125	90	30
14	M35C-T90-i125-L50		125	90	50
	M35C-T90-i125-L70		125	90	70

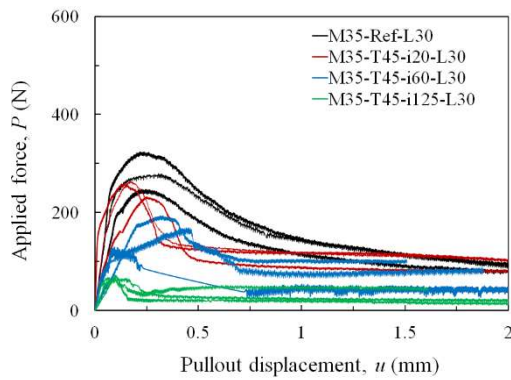
### 5.3 Results and discussions

#### 5.3.1 Pullout test results

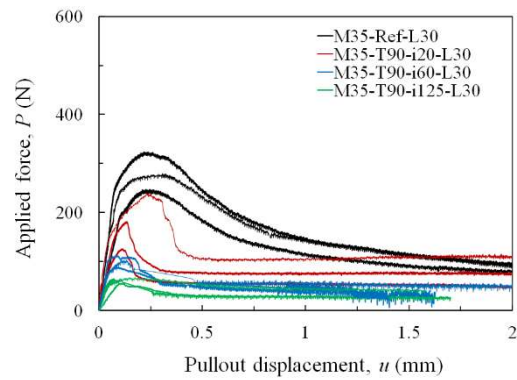
Fig. 5.1 and Fig. 5.2 show the applied force versus displacement for the MFRCM composites without and with short carbon fibers, respectively. Regardless of the presence of short carbon fibers, current density, polarization time and embedded length, all the specimens exhibit similar pullout behavior that is featured as an ascending branch up to the peak and a descending branch followed by a slowly descending tail. With introducing anodic polarization, the pullout behavior of MFRCM composites is compromised, depending on current density. As current density is increased, the peak pullout force and the residual force are lowered for the polarized MFRCM composites, indicating degradation in the load transfer between carbon fabric and cementitious matrix. Besides, most pullout specimens exhibited a similar failure characterized by the

slippage-partial rupture of the carbon yarn, except the reference pullout specimens with a 30 mm long embedded length. These reference specimens failed due to the slippage of the whole carbon yarn through the matrix. It is worth mentioning that other specimens with 30 mm embedded length and with anodic polarization showed the slippage-partial rupture of the carbon yarn, which was caused by the polarization induced degradation rather than the applied force. For the polarized pullout specimens with longer embedded lengths, they failed by the slippage-partial rupture of the carbon yarn, while the rupture was due to combined effects of the applied force and the polarization induced degradation.

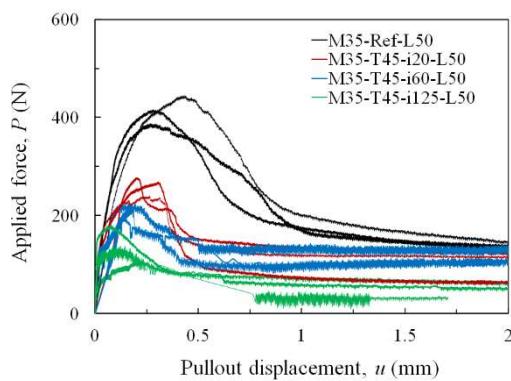
The degraded pullout behavior can be related to the degradation mechanisms for MFRCM composites with anodic polarization. As evidenced, anodic polarization causes degradations in the morphology in the carbon fabric and matrix, such as filament cracking and spalling. The mechanical properties of carbon fabric and the interfacial bond between carbon fabric and matrix are, therefore, strongly affected. The degradation of polarized MFRCM composites depends on current density. With increasing current density, the carbon fabric in the composite is subject to more severe deterioration characterized by multiple transverse cracks on the filaments, the increased number of deteriorated filaments and thus the reduced cross-sectional area of the carbon yarn.



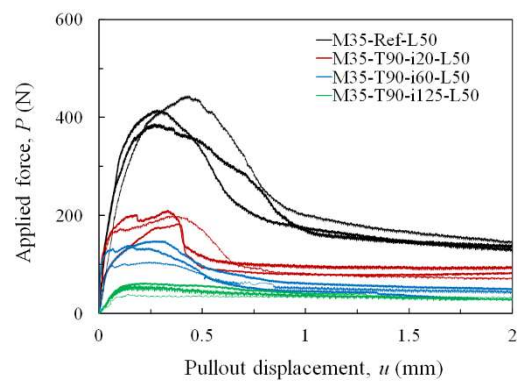
(a) M35-T45-L30



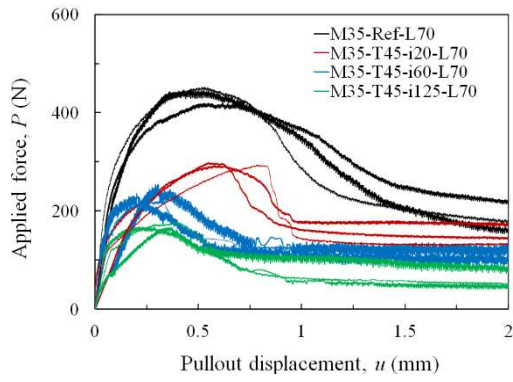
(b) M35-T90-L30



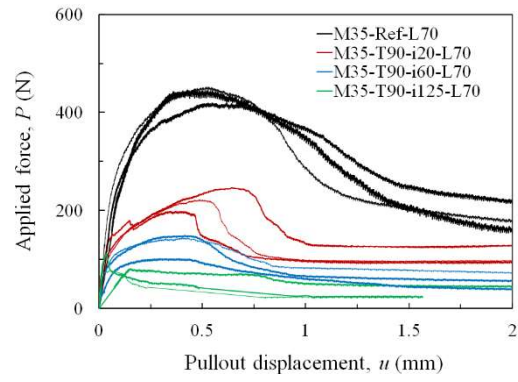
(c) M35-T45-L50



(d) M35-T90-L50

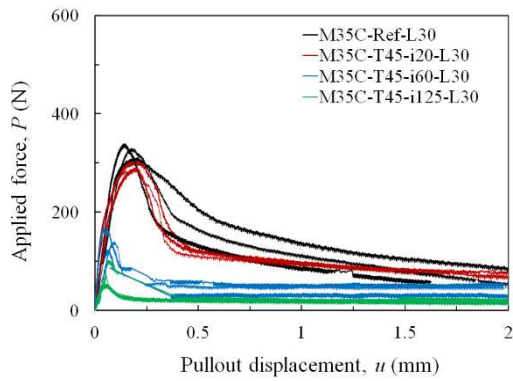


(e) M35-T45-L70

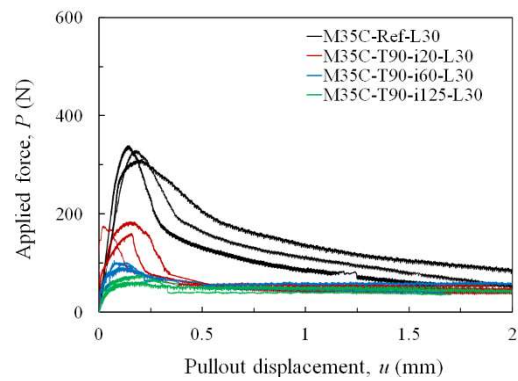


(f) M35-T90-L70

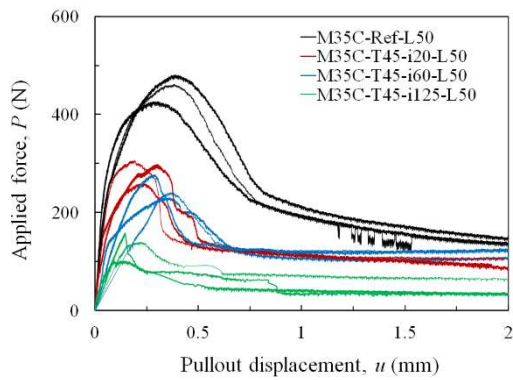
Fig. 5.1 The applied force versus displacement curve for M35 composites



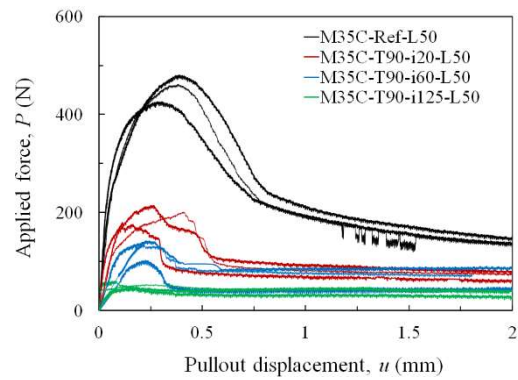
(a) M35C-T45-L30



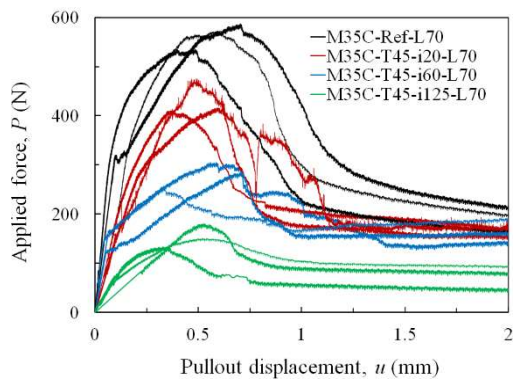
(b) M35C-T90-L30



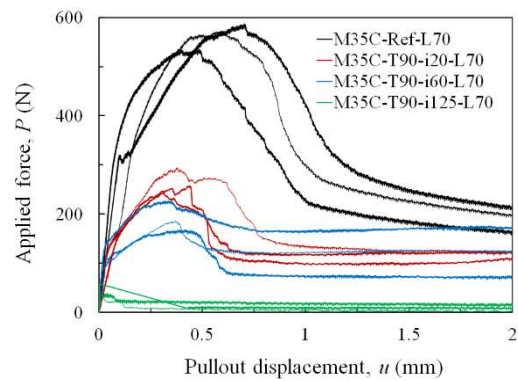
(c) M35C-T45-L50



(d) M35C-T90-L50



(e) M35C-T45-L70



(f) M35C-T90-L70

Fig. 5.2 The applied force versus displacement curve for M35C composites

### 5.3.2 Effects of anodic polarization on sectional area of the embedded carbon yarn

MFRCM composites would suffer from severe degradation after being subjected to anodic polarization. Before the evaluation of the bond slip relationship for the outer and inner interface, the changes in the cross-sectional area of the embedded yarn due to polarization induced degradation should be first known. The embedded carbon yarn can be subdivided into two parts due to limited and stochastic matrix impregnation, and an approach was proposed to evaluate the percentage of impregnated part within an embedded yarn based on the image processing and analysis. The results show that 30% of the filaments can be impregnated by matrix. However, some problems were encountered when applying this approach to evaluate the impregnation percentage for the MFRCM composites after anodic polarization. When analyzing the number of filaments remained in the matrix after pullout tests for the polarized composites, it is hard to differentiate these filaments due to pullout tests or the polarization induced deterioration and thus classify them into the outer part or inner part. In addition, it is also difficult to obtain clear sectional images of the polarized MFRCM composites, as the broken pieces of filaments caused by anodic polarization blur the captured sectional images.

Although the image processing and analysis described in Chapter 3 cannot apply to the MFRCM composites after anodic polarization, it is possible to estimate the changes in the cross-sectional area of the outer part based on the experimental pullout curves. By analyzing the applied force versus pullout displacement curve of pullout specimens with 50 mm embedded length, it can be seen that the force carried by the outer part at the beginning of progressive failure can be approximated by the difference between the peak pullout force and the force carried by the inner part, and the latter can be obtained by extrapolating the pullout curves after breakage of the outer part. Hence, the cross-sectional area of the outer part can be obtained by dividing the tensile capacity of the outer part by the effective tensile strength.

Before analyzing the effects of anodic polarization on changes in the cross-section, the concept of the extent of anodic polarization was introduced. According to Faraday's law of electrolysis, the amount of product formed on the electrode is proportional to the quantity of the charge passed through the electrode. Besides, the degradation of carbon fabric within the MFRCM composites is associated with the products produced during the electrochemical reaction on the fabric. The degradation is herein related to the charge passed through the carbon fabric during anodic polarization. In the present study, the actual charge density passed through the carbon fabric in the MFRCM composites is normalized to the charge density at the service life of the composites, which is also termed the extent of anodic polarization,  $\alpha$ .

The estimated changes in the cross-sectional area for the outer part are expressed by the outer sectional reduction factor,  $\beta_{A_{out}}(\alpha)$ , which is defined as the ratio of reduction in the cross-sectional area of the outer part after anodic polarization to the original area of the outer part. Thus Eq. (5.1) can be used to calculate  $\beta_{A_{out}}(\alpha)$ .

$$\beta_{A_{out}}(\alpha) = \frac{A_{out}(\alpha=0) - A_{out}(\alpha)}{A_{out}(\alpha=0)} \quad (1)$$

Where  $A_{out}(\alpha=0)$  is the cross-sectional area of the outer part before anodic polarization;  $A_{out}(\alpha)$  is the cross-sectional area of the outer part after anodic polarization with a certain level of  $\alpha$ .

As observed in SEM, the filaments in the inner part were also subjected to polarization induced deterioration, and thus the cross-sectional area of the inner part was reduced. For the total cross-sectional area of the embedded carbon yarn, there is a full reduction can be found for the composites polarized at the service life. When the service life is exceeded, most filaments in the composite are broken and the corresponding the pullout specimens show a peak force close to zero. The reduction of the cross-section of the carbon yarn is due to the cracking of filaments caused by anodic polarization, and the reduction is related to the product formed during the anodic electrode reaction, which is proportional to the quantity of charge. A linear variation was postulated for the reduction in the cross-sectional area of the whole carbon yarn with increasing the charge density. Upon the evaluation of changes in the cross-sectional area of the whole carbon yarn and the outer part, it is likely to evaluate the changes in the area of the inner part. Likewise, the estimated changes in the cross-sectional area for the inner part are expressed by the inner sectional reduction factor,  $\beta_{A_{in}}(\alpha)$ , which is defined as the ratio of reduction in the cross-sectional area of the inner part after anodic polarization to the original area of the inner part. Thus Eq. (5.2) can be used to calculate  $\beta_{A_{in}}(\alpha)$ .

$$\beta_{A_{in}}(\alpha) = \frac{A_{in}(\alpha=0) - A_{in}(\alpha)}{A_{in}(\alpha=0)} \quad (5.2)$$

Where  $A_{in}(\alpha=0)$  is the cross-sectional area of the inner part before anodic polarization;  $A_{in}(\alpha)$  is the cross-sectional area of the original inner part with a certain level of  $\alpha$ .

Fig. 5.3 shows the sectional reduction factor versus  $\alpha$  for the outer and inner part of the embedded carbon yarn in the MFRCM composites without and with short carbon fibers. The presence of short carbon fibers has a marginal effect on the sectional reduction factor. The sectional reduction factor shows an ascending trend for both the outer and inner parts with increasing the extent of anodic polarization, which means their cross-sectional area is reduced during anodic polarization. The outer part's cross-section starts to decrease once anodic polarization takes place, while the reduction in the cross-section of the inner part occurs until a certain extent of anodic polarization is reached. That is to say, the polarization induced deterioration is mostly imposed on the outer part instead of the inner part for a small extent of anodic polarization. It is reasonable that the filaments in the outer part are more vulnerable, as they are closer to the matrix than the filaments in the inner part and the anodic reaction can proceed more easily on the outer part. Eq. (5.3) can be found to fit the relationship between  $\beta_{A_{out}}(\alpha)$  and  $\alpha$  with good accuracy, which leads to  $R = 0.93$ . And the relationship between  $\beta_{A_{in}}(\alpha)$  and  $\alpha$  can also be fitted by Eq. (5.4) with  $R = 0.90$ .

$$\beta_{A_{out}}(\alpha) = \alpha^{0.33} \quad (5.3)$$

$$\beta_{A_{in}}(\alpha) = \begin{cases} 0 & \alpha < 0.16 \\ 1 - \frac{1 - \alpha - \beta_m [1 - \beta_{A_{out}}(\alpha)]}{1 - \beta_m} & \alpha \geq 0.16 \end{cases} \quad (5.4)$$

Where  $\beta_m$  is the percentage of the sectional area of the outer part to the whole carbon yarn before anodic polarization, i.e. the degree of matrix impregnation.



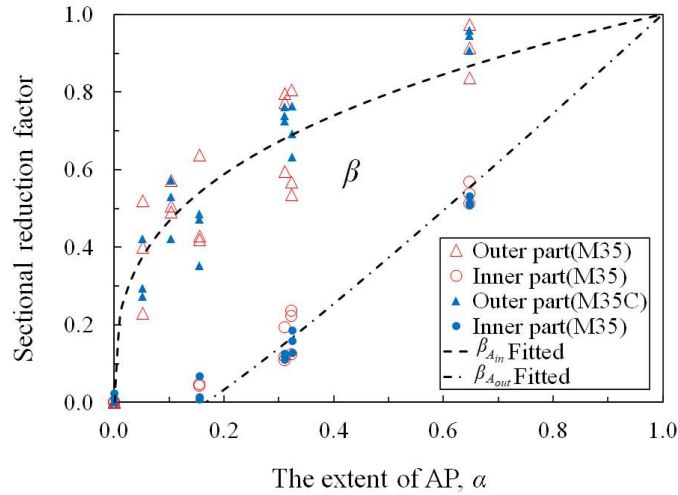


Fig. 5.3 The relationship between sectional reduction factor and  $\alpha$  for the inner and outer parts for MFRCM composites without and with short carbon fibers

### 5.3.3 Effects of anodic polarization on bond slip relationship for the outer interface

As previously described, the bond behavior of the outer part should be evaluated using the pullout test results with short embedded length. In such a case, the specimens fail due to the slippage of the whole carbon yarn, and the corresponding global behavior is dominated by the bond behavior of the outer interface. For the MFRCM composites with 30 mm long embedded length, the specimens without anodic polarization show the failure by slippage of the whole carbon yarn, while the slippage-partial rupture of the carbon yarn can be seen for the specimens with anodic polarization. With increasing  $\alpha$ , the partial rupture of the carbon yarn is more pronounced. The partial rupture of the carbon yarn for MFRCM composites with 30 mm embedded length is due to the polarization induced degradation, and the pullout behavior of the specimens is still controlled by the bond property at the interface between the outer part and the matrix.

Following the same procedure described previously, the bond parameters required to define the bond slip relationship for the outer interface can be evaluated. The bond parameters for defining the bond slip relationship for the outer interface for the MFRCM composites without anodic polarization are tabulated in Table 5.2.

Table 5.2 Bond parameters for the outer and inner interfaces for the MFRCM composites without anodic polarization

Specimen	Outer interface				Inner interface	
	$k_1$ (N/mm <sup>3</sup> )	$k_2$ (N/mm <sup>3</sup> )	$\tau_{max}$ (MPa)	$\tau_0$ (MPa)	$k_{in}$ (N/mm <sup>3</sup> )	$\tau_{in,max}$ (MPa)
M35	66.07	1.49	1.46	0.76	0.11	0.63
M35C	56.75	3.15	1.72	0.89	0.14	0.68

Fig. 5.4 shows, as an example, the evaluated bond slip relationship for the outer interface for the M35 composites polarized over 45 days. As can be seen, anodic polarization has a significant influence on the bond slip relationship for the outer interface. With increasing current density, the local bond strength and the residual bond stress experience a reduction, while there is a marginal effect on the slope of both the ascending and descending portions of the bond slip relationship. To explicate the effects of anodic polarization on the bond behavior

of the outer interface is equivalent to explicate the effects of anodic polarization on the local bond strength and the residual bond stress.

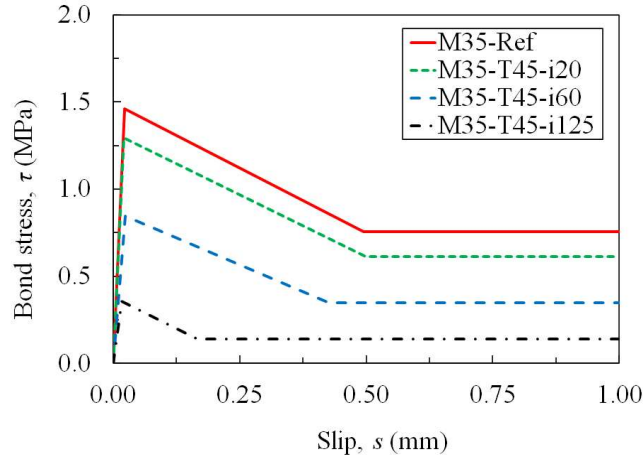


Fig. 5.4 The evaluated bond slip relationship for the outer interface for M35 composites polarized over 45 days

The effects can be expressed in terms of two influence factors,  $\beta_{\tau_{max}}$  and  $\beta_{\tau_0}$  (Eq. (5.5) and Eq. (5.6)), corresponding to the changes in the local bond strength and the residual bond stress, respectively.

$$\beta_{\tau_{max}}(\alpha) = \frac{\tau_{max}(\alpha)}{\tau_{max}(\alpha=0)} \quad (5.5)$$

$$\beta_{\tau_0}(\alpha) = \frac{\tau_0(\alpha)}{\tau_0(\alpha=0)} \quad (5.6)$$

Where  $\tau_{max}(\alpha)$  and  $\tau_0(\alpha)$  denote the local bond strength and the residual bond stress for the MFRCM composites polarized with a certain level of  $\alpha$ , respectively; and  $\tau_{max}(\alpha=0)$  and  $\tau_0(\alpha=0)$  denote the local bond strength and the residual bond stress for the MFRCM composites without anodic polarization, respectively, which has been given in Table 5.2.

Fig. 5.5 and Fig. 5.6 show the effect of  $\alpha$  on the local bond strength and the residual bond stress for the MFRCM composites without and with short carbon fibers. The results show that as  $\alpha$  increases, both  $\beta_{\tau_{max}}$  and  $\beta_{\tau_0}$  show a reduction. It was found that rational functions can lead to the good fitting of the variations in  $\beta_{\tau_{max}}$  and  $\beta_{\tau_0}$ . Eq. (5.7) can be found to give a good fitting of  $\beta_{\tau_{max}}$  for the MFRCM composites without and with short carbon fibers, and the respective value of  $R$  is 0.90 and 0.92. Eq. (5.8) can be found to give a good fitting of  $\beta_{\tau_0}$  for the MFRCM composites without and with short carbon fibers, and the respective value of  $R$  is 0.85 and 0.89. The experimental and fitting results of  $\beta_{\tau_{max}}$  and  $\beta_{\tau_0}$  are presented in Fig. 5.5 and Fig. 5.6. Therefore, the bond slip relationship of the outer interface for MFRCM composites subjected to anodic polarization can be calculated according to Table 5.2 and Eq. (5.7-8).

$$\beta_{\tau_{max}}(\alpha) = \begin{cases} \frac{0.165}{0.165 + \alpha} & \text{for M35 FRCM composites} \\ \frac{0.131}{0.131 + \alpha} & \text{for M35C FRCM composites} \end{cases} \quad (5.7)$$

$$\beta_{\tau_0}(\alpha) = \begin{cases} \frac{0.135}{0.135 + \alpha} & \text{for M35 FRCM composites} \\ \frac{0.081}{0.081 + \alpha} & \text{for M35C FRCM composites} \end{cases} \quad (5.8)$$

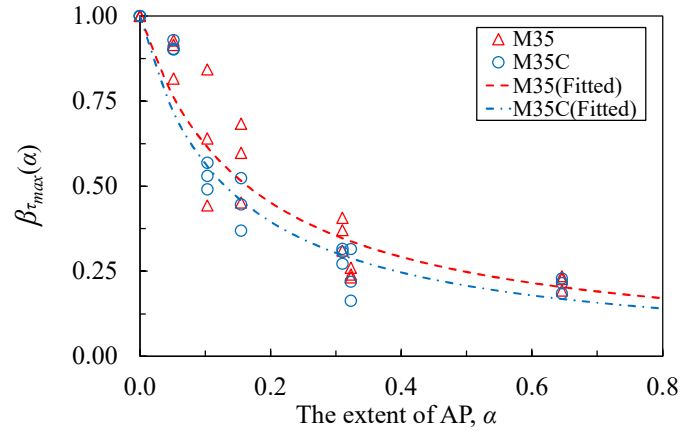


Fig. 5.5 The effect of  $\alpha$  on the local bond strength for the outer interface

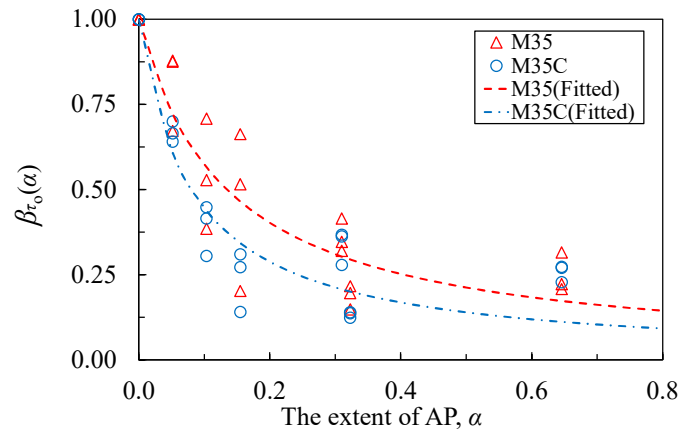


Fig. 5.6 The effect of  $\alpha$  on the residual bond strength for the outer interface

#### 5.3.4 Effects of anodic polarization on bond slip relationship for the inner interface

As described previously, the slippage-partial rupture of the embedded carbon yarn can be seen for pullout specimens with 50 mm embedded length. Specifically, such failure is featured by the slippage of the inner part and the breakage of the outer part during the pullout process. Hence, the bond behavior of the inner interface dominates the pullout behavior of the specimens after the breakage of the outer part occurs. Thus, the pullout curve after the breakage of the outer part can be used to evaluate the bond slip relationship for the inner interface. After anodic polarization, the percentage of the inner part pulled out of the matrix was reduced, as the filaments subjected to significant degradation caused by anodic polarization would be left in

the matrix. The variations in the cross-sectional area caused by anodic polarization were addressed previously. Afterwards, the bond slip relationship for the inner interface was evaluated using the same procedure described previously. Table 5.2 presents the bond parameters for the inner interface for the MFRCM composites without anodic polarization.

Fig. 5.7 shows, as an example, the evaluated bond slip relationship for the inner interface for M35 composites polarized over 45 days. With increasing current density, the local bond strength decreases, while there is a marginal effect on the slope of the descending portion of the bond slip relationship.

The effect of anodic polarization on the inner interface can be represented by the effect of anodic polarization on the local bond strength, which can be expressed by an influencing factor,  $\beta_{\tau_{in,max}}$  (Eq. (5.9)), corresponding to the changes in the local bond strength.

$$\beta_{\tau_{in,max}}(\alpha) = \frac{\tau_{in,max}(\alpha)}{\tau_{in,max}(\alpha=0)} \quad (5.9)$$

Where  $\tau_{in,max}(\alpha)$  equals the local bond strength for the MFRCM composites polarized with a certain extent of  $\alpha$ ; and  $\tau_{in,max}(\alpha=0)$  denotes the local bond strength for the MFRCM composites without anodic polarization, which has been given in Table 5.2.

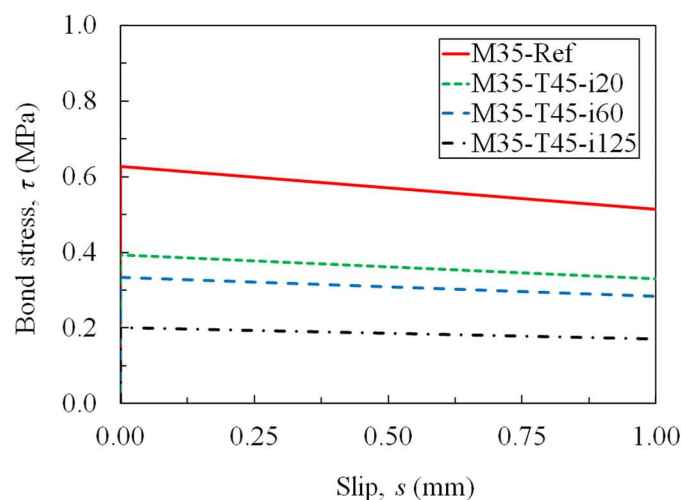


Fig. 5.7 The evaluated bond slip relationship of the inner interface for M35 composites polarized over 45 days

Fig. 5.8 shows the effect of  $\alpha$  on the local bond strength for the inner interface for MFRCM composites without and with short carbon fibers. The results show that as  $\alpha$  increases,  $\beta_{\tau_{in,max}}$  is decreased. Eq. (5.10) can be found to give a good fitting of  $\beta_{\tau_{in,max}}$  for the MFRCM composites without and with short carbon fibers, and the value of R is 0.88. Therefore, the bond slip relationship of the inner interface for the MFRCM composites subjected to anodic polarization can be calculated according to Table 5.2 and Eq. (5.10).

$$\beta_{\tau_{in,max}}(\alpha) = \frac{0.132}{0.132 + \alpha} \quad (5.10)$$

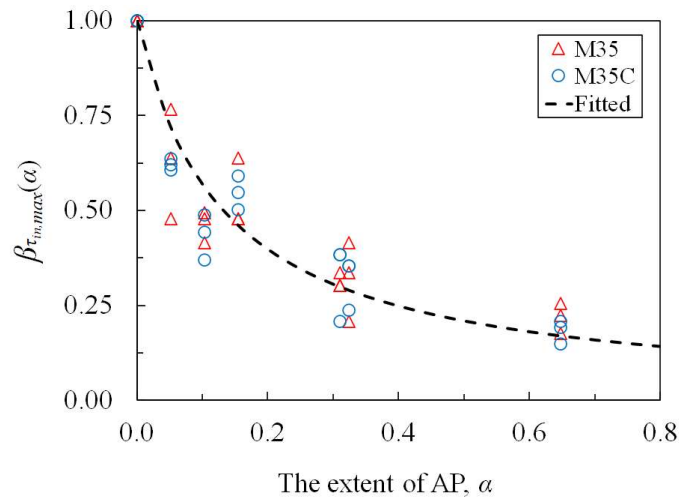


Fig. 5.8 The effect of  $\alpha$  on the local bond strength for the inner interface

#### 5.4 Conclusions of this chapter

Based on the test results and analyses, the following conclusions can be drawn in this chapter.

It can be seen from pullout tests that for MFRCM composites without anodic polarization, the specimens with 30 mm embedded length failed by the slippage of the whole carbon yarn, while the slippage-partial rupture of the carbon yarn was exhibited by the specimens with 50 mm and 70 m embedded length. With introducing anodic polarization, all the pullout specimens showed the failure featured by the slippage-partial rupture of the carbon yarn. With increasing current density, the peak applied force and the residual force decrease.

With increasing the extent of anodic polarization, the cross-sectional area for the carbon yarn within the MFRCM composites decreases. For a small extent of anodic polarization, the sectional area for the outer part is decreased, while no reduction is seen for the inner part. After reaching a certain extent of anodic polarization, the cross-section of the inner part starts to decrease.

The bond slip relationship for the outer and inner interface can be evaluated for the MFRCM composites based on the pullout curves. The results show that anodic polarization has a noticeable effect on the bond slip relationship for the outer and inner interface. As the current density is increased, the bond slip relationship for both interfaces is compromised. In particular, the local bond strength and the residual bond stress are reduced by anodic polarization for the outer interface, while it is the local bond strength decreased for the inner interface. Further, these bond parameters were correlated with the extent of anodic polarization to express the effect of anodic polarization on the bond behavior between carbon fabric and cementitious matrix.

## Chapter 6

### 6 Summary and suggestions

#### 6.1 Summary

The thesis presents systematic research aimed at clarifying the bond behavior between carbon fabric and cementitious matrix within the MFRCM composites under anodic polarization. The major findings obtained from the present research are as follows.

(1) The bond behavior of carbon yarn embedded in a range of cementitious matrices has been identified. The trilinear bond slip relationship was assumed and determined by comparing the analytical  $P\sim u$  curve with the experimental results. With the evaluated bond slip relationship, the effect of matrix type on the bond behavior between carbon yarn and cementitious matrix can be indicated. The results suggest similar bond behavior of the carbon yarn embedded in various matrices. The applied force versus displacement curve can be numerically predicted for different bond lengths using the evaluated bond slip relationship, and the critical embedment length required to reach the tensile strength of the carbon yarn can be determined. Further, an approach that can be used to calculate the critical embedment length has been established, providing a good prediction that fits well with the numerical results.

(2) The bond between carbon fabric and the matrix is influenced and complicated by the limited matrix impregnation. The filaments within a single carbon yarn can be grouped into two parts, namely the outer part and the inner part, and two interfaces be defined, including the outer interface between the matrix and the outer part and the inner interface between the outer part and the inner part. Based on the image processing and analysis results, the percentage of the outer part is estimated at around 30% of the whole carbon yarn. A method has been proposed to determine the bond slip relationship for the outer and inner interface based on pullout test results. FE modeling with the obtained bond slip relationships can provide good agreement with experimental results in terms of the failure mechanisms and the pullout response curve. With FE modeling, the stress transfer at the outer and inner interfaces and the contribution of the outer and inner parts to carrying the applied force can also be clarified. In addition, the effects of matrix impregnation, strength factor and embedded length have been discussed through a parametric study.

(3) The electrochemical performance of MFRCM composites during anodic polarization has been established in terms of applied current, cell voltage and the instant-off anodic potential. Stabilized electrochemical performance can be maintained for the MFRCM composites polarized at a current density no more than  $125 \text{ mA/m}^2$  for 90 days, while an exponential increase can be seen in the measured cell voltage for larger current densities. The service life defined as the time at which the exponential increase in the cell voltage initiates is reduced with increasing the current densities. Furthermore, the charge density at service life is found to be almost the same for the MFRCM composites polarized at different current densities.

(4) The mechanisms of degradation have been identified for the MFRCM composites under anodic polarization by means of SEM, EDS, FTIR and XPS. For the matrix in the vicinity of carbon fabric after anodic polarization, no significant change was detected in terms of calcium distribution regardless of current density. While for the carbon fabric in the polarized MFRCM

composites, severe degradation occurred on the carbon fabric, which was featured by multiple transverse cracks on the carbon filaments. In the case of a large current density, the carbon filaments can even be intercepted or scaled. Besides, the chemical composition of carbon fabric is also affected by anodic polarization. Based on these characterization results, possible electrochemical reactions and propagation of the reactions have been discussed to reach a better understanding of the mechanisms of degradation for the MFRCM composites under anodic polarization.

(5) Anodic polarization harms the carbon fabric-cementitious matrix system. The cross-sectional area of the outer and inner part within an embedded carbon yarn is reduced due to polarization induced degradation. The relationship between the changes in the sectional area and the extent of anodic polarization has been established to explicate the degradation of the carbon fabric caused by polarization. Besides, the respective bond slip relationship for the outer and inner interface has also been obtained for the MFRCM composites subjected to anodic polarization. There is a significant degradation in the bond behavior of the outer and inner interface. The relationship between the bond slip relationship and the extent of anodic polarization has been established for the outer and inner interface.

## **6.2 Suggestions for future works**

Based on the major outcomes of the present study, some suggestions are given below.

(1) The influence of matrix impregnation on the bond behavior between carbon fabric and the cementitious matrix has been investigated. The non-uniform matrix impregnation leads to progressive failure of the outer part and the slippage of the inner part. Thus, it is useful to develop some measures to increase the matrix impregnation and subsequently to improve the corresponding bond behavior of the carbon fabric-cementitious matrix system.

(2) Carbon fabric exhibited severe deterioration for the MFRCM composites subjected to anodic polarization. To increase the resistance of the carbon fabric to polarization induced degradation is meaningful for improving the sustainable performance of the ICCP-SS method. Thus, future research should take into consideration the improvement of the carbon fabric for the MFRCM composites. In addition to deterioration of carbon fabric in MFRCM composites with anodic polarization, it is also likely to encounter other degradation phenomena, such as anodic acidification between carbon fiber and matrix, which also requires further clarification.

(3) Since the deficient concrete structures that ICCP-SS would apply to are possibly caused by chloride contamination, the presence of chloride is an important issue, as it may affect the efficiency of ICCP, degradation mechanisms of carbon fabric and the corresponding bond and mechanical behavior of the MFRCM composite. Therefore, the presence of chloride should be considered in future studies.

(4) Although the bond behavior has been investigated for the MFRCM composites after anodic polarization, the interaction between the anodic polarization and the external force is not yet addressed. In reality, the composites are supposed to be subjected to the anodic polarization and the external force at the same time. Thus, further investigations should be performed on this interaction.

(5) The bond between carbon fabric and cementitious matrix within the MFRCM composites has been studied in the present study with the purpose of not only characterizing the stress transfer in the fabric-matrix systems but also providing the fundamental knowledge to understand the global mechanical behavior of the composites and the corresponding strengthening systems. The upscale application of the bond behavior between carbon fabric and matrix in modeling the mechanical behavior of the composites and the corresponding strengthening systems would be hopefully considered in the future. Further, based on the good understanding of MFRCM composites and the corresponding strengthened structures, future studies are also needed to investigate how to predict the life cycle of structures with ICCP-SS.



# Appendix

## 7 Appendix A

### 7.1 Introduction

This appendix presents a generalized method to assess the bond behavior between externally bonded FRP and substrate concrete. The method is also capable of predicting the bond strength, FRP strain distribution along the FRP-concrete interface and effective bond length. In comparison to the existing methods of determining the bond slip relationship for the interface, the advantage of the proposed method lies in obtaining the bond slip relationship based on the global mechanical behavior of the interface while there is no need to presume the detailed configuration of the relationship. Following the proposed methodology, the global applied force versus displacement (namely the loaded end slip) can be derived for any given bond slip relationship, which was used to derive Eq. (3.4) in Chapter 3.

The theorem of the proposed method to determine the bond slip relationship was first explained in the appendix. Then, the formulae were derived to predict the bond strength, strain distribution and effective bond length. Based on the assumption of the linear strain distribution along the FRP-concrete interface, the calculation of the effective bond length can be easily conducted based on the global force versus displacement curve. A referenced FRP-concrete interface reported in the existing literature (Yao 2014) was used as an example to illustrate the detailed implementation of the proposed method. Further, a comparison of the effective bond length predicted from Chen and Teng's model (2001), the analytical approach and the proposed method was carried out to validate the reliability of the proposed method.

### 7.2 Generalized evaluation of bond behavior between FRP and concrete

#### 7.2.1 Determination of $\tau$ - $s$ relationship using the $P$ - $u$ curve

Single shear bond test (single lap shear test or pull off test) has been widely used to investigate the bond at the FRP-concrete interface. The typical setup for the single shear test is shown in Fig. A.1. FRP is normally applied onto concrete surface with epoxy resin and subjected to tension force.

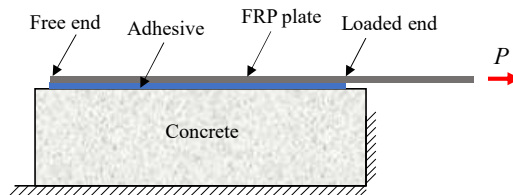


Fig. A.1 Test setup for single shear tests

The interfacial governing equation can be formulated according to the force equilibrium, compatibility condition and material behavior when analyzing a small fragment  $dx$  of the FRP. The. A second-order differential equation has been normally proposed to express the interfacial governing equation, see Eq. (A.1). Though some variations may exist in the interfacial equations for different studies, the equations can be simplified to be close to Eq. (A.1).

$$\frac{d^2s(x)}{dx^2} = \frac{1}{E_f t_f} \tau(s) \quad (\text{A.1})$$

Where  $s$  denotes the slip of FRP relative to substrate concrete, which is equal to the difference of displacement between FRP and concrete;  $E_f$  means Young's modulus of FRP;  $t_f$  means the thickness of FRP; and  $\tau(s)$  indicates the relationship between bond stress and slip, i.e. the bond stress slip relationship.

As strain equals the first-order derivative of  $s$  for the externally bonded FRP, the following equation can be established.

$$\frac{d}{dx} \varepsilon(x)^2 = \frac{d}{dx} \left( \frac{ds(x)}{dx} \right)^2 = 2 \frac{ds(x)}{dx} \frac{d^2s(x)}{dx^2} \quad (\text{A.2})$$

The order of interfacial governing equations can be reduced by substituting Inserting Eq. (A.2) into Eq. (A.1). Thus, one can have

$$\frac{d}{dx} \varepsilon(x)^2 = \frac{2s'(x)}{E_f t_f} \tau(s) \quad (\text{A.3})$$

It should be noted that the proposed method applies to the case that FRP has a sufficiently long bond length, which means the slip and strain at the free end of FRP are both equal to zero. By introducing the zero slip and zero strain at the free end, integrating both sides of Eq. (A.3) over the bond length yields

$$\int_0^L \frac{d}{dx} \varepsilon(x)^2 dx = \int_0^L \frac{2s'(x)}{E_f t_f} \tau(s) dx = \int_0^u \frac{2}{E_f t_f} \tau(s) ds \quad (\text{A.4})$$

Where  $L$  equals the FRP's bond length and  $u$  is the loaded end slip (also termed the global displacement).

Further, Eq. (A.4) can be converted to

$$\varepsilon_L^2(u) = \frac{2}{E_f t_f} \int_0^u \tau(s) ds \quad (\text{A.5})$$

Where  $\varepsilon_L^2$  equals the loaded end strain of FPR.

Taking the first-order derivative of Eq. (A.5) with respect to  $u$ , Eq. (A.6) can be obtained. It can be further converted to Eq. (A.7) by introducing FRP's linear tensile behavior.

$$\varepsilon_L(u) \varepsilon_L'(u) = \frac{1}{E_f t_f} \tau(u) \quad (\text{A.6})$$

$$\tau(u) = \frac{1}{E_f t_f b_f^2} P(u) P'(u) \quad (\text{A.7})$$

Where  $P(u) = E_f t_f b_f \varepsilon_L(u)$ , which is the global force.

Eq. (A.7) can be expanded by replacing the derivate with difference quotient, see Eq. (A.8).

$$\tau(u_i) = \frac{1}{E_f t_f b_f^2} P(u_i) \frac{P(u_i) - P(u_{i-1})}{u_i - u_{i-1}} = \tau(s_i) \quad (\text{A.8})$$

Therefore, the relationship between the bond slip relationship and the global force versus displacement can be established by Eq. (A.8). It can be seen that the bond slip relationship can be determined directly based on the proposed based on the global force versus displacement. The obtained bond slip relationship is more generalized since no assumption on the shape of the relationship is presumed. Although  $u$  in Eq. (A.7) (or  $u_i$  in Eq. (A.8)) means the global displacement,  $\tau(u)$  or  $\tau(u_i)$  corresponds to the local bond behavior.

### 7.2.2 Prediction of the bond strength model

The integral of the bond slip relationship over an interval  $[0, u]$  is defined as  $I(u)$ , see Eq. (A.9).

$$I(u) = \int_0^u \tau(s) ds \quad (\text{A.9})$$

Eq. (A.10) can be obtained by using the finite difference method.

$$I(u) = \int_0^u \tau(s) ds = \sum_{i=1}^n \frac{\tau(s_{i-1}) + \tau(s_i)}{2} (s_i - s_{i-1}), s_n = u \quad (\text{A.10})$$

Based on Eq. (A.5) and Eq. (A.9) as well as the FRP's material behavior, Eq. (A.11) can be established.

$$P(u) = b_f \sqrt{2E_f t_f I(u)} \quad (\text{A.11})$$

Therefore, it is able to predict the global force versus displacement curve for any bond slip relationship.

In addition, the bond strength model can be easily derived using Eq. (A.11). Once  $I(u)$  reaches its maximum, the maximum global force (bond strength) can be achieved. The maximum value of  $I(u)$  equals the area underneath the whole bond slip relationship, which is also termed fracture energy,  $G_f$ . Hence, the bond strength model becomes,

$$P_{max} = b_f \sqrt{2E_f t_f G_f} \quad (\text{A.12})$$

Eq. (A.12) is similar to the existing bond strength models where  $G_f$  is used. Bond strength is independent of the shape of the bond slip relationship but dependent on  $G_f$ . It means that bond strength could be the same once  $G_f$  is equal for different relationships, though the shape may differ greatly.

### 7.2.3 Prediction of strain and bond stress distribution

As previously described, the proposed method also covers the prediction of FRP strain distribution along the FRP-concrete interface. Based on Eq. (A.5), the loaded end strain of FRP

can be related to the integral  $I(u)$ . Therefore, When the slip is given at a point along the interface, the corresponding strain can be determined provided a given bond slip relationship.

For the sake of illustration, the global displacement, i.e. the loaded end slip, is taken as  $s_n$ . The bond slip relationship and the bond length are discretized into  $n$  small intervals. Fig. A.2 presents a diagram for determining the strain distribution of the externally bonded reinforcement for any given bond slip relationship.

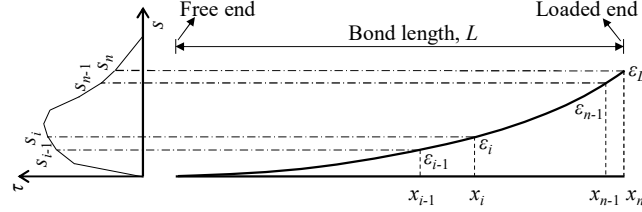


Fig. A.2 Diagram for determining the strain distribution of the externally bonded reinforcement for any bond slip relationship.

According to Eq. (A.5), Eq. (A.13) can be obtained to calculate the strain  $\varepsilon_i$  at the point  $x_i$  where the slip is equal to  $s_i$ .

$$\varepsilon_i^2 = \frac{2}{E_f t_f} \int_0^{s_i} \tau(s) ds \quad (\text{A.13})$$

As can be seen in Fig. A.2, the strain and the slip at any point along the interface can be determined based on Eq. (A.10) and Eq. (A.13). Once the position of each point with the known strain and slip can be determined, the strain distribution can be obtained.

In  $[x_{i-1}, x_i]$ , the slip and strain at the node  $x_i$  are, respectively, represented by  $s_i$  and  $\varepsilon_i$ . Linear distribution in the strain within a small interval can be assumed. Thus, one can have

$$\frac{s_i - s_{i-1}}{\Delta x_i} = \frac{\varepsilon_i + \varepsilon_{i-1}}{2} \quad (\text{A.14})$$

Where  $s_i$  and  $\varepsilon_i$  are the slip and the strain at  $x_i$ , respectively and  $\Delta x_i$  is the interval length.

Combining Eq. (A.10), Eq. (A.13) and Eq. (A.14),  $\Delta x_i$  can be computed by Eq. (A.15) and Eq. (A.16).

$$\Delta x_i = \sqrt{2E_f t_f} \left[ \frac{s_i - s_{i-1}}{\sqrt{I(s_i)} + \sqrt{I(s_{i-1})}} \right] \quad (\text{A.15})$$

$$\Delta x_i = 2\sqrt{2E_f t_f} \left[ \frac{\sqrt{I(s_i)} - \sqrt{I(s_{i-1})}}{\tau(s_i) + \tau(s_{i-1})} \right] \quad (\text{A.16})$$

With the global force versus displacement curve, Eq. (A.15) and Eq. (A.16) can be converted to,

$$\Delta x_i = 2E_f t_f b_f \left[ \frac{u_i - u_{i-1}}{P(u_i) + P(u_{i-1})} \right] \quad (\text{A.17})$$

Since the loaded end slip and the corresponding strain are known, the position  $x_i$  with  $s = s_i$  can be determined through a recursive method starting from the loaded end. Thus, the strain distribution during the entire experiment can be determined by varying the global displacement at the loaded end.

#### 7.2.4 Determination of $L_{eff}$

The proposed method is also capable of determining  $L_{eff}$  based on the global force versus displacement curve. Provided a bond slip relationship,  $s_f$  indicates the post-peak slip at which bond stress is zero or close to zero. For some existing bond slip models, bond stress is impossible to reach exactly zero because they are an asymptotic function, as shown in Table A.1.  $L_{eff}$  can be obtained if the loaded end slip reaches  $s_f$ , indicating the entire course of the bond slip relationship can fully develop along the interface.

when  $u = s_f$ ,  $L_{eff}$  is the sum of the length of  $n$  intervals, see Eq. (A.18).

$$L_{eff} = \sum_{i=1}^n \Delta x_i = 2\sqrt{2E_f t_f} \sum_{i=1}^n \frac{\sqrt{I(s_i)} - \sqrt{I(s_{i-1})}}{\tau(s_i) + \tau(s_{i-1})}, s_n = s_f \quad (\text{A.18})$$

According to Eq. (A.18)  $L_{eff}$  can be related to the bond slip relationship. Provided any bond slip relationship, Eq. (A.18) can be used to determine  $L_{eff}$ .

After reviewing the strain distribution of FRP with the loaded end slip exceeding  $s_f$ , a nearly a centrosymmetric distribution can be found. Once the loaded end slip exceeds  $s_f$ , debonding will initiate and propagate towards the free end. The actual and simplified strain distribution of FRP is shown in Fig A.3. The strain becomes null at the free end due to small slips, while the strain close to the loaded end is almost kept at a certain level, indicating the loss in the bond because of large slips.

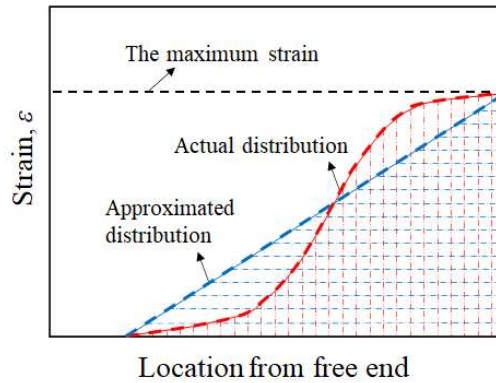


Fig. A.3 Actual and simplified strain distribution of FRP along the interface

When the loaded end slip is equal to  $s_f$ , it can be computed by integrating the strain over the whole bond length. In order words,  $s_f$  equals the area under the strain distribution curve. As the actual strain distribution follows a nearly centrosymmetric shape, the actual area under the

strain distribution curve can be approximated by the area under a linear distribution curve. Thus, Eq. (A.19) can be obtained.

$$s_f = \int_0^{L_{eff}} \frac{1}{L_{eff}} \sqrt{\frac{2G_f}{E_f t_f}} x dx \quad (19)$$

Eq. (A.19) can be rearranged as

$$L_{eff} = s_f \sqrt{\frac{2E_f t_f}{G_f}} \quad (20)$$

It can be seen that  $L_{eff}$  is related to the overall and local properties of the bond slip relationship, namely  $G_f$  and  $s_f$ .

Once determining  $G_f$  using Eq. (A.12) and taking  $s_f$  as the global displacement corresponding to the maximum global force, Eq. (A.20) can be used to calculate  $L_{eff}$  based on the experimental results. Note that the FRP width significantly affects the maximum global force and thus  $G_f$  obtained from Eq. (12) is influenced. However,  $G_f$  does not scale with the FRP width if determining from the strain measurements in the central region of the FRP sheet (Subramaniam et al. 2007; Subramaniam et al. 2011). Thus, when using Eq. (12), the influence of the FRP width on the maximum global force should be excluded, which can be done by introducing the FRP-concrete width ratio (Chen and Teng 2001) or an additional width (Dai et al. 2005).

Eq. (A.21) can be obtained by combining Eq. (A.12) and Eq. (A.20).

$$L_{eff} = \frac{2s_f E_f t_f b_f}{P_{max}} \quad (A.21)$$

Special attention should be paid to determine  $s_f$  from the experimental results, as it greatly influences the calculation of  $L_{eff}$ . In this study,  $s_f$  can be determined by Eq. (A.22) with assuming a bilinear bond slip relationship.

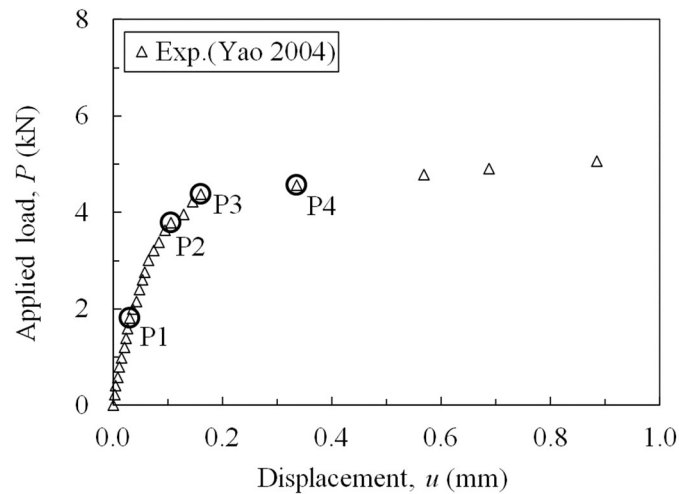
$$s_f = \frac{2G_f}{\tau_{max}} \quad (A.22)$$

Where  $\tau_{max}$  denotes local bond strength obtained from Eq. (A.8).

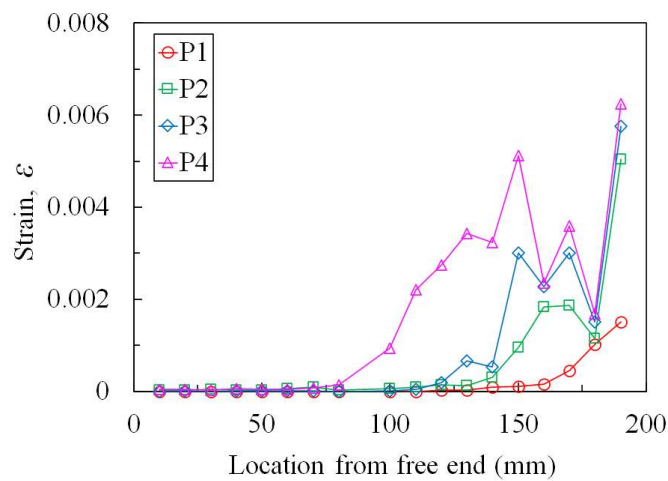
### 7.3 An introductory example of utilizing the proposed method

An FRP-concrete interface reported in the literature is used as an example to illustrate the implementation of the proposed method. The reported FRP interface is documented in (Yao 2004) with the following parameters:  $E_f = 256$  GPa,  $t_f = 0.165$  mm,  $b_f = 25$  mm,  $L = 190$  mm and  $f_c = 29$  MPa. The experimental force versus displacement curve and the strain distribution can be referred to (Yao 2004; Yuan et al. 2004). The effect of the FRP width on the bond strength was excluded using the FRP-concrete width ratio. Then, the applied load and the measured strain were divided by the width factor ( $\beta_w$  in (Chen and Teng 2001)). By doing this, the predicted bond strength will be equal to the experimental result.

The global force versus displacement curve of the referenced joint up to  $u = 0.9$  mm is shown in Fig. A.4b (Yao 2004; Yuan et al. 2004). Fig. A.4b shows the FRP strain distribution at various loading levels (Yao 2004; Yuan et al. 2004). The loading levels indicated by P1, P2, P3 and P4 correspond to the applied forces of 2.26 kN, 4.75 kN, 5.53 kN and 5.74 kN, respectively (Yao 2004; Yuan et al. 2004). For a small loading level, strain decreases with increasing the distance away from the loaded end, which means that the bond is activated from the loaded end to the free end. For a high loading level, the strain descends slowly at the loaded end, indicating the loss in the bond due to debonding.



(a) The global force versus displacement curve



(b) The strain distribution of FRP at different loading levels

Fig. A.4 Experimental results of the referenced FRP-concrete joint in terms of (a) the global force versus displacement curve and (b) the strain distribution of FRP at different loading levels

Table A.1 shows some existing bond slip relationships found in the literature. With the given parameters for the reference interface, different bond slip relationships can be determined for the interface.

Table A.1 Various bond slip models available in the existing literature

Bond slip relationship	Expression	Bond parameters
Nakaba et al. (2001)	$\frac{\tau}{\tau_{max}} = \frac{s}{s_{max}} \frac{n}{n-1 + (s/s_{max})^n}$	$\tau_{max} = 3.5f_c^{0.19}$ $n = 3$ $s_{max} = 0.065 \text{ mm}$
Sato et al. (2000)	$\tau = \frac{\tau_{max}}{s_{max}} G_0 D^* s, s \leq s_{max}$ $\tau = \tau_{max} e^{-10(s-s_{max})}, s > s_{max}$	$G_0 = 1 + \frac{25500}{E_f t_f}, E_f t_f \geq 38.4 \text{ GPa} \cdot \text{mm}$ $\tau_{max} = 9.1 f_c^{0.2} E_f t_f \times 10^{-5} \leq 3.49 f_c^{0.2}$ $D^* = 1 - e^{\alpha(s/s_{max})^{-\beta}}$ $\alpha = \ln\left(1 - \frac{1}{G_0}\right)$ $\beta = 0.2665 (E_f t_f)^{0.083} \leq 0.64$
Guo et al. (2005)	$\frac{\tau}{\tau_{max}} = 1.114 \left(\frac{s}{s_{max}}\right)^{0.488}, s \leq s_{max}$ $\frac{\tau}{\tau_{max}} = 1.3424 e^{-0.2578s/s_{max}}, s > s_{max}$	$\tau_{max} = 0.7512 f_c^{0.5}$
Savoia et al. (2003)	$\tau = \tau_{max} \frac{s}{s_{max}} \frac{2.86}{1.86 + (s/s_{max})^{2.86}}$	$\tau_{max} = 3.5 f_c^{0.19}$ $s_{max} = 0.051 \text{ mm}$
Dai et al. (2005)	$\tau = 2B G_f (e^{-Bs} - e^{-2Bs})$	$G_f = 0.446 \left(\frac{G_a}{t_a}\right)^{-0.352} (E_f t_f)^{0.023}$ $B = 6.846 (E_f t_f)^{0.108} \left(\frac{G_a}{t_a}\right)^{0.833}$
Lu et al. (2005)	$\tau = \tau_{max} \sqrt{\frac{s}{s_{max}}}, s \leq s_{max}$ $\tau = \tau_{max} e^{-\alpha(s/s_{max}-1)}, s > s_{max}$	$s_{max} = 0.0195 \beta_w f_t$ $G_f = 0.308 \beta_w^2 \sqrt{f_t}$ $\beta_w = \sqrt{\frac{2.25 - b_f/b_c}{1.25 + b_f/b_c}}$ $\alpha = \frac{1}{\frac{G_f}{\tau_{max} s_{max}} - 2/3}$

Note:  $f_c$  = the compressive strength of the substrate concrete;  $G_a$  = the shear modulus of the adhesive;  $t_a$  = the thickness of the adhesive;  $f_t$  = the tensile strength of the substrate concrete;  $b_c$  = the width of the substrate concrete.

Fig. A.5 compares the different bond slip relationships for the same interface. These relationships have a similar overall tendency, including an ascending and a descending branch.



Even though, the relationships differ in local behavior, like the slope of the ascending and descending branches, the local bond strength and the corresponding slip and  $s_f$ .

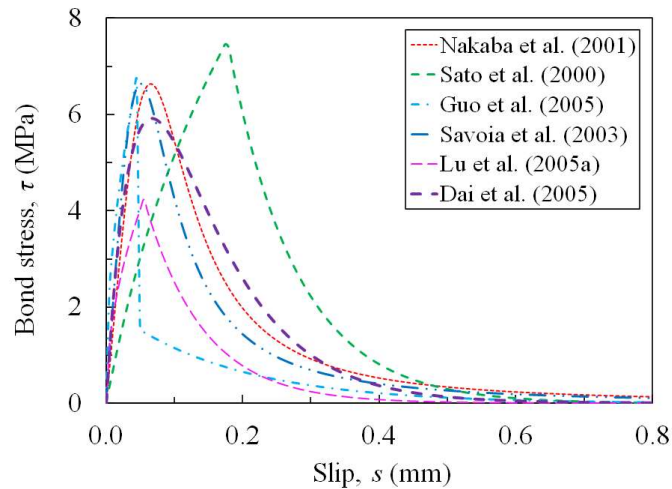


Fig. A.5 Comparison between various bond slip relationships.

Fig. A.6 shows a comparison of the global force versus displacement curve between experiments and predictions with various bond slip relationships shown in Fig. A.5. Lu et al.'s model (Lu et al. 2005) and Guo et al.'s model (Guo et al. 2005) lead to close prediction, while other models overestimate the experimental results. As for Lu et al.'s model (Lu et al. 2005), there is a clear difference between the experimental and predicted curve for large displacements. Whilst Guo et al.'s model (Guo et al. 2005) leads to the prediction that shows deviation from the initial increasing part of the experimental curve. Thus, none of the existing bond slip relationships provides accurate predictions of the experimental results.

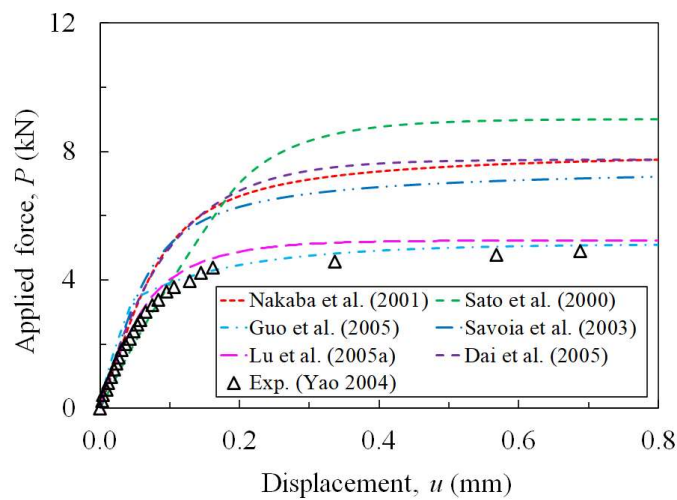


Fig. A.6 Comparison between the experimental global force versus displacement curve and predictions using various bond slip relationships shown in Fig. A.5

Based on the proposed method, the generalized bond slip relationship can be obtained from the experimental global force versus displacement curve. The experimental curve was discretized into small intervals and the number of small intervals is herein taken as 200. Data treatment without significant alteration may be needed to increase the quality of the experimental results, like data smoothing. Then, the bond slip relationship can be obtained by Eq. (A.8).

Fig. A.7 presents a comparison between various modified bond slip relationships. The proposed relationship marked by the black dotted line in Fig. A.7 is obtained from Eq. (A.8). It should be noted that there is an inflection point in the descending part of the proposed relationship. This is because the slope of the global force versus displacement curve at about  $u = 0.2$  mm (as shown in Fig. A.4) decreases significantly and cause the inflection point to appear. Besides, the proposed relationship was further simplified to a bilinear relationship based on the equivalent bond strength. The local bond strength and the corresponding slip are the same between the proposed and bilinear relationship and  $s_f$  can also be obtained from Eq. (A.22). The existing bond slip relationships were also modified and included in this analysis. To maintain the specific shape of these relationships, an adjustment coefficient was used to multiply the bond stress until the  $G_f$  leads to the predicted bond strength equal to the experimental results. Although  $G_f$  is the same for different bond slip relationships, the relationships exhibit a significant difference. In comparison to the proposed relationship, Guo et al.'s model (Guo et al. 2005) provides the highest local bond strength, while Sato et al.'s model (Sato et al. 2000), Nakaba et al.'s model (Nakaba et al. 2001) and Dai et al.'s model (Dai et al. 2005) underestimate the local bond strength.

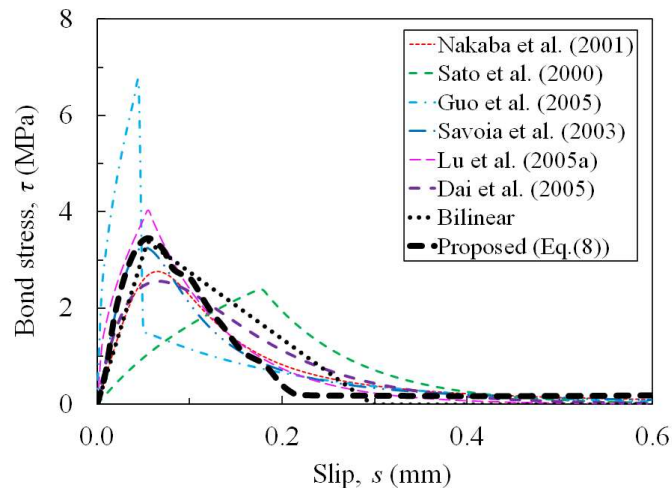


Fig. A.7 Comparison between various modified bond slip relationships and the two relationships obtained from the proposed method

The experimental global force versus displacement curve and predictions using the bond slip relationships shown in Fig. A.7 are presented in Fig. A.8. All the existing bond slip relationships provide the equal maximum global force, as they had the same  $G_f$ . Savoia et al.'s model (Savoia et al. 2003) results in good predictions since it is close to the proposed relationship. There are clear differences between the experimental and predicted results for other relationships. There is no doubt that the proposed relationship leads to a perfect prediction as it can be seen as a back-calculation process when using the proposed relationship.

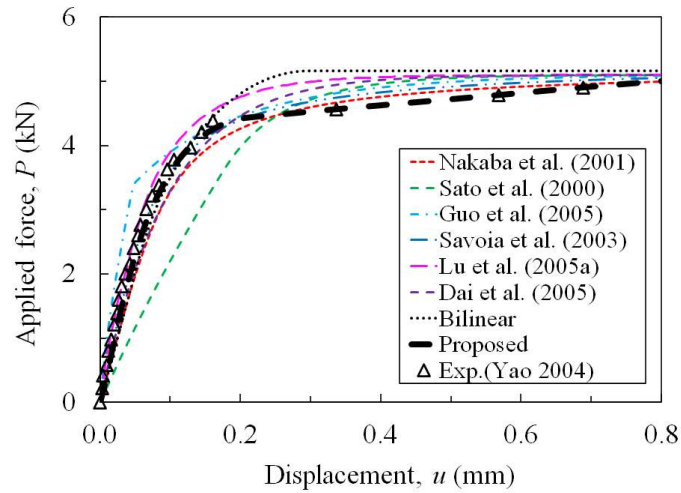
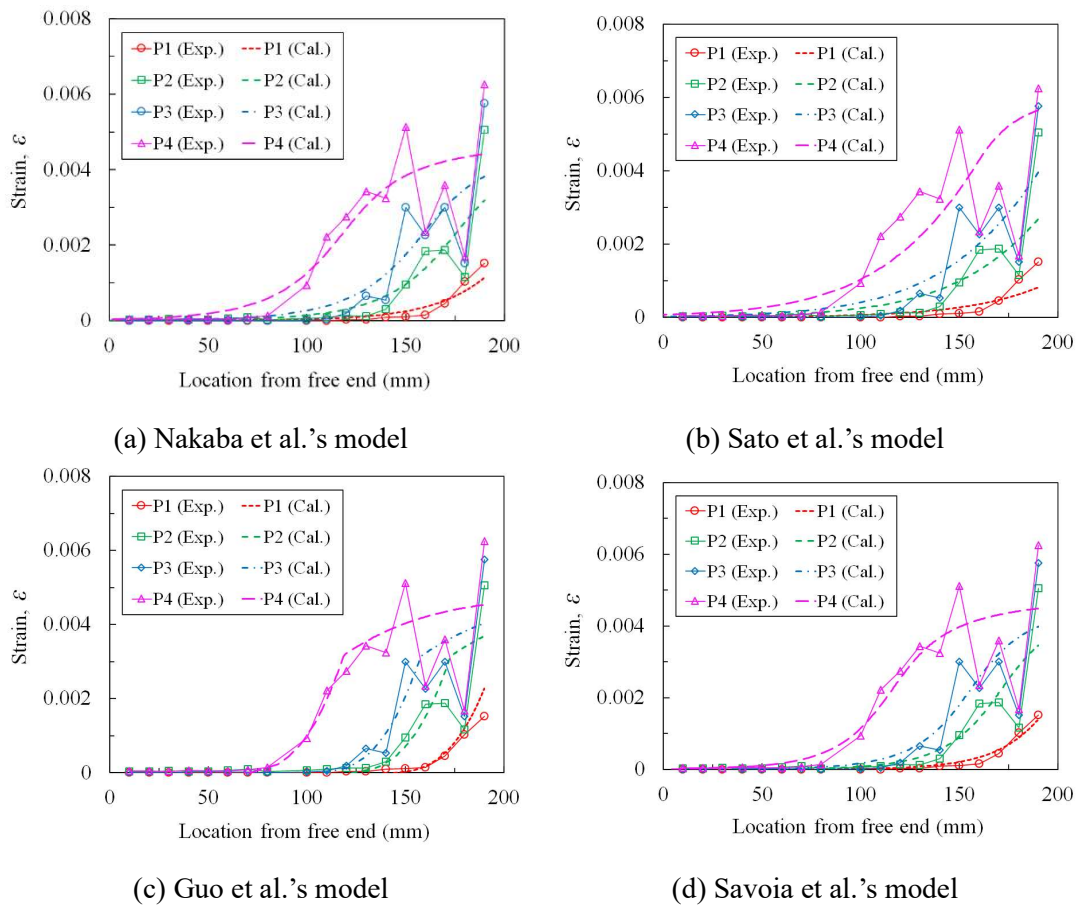


Fig. A.8 Comparison between the experimental global force versus displacement curve and predictions with various bond slip relationships in Fig. A.7

In addition, various bond slip relationships shown in Fig. A.7 were used to derive the strain distribution of FRP at various loading levels. Fig. A.9 presents a comparison of the strain distribution obtained from the experiment and predictions with various bond slip relationships. The comparison shows that all relationships lead to prediction in reasonable agreement with the experimental results.



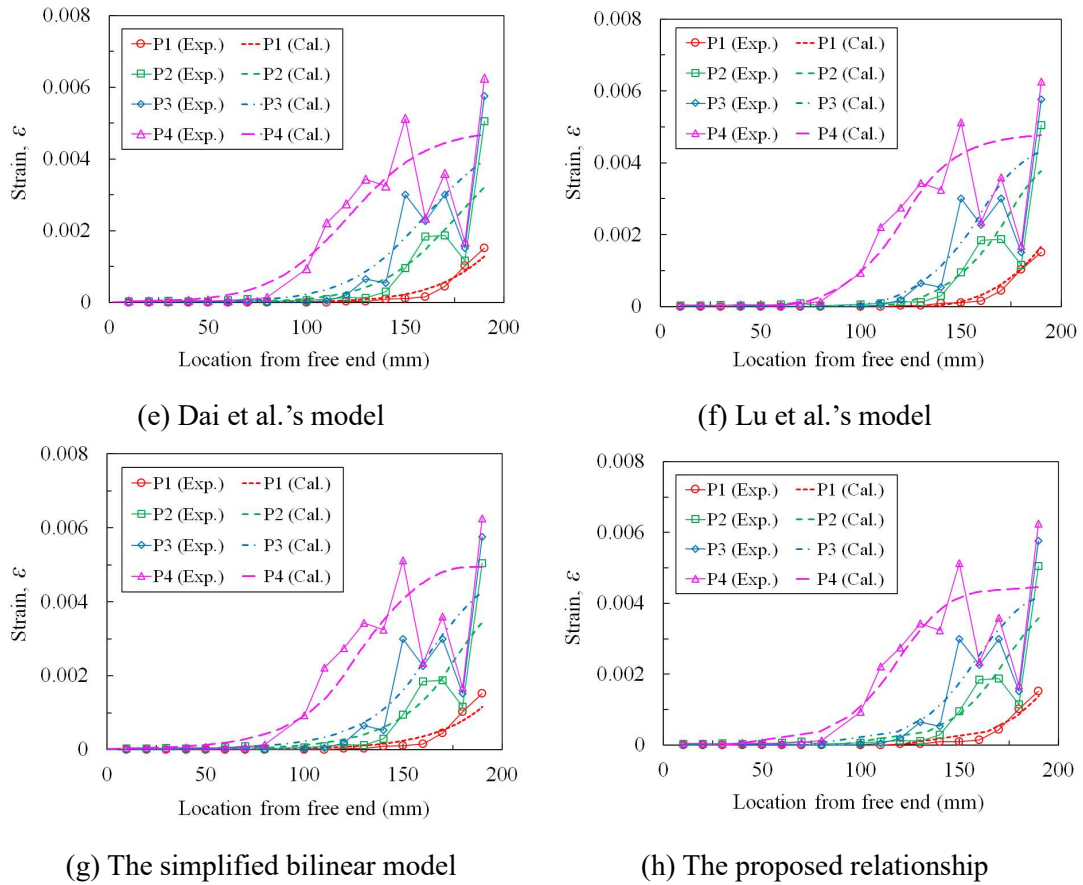


Fig. A.9. Comparison between the measured strain distribution and the predicted results using various bond slip models in Fig. A.7

After obtaining strain distribution, bond stress distribution can also be determined along the interface. The bond stress distribution along the referenced interface at loading level P4 for various bond slip relationships is presented in Fig. A.10. The results show that all the relationships fully develop along a limited length along the interface except Sato's model (Sato et al. 2000). This limited length is equivalent to  $L_{eff}$ . Therefore, the obtained bond stress distributions differ greatly for various bond slip relationships, but  $L_{eff}$  is similar except for Sato et al.'s model (Sato et al. 2000).

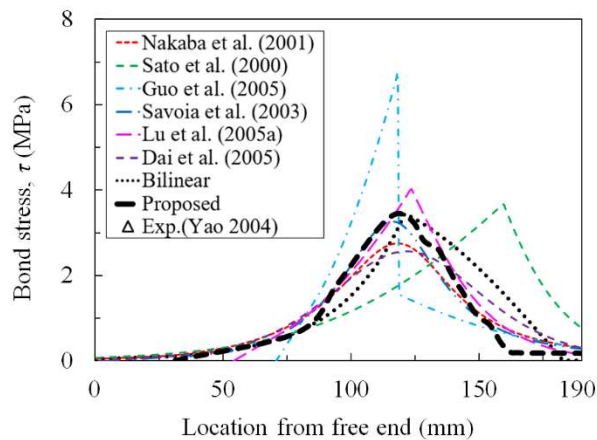


Fig. A.10 Bond stress distribution for various bond slip relationships of the referenced interface at the loading level P4

#### 7.4 Verification of the proposed method to calculate $L_{eff}$

The reliability of the proposed method to calculate  $L_{eff}$  is verified. Yao (2004) investigated the effect of bond length on bond strength. The full range behavior of the interfaces was analyzed with assuming a bilinear bond slip relationship. The bond parameters required to define the bilinear relationship were given for the interfaces. The slip  $s_f$  was taken as the average value obtained for the interfaces with long bond lengths (over 100 mm). As the accuracy of Chen and Teng's model (Chen and Teng 2001) has been demonstrated, it can be used to calculate  $L_{eff}$ . Fig. A.11 compares  $L_{eff}$  obtained from the experiments (Yao 2004), the proposed method and Chen and Teng's model. It can be seen that  $L_{eff}$  calculated by the proposed method and Chen and Teng's model are in good agreement with the experimental results.

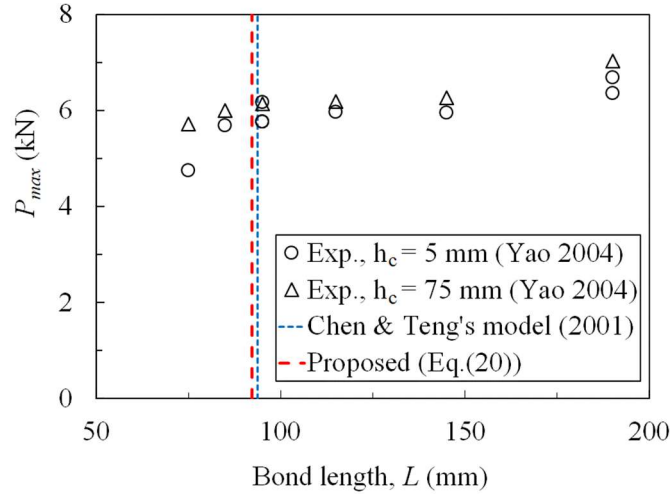


Fig. A.11 Comparison of  $L_{eff}$  obtained from experiments, Chen and Teng's model and the proposed method

Besides, to accurately calculate  $L_{eff}$ , a formula incorporating bond parameters (Dai et al. 2005) was given in Eq. (A.23).

$$L_{eff} = \frac{\sqrt{2E_f t_f}}{B\sqrt{G_f}} \ln\left(\frac{1+\alpha}{1-\alpha}\right) \quad (A.23)$$

where  $G_f$  and  $B$  are the fracture energy and the ductility index, respectively, and  $\alpha$  denotes the percentage of the theoretical bond strength that  $L_{eff}$  can bear.

According to Eq. (23),  $L_{eff}$  increases with increasing  $\alpha$ . Since a longer length than  $L_{eff}$  cannot efficiently increase the bond strength, a value of 0.96 is suggested for  $\alpha$  in (Dai et al. 2006). While  $L_{eff}$  is defined as the length so that 0.97 of the theoretical bond strength can be attained (Yuan et al. 2001).  $\alpha$  ranged from 0.96 to 0.99 was considered to discuss its effect on  $L_{eff}$ . As the bond slip relationship has been reported for all the specimens (Dai et al. 2005), it is easy to calculate  $L_{eff}$  according to Dai et al.'s method (Eq. (23)) and the proposed method. Fig. A.12 compares  $L_{eff}$  obtained from Dai et al.'s method and the proposed method. Good agreement in the predicted  $L_{eff}$  can be achieved for these two methods in the case of  $\alpha$  ranged from 0.96 to 0.98. For  $\alpha = 0.99$ , the calculated  $L_{eff}$  is 32% higher for Dai et al.'s method than the proposed method. According to Eq. (21), the calculated  $L_{eff}$  is only 3% larger for  $\alpha = 0.99$  than  $\alpha = 0.96$ , while it becomes 29% for Dai et al.'s method. This is because the calculated  $L_{eff}$  by Eq. (23) is

larger when  $\alpha$  becomes higher. The calculated  $L_{eff}$  is less sensitive to the value of  $\alpha$  for the proposed method, see Fig. A.12. Thus, the proposed method consisting of Eq. (8), Eq. (21) and Eq. (22) can be used to calculate  $L_{eff}$  using the experimental global force versus displacement curve.

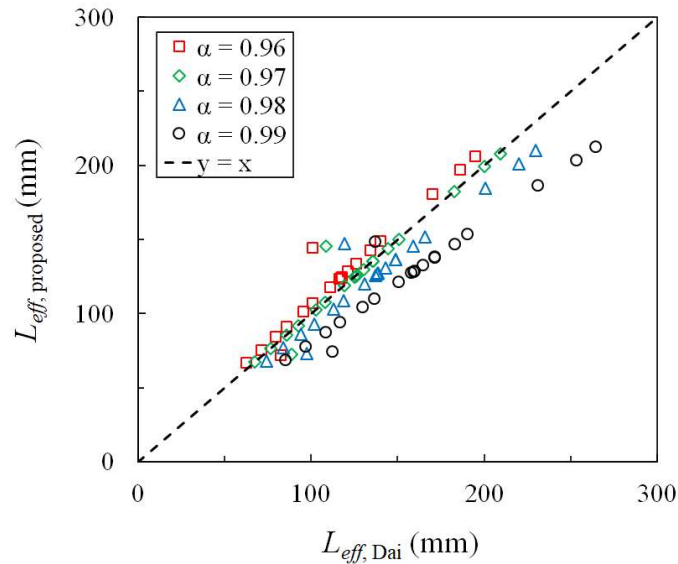


Fig. A.12 Comparison of  $L_{eff}$  obtained from Dai et al.'s method and the proposed method

### Symbols

$b_f$ : the width of FRP;

$E_f$ : Young's modulus of FRP;

$f_c$ : the compressive strength of concrete;

$f_t$ : the tensile strength of concrete;

$G_f$ : the fracture energy;

$G_a$ : the shear modulus of adhesive;

$I(u)$ : the integral of bond slip relationship with respect to slip over  $[0, u]$ ;

$L$ : the bond length of FRP;

$L_{eff}$ : the effective bond length;

$P_{max}$ : the maximum applied force;

$P(u)$ : the applied force versus displacement curve;

$P(u_i)$ : the  $i$ -th force in the applied force versus displacement curve;

$s(x)$ : the slip of FRP at a point  $x$ ;

$s_f$ : the post-peak slip corresponding to null or insignificant bond stress.

$s_i$ : the slip of FRP at the  $i$ -th point along FRP-concrete interface;

$t_a$ : the thickness of adhesive;

$t_f$ : the thickness of FRP;

$u$ : the displacement applied at the loaded end of FRP;

$u_i$ : the  $i$ -th displacement in the applied force versus displacement curve;

$\Delta x_i$ : the interval length of  $[x_{i-1}, x_i]$ ;

$\varepsilon(x)$ : the strain of FRP at a point  $x$ ;

$\varepsilon_i$ : the strain of FRP at the  $i$ -th point along FRP-concrete interface;

$\varepsilon_L$ : the strain of FRP at the loaded end;

$\tau(s)$ : the bond slip relationship that is the relationship between bond stress and slip; and

$\tau_{max}$ : the local bond strength of the bond slip relationship.

## References

- ACI 222R-01. (2001). *Protection of metals in concrete against corrosion. ACI Committee 222.*
- ACI 318-02/318R-02. (2002). *Building code requirements for structural concrete and commentary. ACI Committee 318.*
- ACI 440.2R. (2008). *Guide for the Design and Construction of Externally Bonded FRP Systems. American Concrete Institute ACI Committee 440.*
- ACI 549.4R-13. (2013). *Guide to design and construction of externally bonded fabric-reinforced cementitious matrix (FRCM) systems for repair and strengthening concrete and masonry structures. ACI Committee 549.*
- ACI 562M-13. (2015). *Code Requirements for Evaluation, Repair, and Rehabilitation of Concrete Buildings (ACI 562-13) and Commentary. ACI Committee 562.*
- Ambrisi, A. D., and Focacci, F. (2011). "Flexural Strengthening of RC Beams with Cement-Based Composites." *Journal of composites for construction*, 15(5), 707–720.
- Arboleda, D. (2014). "Fabric Reinforced Cementitious Matrix (FRCM) Composites for Infrastructure Strengthening and Rehabilitation : Characterization Methods." *PhD Thesis.*
- Awani, O., El-Maaddawy, T., and Ismail, N. (2017). "Fabric-reinforced cementitious matrix: A promising strengthening technique for concrete structures." *Construction and Building Materials*, 132, 94–111.
- Badanoiu, A., and Holmgren, J. (2003). "Cementitious composites reinforced with continuous carbon fibres for strengthening of concrete structures." *Cement and Concrete Composites*, 25(3), 387–394.
- Banholzer, B. (2006). "Bond of a strand in a cementitious matrix." *Materials and Structures*, 39(10), 1015–1028.
- Banholzer, B., Brameshuber, W., and Jung, W. (2006). "Analytical evaluation of pull-out tests—The inverse problem." *Cement & Concrete Composites*, 28(6), 564–571.
- Barhum, R., and Mechtcherine, V. (2011). "Mechanical Behaviour under Tensile Loading of Textile Reinforced Concrete with Short Fibres." *6th Colloquium on Textile Reinforced Structures (CTRS6).*
- Bertolini, L., Bolzoni, F., Pastore, T., and Pedefferri, P. (2004). "Effectiveness of a conductive cementitious mortar anode for cathodic protection of steel in concrete." *Cement and Concrete Research*, 34(4), 681–694.
- Bismarck, A., Kumru, M. E., Springer, J., and Simitzis, J. (1999). "Surface properties of PAN-based carbon fibers tuned by anodic oxidation in different alkaline electrolyte systems." *Applied Surface Science*, 143(1), 45–55.
- Boehm, H. P. (2002). "Surface oxides on carbon and their analysis: A critical assessment." *Carbon*, 40(2), 145–149.
- Bubert, H., Ai, X., Haiber, S., Heintze, M., Brüser, V., Pasch, E., Brandl, W., and Marginean, G. (2002). "Basic analytical investigation of plasma-chemically modified carbon fibers." *Spectrochimica Acta - Part B Atomic Spectroscopy*, 57(10), 1601–1610.



- Byrne, A., Norton, B., and Holmes, N. (2016). "State-of-the-art review of cathodic protection for reinforced concrete structures." *Magazine of Concrete Research*, 68(13), 664–677.
- Carol Kozlowski and Peter M.A. Sherwood. (1985). "X-Ray Photoelectron-spectroscopic Studies of Carbon-fibre Surfaces." *Journal of the Chemical Society Faraday Transactions*, 1985, 81(11), 2745-2756.
- Carozzi, F.G., Arboleda, D., Poggi, C., and Nanni, A. (2020). "Direct Shear Bond Tests of Fabric-Reinforced Cementitious Matrix Materials." *Journal of Composites for Construction*, 24(1).
- Carozzi, F.G., Bellini, A., D'Antino, T., de Felice, G., Focacci, F., Hojdys, Ł., Laghi, L., Lanoye, E., Micelli, F., Panizza, M., and Poggi, C. (2017). "Experimental investigation of tensile and bond properties of Carbon-FRCM composites for strengthening masonry elements." *Composites Part B: Engineering*, 128, 100–119.
- Carozzi, F.G., Colombi, P., Fava, G., and Poggi, C. (2016). "A cohesive interface crack model for the matrix – textile debonding in FRCM composites." *Composite Structures*, 143, 230–241.
- Chen, J.F., and Teng, J.G. (2001). "Anchorage strength models for FRP and steel plates bonded to concrete." *Journal of Structural Engineering*, 127(7), 784–791.
- Chini, M., and Antonsen, R. (2008). "Polarization Behavior of Carbon Fiber as an Anodic Material in Cathodic Protection." *11th International Conference on Durability of Building Materials and Components, Istanbul, Turkey, May 11-18*.
- Chung, D.D.L. (2002). "Review graphite." *Journal of material science*, 37(8), 1475-1489.
- Eastwood, B.J., Christensen, P.A., Armstrong, R.D., and Bates, N.R. (1999). "Electrochemical oxidation of a carbon black loaded polymer electrode in aqueous electrolytes." *Journal of Solid State Electrochemistry*, 3(4), 179-186.
- Contamine, R., Larbi, A. S., and Hamelin, P. (2011). "Contribution to direct tensile testing of textile reinforced concrete (TRC) composites." *Materials Science & Engineering A*, 528(29–30), 8589–8598.
- D'Ambrisi, A., Feo, L., and Focacci, F. (2013). "Experimental and analytical investigation on bond between Carbon-FRCM materials and masonry." *Composites Part B: Engineering*, 46, 15–20.
- D'Antino, T., Carozzi, F. G., Colombi, P., and Poggi, C. (2017). *A new pull-out test to study the bond behavior of fiber reinforced cementitious composites. Key Engineering Materials*, 747, 258-265.
- D'Antino, T., Colombi, P., Carloni, C., and Sneed, L. H. (2018). "Estimation of a matrix-fiber interface cohesive material law in FRCM-concrete joints." *Composite Structures*, 193, 103–112.
- D'Antino, T., and Papanicolaou, C. (2017). "Mechanical characterization of textile reinforced inorganic-matrix composites." *Composites Part B: Engineering*, 127, 78–91.

- Dai, J., Ueda, T., and Sato, Y. (2006). “Unified Analytical Approaches for Determining Shear Bond Characteristics of FRP-Concrete Interfaces through Pullout Tests.” *Journal of Advanced Concrete Technology*, 4(1), 133–145.
- Dai, J., Ueda, T., Sato, Y., Bisby, L. a, Green, M. F., and Kodur, V. K. R. (2005). “Development of the nonlinear bond stress-slip model of Fiber Reinforced Plastics Sheet-concrete interfaces with a simple method.” *Journal of Composites for Construction*, 9(1), 52–62.
- Dai, Z., Zhang, B., Shi, F., Li, M., Zhang, Z., and Gu, Y. (2011). “Effect of heat treatment on carbon fiber surface properties and fibers/epoxy interfacial adhesion.” *Applied Surface Science*, 257(20), 8457–8461.
- Dalalbashi, A., Ghiassi, B., Oliveira, D. V., and Freitas, A. (2018a). “Fiber-to-mortar bond behavior in TRM composites: Effect of embedded length and fiber configuration.” *Composites Part B: Engineering*, 152, 43–57.
- Dalalbashi, A., Ghiassi, B., Oliveira, D. V., and Freitas, A. (2018b). “Effect of test setup on the fiber-to-mortar pull-out response in TRM composites: Experimental and analytical modeling.” *Composites Part B: Engineering*, 143, 250–268.
- Donnini, J., and Corinaldesi, V. (2017). “Mechanical characterization of different FRCM systems for structural reinforcement.” *Construction and Building Materials*, 145, 565–575.
- Donnini, J., Corinaldesi, V., and Nanni, A. (2015). “FRCM mechanical properties using carbon fabrics with different coating treatments.” *International Workshop On: “durability & Sustainability of Concrete Structures*, 220–228.
- Escrig, C., Gil, L., and Bernat-Maso, E. (2017). “Experimental comparison of reinforced concrete beams strengthened against bending with different types of cementitious-matrix composite materials.” *Construction and Building Materials*, 137, 317–329.
- Focacci, F., D’Antino, T., Carloni, C., Sneed, L. H., and Pellegrino, C. (2017). “An indirect method to calibrate the interfacial cohesive material law for FRCM-concrete joints.” *Materials and Design*, 128, 206–217.
- Gardner, S. D., Singamsetty, C. S. K., Booth, G. L., He, G. R., and Pittman, C. U. (1995). “Surface characterization of carbon fibers using angle-resolved XPS and ISS.” *Carbon*, 33(5), 587–595.
- GB/T 3362-2005. (2005). *Test methods for tensile properties of carbon fiber multifilament*. China.
- Guo, Z., Cao, S., Sun, W., and Lin, X. (2005). “Experimental study on bond stress-slip behavior between FRP sheets and concrete.” *Proceedings of the International Symposium on Bond Behaviour of FRP in Structures*, (International Institute for FRP in Construction), 77–84.
- Hartig, J. U. (2011). “Numerical investigations on the uniaxial tensile behaviour of Textile Reinforced Concrete.” *Fakultät Bauingenieurwesen*, Ph.D. Thesis.
- Hashemi, S., and Al-Mahaidi, R. (2010). “Investigation of bond strength and flexural behavior of FRP-strengthened reinforced concrete beams using cement-based adhesives.” *Australian Journal of Structural Engineering*, 11(2), 129–139.

- Häußler-Combe, U., and Hartig, J. (2007). “Bond and failure mechanisms of textile reinforced concrete (TRC) under uniaxial tensile loading.” *Cement & Concrete Composites*, 29(4), 279–289.
- Hegger, J., Will, N., Bruckermann, O., and Voss, S. (2006). “Load-bearing behavior and simulation of textile reinforced concrete.” *Materials and Structures*, 39(8), 765–776.
- ISO 679:2009. (2009). *Cement - Test methods - Determination of strength*. International Organization for Standardization, Geneva, Switzerland.
- Jing, X., and Wu, Y. (2011). “Electrochemical studies on the performance of conductive overlay material in cathodic protection of reinforced concrete.” *Construction and Building Materials*, 25(5), 2655–2662.
- Kainourgiou, P., Kartsonakis, I. A., Dragatogiannis, D. A., Koumoulos, E. P., Goulis, P., and Charitidis, C. A. (2017). “Electrochemical surface functionalization of carbon fibers for chemical affinity improvement with epoxy resins.” *Applied Surface Science*, 416, 593–604.
- Koster, T., Peelen, W., Larbi, J., Rooij, M. De, and Polder, R. (2010). “Numerical model of  $\text{Ca}(\text{OH})_2$  transport in concrete due to electrical currents.” *Materials and Corrosion*, 61.
- Koutas, L. N., Tetta, Z., Bournas, D. A., and Triantafillou, T. C. (2019). “Strengthening of Concrete Structures with Textile Reinforced Mortars: State-of-the-Art Review.” *Journal of Composites for Construction*, 23(1), 1–20.
- Lancioni, G., Donnini, J., and Corinaldesi, V. (2017). “A variational model for determining fracture modes in FRCM Systems.” *Procedia Structural Integrity*, 3, 354–361.
- Larrinaga, P., Chastre, C., Biscaia, H. C., and San-José, J. T. (2014). “Experimental and numerical modeling of basalt textile reinforced mortar behavior under uniaxial tensile stress.” *Materials and Design*, 55, 66–74.
- Lee, E. Seok, Lee, C. Hyun, Chun, Y. S., Han, C. Ji, and Lim, D. S. (2017). “Effect of hydrogen plasma-mediated surface modification of carbon fibers on the mechanical properties of carbon-fiber-reinforced polyetherimide composites.” *Composites Part B: Engineering*, 116, 451–458.
- Liu, J., Tian, Y., Chen, Y., and Liang, J. (2010a). “Interfacial and mechanical properties of carbon fibers modified by electrochemical oxidation in  $(\text{NH}_4\text{HCO}_3)/(\text{NH}_4)_2\text{CO}_3 \cdot \text{H}_2\text{O}$  aqueous compound solution.” *Applied Surface Science*, 256(21), 6199–6204.
- Liu, J., Tian, Y., Chen, Y., Liang, J., Zhang, L., and Fong, H. (2010b). “A surface treatment technique of electrochemical oxidation to simultaneously improve the interfacial bonding strength and the tensile strength of PAN-based carbon fibers.” *Materials Chemistry and Physics*, 122(2–3), 548–555.
- Lorenz, E., and Ortlepp, R. (2011). “Bond Behavior of Textile Reinforcements - Development of a Pull-Out Test and Modeling of the Respective Bond versus Slip Relation.” *High Performance Fiber Reinforced Cement Composites*, 479–486.
- Lu, X.Z., Teng, J.G., Ye, L.P., and Jiang, J.J. (2005). “Bond-slip models for FRP sheets/plates bonded to concrete.” *Engineering Structures*, 27(6), 920–937.

- Mork, J.H., S. Mayer, and R. Asheim (2007). “The performance of cathodic protection on harbor and jetty of Honningsvåg Norway”. In: *Proceeding of the 5th International Conference on Concrete Structures Under Extreme Conditions of Environment and Loading*, CONSEC’07, 2007.
- NACE SP0290-2007. (2007). *Impressed current cathodic protection of reinforcing steel in atmospherically exposed concrete structures*.
- Nakaba, K., Kanakubo, T., Furuta, T., and Yoshizawa, H. (2001). “Bond behavior between fiber-reinforced polymer laminates and concrete.” *ACI Structural Journal*, 98(3), 359–367.
- Nguyen, C. Van, Lambert, P., Mangat, P., Flaherty, F. O. ’, Jones, G., Boshkov, N., D’Elia, E., and Valentini, C. (2012). “The Performance of Carbon Fibre Composites as ICCP Anodes for Reinforced Concrete Structures.” *International Scholarly Research Network ISRN Corrosion*, 2012.
- Nguyen, C. Van, Lambert, P., Mangat, P. S., O’Flaherty, F. J., and Jones, G. (2016). “Near-surface mounted carbon fiber rod used for combined strengthening and cathodic protection for reinforced concrete structures.” *Structure and Infrastructure Engineering*, 12(3), 356–365.
- Ombres, L., and Mazzuca, S. (2017). “Confined Concrete Elements with Cement-Based Composites: Confinement Effectiveness and Prediction Models.” *Journal of Composites for Construction*, 21(3), 1–15.
- Park, K.J., Kang, H.J., Choi, I.H., Shin, S., and Kim, S.J. (2016). “Progressive failure analysis of carbon-fiber-reinforced polymer (CFRP) laminates using combined material nonlinear elasticity and continuum damage mechanics based on treatment of coupon test.” *Journal of Composite Materials*, 50(11), 1431–1455.
- Pedferri, P. (1996). “Cathodic protection and cathodic prevention.” *Construction & Building Materials*, 10(5), 391–402.
- Peelen, W.H. A., Polder, R.B., Redaelli, E., and Bertolini, L. (2008). “Qualitative model of concrete acidification due to cathodic protection.” *Materials and Corrosion*, 59(2), 81–90.
- Peled, A., Bentur, A., and Yankelevsky, D. (1998). “Effects of woven fabric geometry on the bonding performance of cementitious composites: mechanical performance.” *Advanced Cement Based Materials*, 7(1), 20–27.
- Peled, A., Sueki, S., and Mobasher, B. (2006). “Bonding in fabric-cement systems: Effects of fabrication methods.” *Cement and Concrete Research*, 36(9), 1661–1671.
- Peled, A., Zaguri, E., and Marom, G. (2008). “Bonding characteristics of multifilament polymer yarns and cement matrices.” *Composites Part A: Applied Science and Manufacturing*, 39(6), 930–939.
- Polder, R., and Peelen, W. (2018). “Cathodic protection of steel in concrete – experience and overview of 30 years application.” *Matec Web of Conferences*, 199.

- Raouf, S.M., Koutas, L.N., and Bournas, D.A. (2016). “Bond between textile-reinforced mortar ( TRM ) and concrete substrates : Experimental investigation.” *Composites Part B*, 98, 350–361.
- Raphael, N., Namratha, K., Chandrashekar, B.N., Sadasivuni, K. K., Ponnamma, D., Smitha, A. S., Krishnaveni, S., Cheng, C., and Byrappa, K. (2018). “Surface modification and grafting of carbon fibers: A route to better interface.” *Progress in Crystal Growth and Characterization of Materials*, 64(3), 75–101.
- De Santis, S., Carozzi, F. G., de Felice, G., and Poggi, C. (2017). “Test methods for Textile Reinforced Mortar systems.” *Composites Part B: Engineering*, 127, 121–132.
- Sato, Y., Asano, Y., and Ueda, T. (2000). “Fundamental study on bond mechanisms of carbon fiber sheet.” 47(648), 71–87.
- Savoia, M., Ferracuti, B., and Mazzotti, C. (2003). “Non-Linear Bond-Slip Law for FRP-Concrete Interface.” *Fibre-reinforced Polymer Reinforcement for Concrete Structures-the Sixth International Symposium on FRP Reinforcement for Concrete Structures*, Singapore, 163–172.
- Sellitti, C., Koenig, J.L., and Ishida, H. (1990). “Surface characterization of graphitized carbon fibers by attenuated total reflection Fourier transform infrared spectroscopy.” *Carbon*, 28(1), 221–228.
- Sneed, L.H., D’Antino, T., Carloni, C., and Pellegrino, C. (2015). “A comparison of the bond behavior of PBO-FRCM composites determined by double-lap and single-lap shear tests.” *Cement and Concrete Composites*, 64, 37–48.
- Subramaniam, K.V., Carloni, C., Nobile, L. (2007). “Width effect in the interface fracture during shear debonding of FRP sheets from concrete.” *Engineering Fracture Mechanics*, 74(4), 578-594.
- Subramaniam, K.V., Carloni, C., Nobile, L. (2011). “An understanding of the width effect in FRP–concrete debonding.” *Strain*, 47(2), 127-137.
- Sueki, S., Soranakom, C., and Mobasher, B. (2007). “Pullout-Slip Response of Fabrics Embedded in a Cement Paste Matrix.” *Journal of Materials in Civil Engineering*, 19(9), 718–727.
- Sueki, S., Soranakom, C., Mobasher, B., and Peled, A. (2005). “Pullout-Slip Response of Fabrics Embedded in a Cement Paste Matrix.” 19(9), 718–727.
- Sun, H., Ali, S., and Yang, M. (2016a). “Degradation of carbon fiber reinforced polymer from cathodic protection process on exposure to NaOH and simulated pore water solutions.” *Materials and Structures*, 49, 5273–5283.
- Sun, H., Wei, L.L., Zhu, M.C., Han, N.X., Zhu, J.H., and Xing, F. (2016b). “Corrosion behavior of carbon fiber reinforced polymer anode in simulated impressed current cathodic protection system with 3 % NaCl solution.” *Construction and Building Materials*, 112, 538–546.
- Sun, Y., Lu, Y., and Yang, C. (2019). “Stripping mechanism of PAN-based carbon fiber during anodic oxidation in NaOH electrolyte.” *Applied Surface Science*, 486, 128–136.

- Tran, C.T.M., Stitmannathum, B., and Ueda, T. (2014). “Investigation of The Bond Behaviour Between PBO-FRCM Strengthening Material and Concrete.” *Journal of Advanced Concrete Technology*, 12(12), 545–557.
- Wang, C., Li, J., Sun, S., Li, X., Zhao, F., Jiang, B., and Huang, Y. (2016). “Electrophoretic deposition of graphene oxide on continuous carbon fibers for reinforcement of both tensile and interfacial strength.” *Composites Science and Technology*, 135, 46–53.
- Wei, L.L., Zhu, J.H., Ueda, T., Su, M.N., Liu, J., Liu, W., Tang, L.P., and Xing, F. (2019). “Tensile behavior of carbon fabric reinforced cementitious matrix composites as both strengthening and anode materials.” *Composite Structures*, 234, 111675.
- Weitzsackert, C.L., and Sherwood, P.M.A. (1995). “X-Ray Photoelectron Spectroscopic Studies of Changes During Electrochemical Oxidation in Base.” *Surface & interface analysis* 23, 551–558.
- Williams Portal, N., Fernandez Perez, I., Nyholm Thrane, L., Lundgren, K., Portal, N.W., Perez, I.F., Thrane, L.N., and Lundgren, K. (2014). “Pull-out of textile reinforcement in concrete.” *Construction & Building Materials*, 71(71), 63–71.
- Xu, S., Krüger, M., Reinhardt, H.-W., and Ožbolt, J. (2004). “Bond Characteristics of Carbon, Alkali Resistant Glass, and Aramid Textiles in Mortar.” *Journal of Materials in Civil Engineering*, 16(4), 356–364.
- Xue, J., Wang, W.X., Zhang, J.Z., and Wu, S.J. (2015). “Progressive failure analysis of the fiber metal laminates based on chopped carbon fiber strands.” *Journal of Reinforced Plastics and Composites*, 34(5), 364–376.
- Yao, J. (2004). “Debonding failures in RC beams and slabs strengthened with FRP plates.” The Hong Kong Polytechnic University, Ph.D. Thesis.
- Yuan, H., Teng, J.G., Seracino, R., Wu, Z.S., and Yao, J. (2004). “Full-range behavior of FRP-to-concrete bonded joints.” *Engineering Structures*, 26(5), 553–565.
- Yue, Z.R., Jiang, W., Wang, L., Gardner, S.D., and Pittman, C. U. (1999). “Surface characterization of electrochemically oxidized carbon fibers.” *Carbon*, 37(11), 1785–1796.
- Yumitori, S., and Nakanishi, Y. (1996). “Effect of anodic oxidation of coal tar pitch-based carbon fiber on adhesion in epoxy matrix: Part 2. Comparative study of three alkaline solutions.” *Composites Part A: Applied Science and Manufacturing*, 27(11), 1059–1066.
- Zhang, E.Q. (2018). “Durability of Reinforced Concrete under Impressed Current Cathodic Protection Failure Mechanism and Service Life Prediction.” Ph.D. Thesis.
- Zhang, E.Q., and Tang, L. (2014). “A Novel Anode Material for Cathodic Prevention of Steel Reinforced Concrete Structures with Hybrid Functions.” 2014.
- Zhang, X.B., Aljewifi, H., and Li, J. (2013). “Failure behavior investigation of continuous yarn reinforced cementitious composites.” *Construction and Building Materials*, 47, 456–464.
- Zhang, X.B., Aljewifi, H., and Li, J. (2014). “Failure Mechanism Investigation of Continuous Fibre Reinforced Cementitious Composites by Pull-out Behaviour Analysis.” *Procedia Materials Science*, 3, 1377–1382.

- Zhu, J.H., Zhu, M.C., Han, N.X., Liu, W., and Xing, F. (2014). “Electrical and Mechanical Performance of Carbon Fiber-Reinforced Polymer Used as the Impressed Current Anode Material.” *Materials*, 7, 5438–5453.
- Zhu, J.H., Wei, L.L., Zhu, M.C., Sun, H.F., Tang, L.P., and Xing, F. (2015). “Polarization Induced Deterioration of Reinforced Concrete with CFRP Anode.” *Materials*, 8(7), 4316–4331.
- Zhu, M.C., Li, W.Q., Zhu, J.H., Ueda, T., Su, M.N., Xing, F., and Li, D.W. (2018). “Bond behavior of a multifilament carbon yarn embedded in cementitious matrix.” *The 8th International Conference of Asian Concrete Federation*, Fuzhou, 283–290.
- Zielke, U., K.J. Hüttinger, and Hoffman, W.P. (1996). “Surface-Oxidized Carbon Fibers : I. Surface Structure and Chemistry.” *Science*, 34(8), 983–998.